AD-A082 534 STATE UNIV OF NEW YORK AT BUFFALO FLUID AND THERMAL S--ETC F/G 20/4
STABILITY AND TRANSITION OF WALL BOUNDARY LAYERS INDUCED BY MOV--ETC(U)
JUL 79 J G HALL, Y M AMR AFOSR-74-2719

UNCLASSIFIED AFOSR-TR-80-0231 NL

1 OF 2
AD
A082534

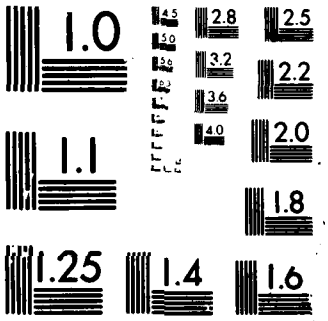

MICROCOPY RESOLUTION TEST CHART
NATIONAL BUREAU OF STANDARDS-1963-A

(9) Final rept.
15 May 74 - 14 May 79

(6)

STABILITY AND TRANSITION OF WALL BOUNDARY LAYERS INDUCED BY MOVING WAVES.

by

(18) (19) AFOSR-TR-80-0231

(10) J. Gordon Hall
and
Yehia Mamoud Amr

State University of New York at Buffalo
Department of Mechanical Engineering
Buffalo, NY, 14260

(16) 2307

(17) A4

Final report on research supported by
the Air Force Office of Scientific Research,
Air Force Systems Command, USAF, under
(15) Grant No. AFOSR 74-2719

(11) 15 Jul[redacted]79

(12) 158

DTIC
ELECTE
S D
A

* Present address: Carrier Corporation, Syracuse, NY, 13221

Approved for public release. Distribution unlimited.

Approved for public release;
distribution unlimited.

Qualified requestors may obtain additional copies from the Defense Documentation Center. All others should apply to the National Technical Information Service.
Conditions of Reproduction: Reproduction, translation, publication, use and disposal in whole or in part by or for the United States Government is Permitted.

AIR FORCE [illegible] OF SCIENTIFIC RESEARCH (AFSC)
NOTICE OF [illegible]
This [illegible] and is
approved [illegible] AFR 190-12 (7b).
Distribution [illegible].
A. D. [illegible]
Technical Information Officer

408 020

UNCLASSIFIED
SECURITY CLASSIFICATION OF THIS PAGE (When Data Entered)

REPORT DOCUMENTATION PAGE

READ INSTRUCTIONS BEFORE COMPLETING FORM

1. REPORT NUMBER: AFOSR-TR- 80-0231
2. GOVT ACCESSION NO.
3. RECIPIENT'S CATALOG NUMBER

4. TITLE (and Subtitle)
STABILITY AND TRANSITION OF WALL BOUNDARY LAYERS INDUCED BY MOVING WAVES

5. TYPE OF REPORT & PERIOD COVERED
FINAL
15 May 1974 - 14 May 1979

6. PERFORMING ORG. REPORT NUMBER

7. AUTHOR(s)
J GORDON HALL
YEHIA MAMOUD AMR

8. CONTRACT OR GRANT NUMBER(s)
AFOSR 74-2719

9. PERFORMING ORGANIZATION NAME AND ADDRESS
UNIVERSITY OF NEW YORK AT BUFFALO
MECHANICAL ENGINEERING DEPARTMENT
BUFFALO, NY 14260

10. PROGRAM ELEMENT, PROJECT, TASK AREA & WORK UNIT NUMBERS
2307A4
61102F

11. CONTROLLING OFFICE NAME AND ADDRESS
AIR FORCR OFFICE OF SCIENTIFIC RESEARCH/NA
BLDG 410
BOLLING AIR FORCE BASE, D C 20332

12. REPORT DATE
July 1979

13. NUMBER OF PAGES
150

14. MONITORING AGENCY NAME & ADDRESS (if different from Controlling Office)

15. SECURITY CLASS. (of this report)
UNCLASSIFIED

15a. DECLASSIFICATION/DOWNGRADING SCHEDULE

16. DISTRIBUTION STATEMENT (of this Report)
Approved for public release; distribution unlimited.

17. DISTRIBUTION STATEMENT (of the abstract entered in Block 20, if different from Report)

18. SUPPLEMENTARY NOTES

19. KEY WORDS (Continue on reverse side if necessary and identify by block number)
FLUID MECHANICS
BOUNDARY LAYER STABILITY
BOUNDARY LAYER TRANSITION

20. ABSTRACT (Continue on reverse side if necessary and identify by block number)

The present study concerns a theoretical investigation of stability and an experimental investigation of transition for wall boundary layers developed within unsteady plane expansion waves and behind shock waves traveling into a gas at rest. The theoretical investigation involved three tasks: the use of approximate methods for the prediction of critical Reynolds numbers, a numerical integration of the Orr-Sommerfeld equation for the incompressible boundary layer flow at the expansion wave head, and the development of a multiple scales technique for nearly quasi-steady, quasi-parallel boundary layer flows. The boundary layer flow at

over

DD FORM 1 JAN 73 1473

UNCLASSIFIED
SECURITY CLASSIFICATION OF THIS PAGE (When Data Entered)

expansion wave head has the same velocity profile as a semi-infinite flat plate given a sudden constant acceleration after being at rest. For this flow a minimum critical Reynolds number $Re_{\delta^*_{cr}}$ =25,488 is calculated. In the experimental study, thin-film surface thermometers, flush hot-film anemometers and hot wire anemometers were used independently and simultaneously to detect boundary layer transition. Expansion wave boundary layer transition times observed after the time of wave head arrival, are five to eight times larger than those previously reported and most of the transition Reynolds numbers observed are above or near the critical Reynolds numbers calculated by the approximate method. Shock wave boundary layer transition times observed are also larger than those previously reported and some of the transition Reynolds numbers observed based on distance to the shock wave front are above the critical values previously calculated. Most of the shock wave boundary layer transition times observed can be correlated with a particle path Reynolds number $Re_{x_p} \approx (4.0 \pm 1) \times 10^6$.

Accession For
NTIS
Unannounced
Availability Codes
Dist. Avail and/or special
A

ABSTRACT

The present study concerns a theoretical investigation of stability and an experimental investigation of transition for wall boundary layers developed within unsteady plane expansion waves and behind shock waves travelling into a gas at rest.

The theoretical investigation involved three tasks: the use of approximate methods for the prediction of critical Reynolds numbers, a numerical integration of the Orr-Sommerfeld equation for the incompressible boundary layer flow at the expansion wave head, and the development of a multiple scales technique for nearly quasi-steady, quasi-parallel boundary layer flows. The boundary layer flow at the expansion wave head has the same velocity profile as a semi-infinite flat plate given a sudden constant acceleration after being at rest. For this flow a minimum critical Reynolds number $Re_{\delta^*_{cr}} = 25{,}488$ is calculated.

In the experimental study, thin-film surface thermometers, flush hot-film anemometers and hot wire anemometers were used independently and simultaneously to detect boundary layer transition. Expansion wave boundary layer transition times observed after the time of wave head arrival, are five to eight times larger than those previously reported and most of the transition Reynolds numbers observed are above or near the critical Reynolds numbers calculated by the approximate method. Shock wave boundary layer transition times observed are also larger than those previously reported and some of the transition Reynolds numbers observed based on distance to the shock wave front are above the critical values previously calculated. Most of the shock wave boundary layer transition times observed can be correlated with a particle path Reynolds number $Re_{x_p} \approx (4.0 \pm 1) \times 10^6$.

NOMENCLATURE

A	defined by Eq. 3.29
A_o	defined by Eq. 3.33
a	overheat ratio, $a = (\frac{R_f}{R_o} - 1)$
a_e	speed of sound at inviscid flow temperature
a_o	speed of sound at $T = T_o$
$B_1, B_2, \ldots, B_8$	defined by Eq. 3.31
$c = c'/u_e$	dimensionless complex disturbance speed of propagation
$c' = \omega/k$	complex disturbance phase velocity
C_p, C_v	gas specific heats, assumed constant
e	defined by Eq. 2.4
E_f	film voltage
F	function defined by Eq. 2.14
f_1, f_2	functions defined by Eq. 3.33
FHFA	Flush Hot-Film Anemometer
G	function defined by Eq. 2.15
g_1, g_2	functions defined by Eq. 3.33
H	shape factor $= \delta^*/\theta$
h_1, h_2, h_3, h_4	functions defined by Eq. 3.39
HWA	Hot-Wire Anemometer
I_1, I_2, I_3, I_4	integrals defined by Eq. 3.41
$k = k'\,\delta_R$	dimensionless complex disturbance wave number, $k = k_r + ik_i$; or coefficient of thermal conductivity.
k'	complex disturbance wave number, $k' = k_r' + ik_i'$
L	effective hot-film length

L^*	actual hot-film length
M_s	shock wave Mach number $= \frac{u_s}{a_o}$
p	gas pressure
q	local surface heat transfer rate
R_f	electrical resistance of film
R_w	electrical resistance of hot-wire
R_o	electrical resistance of wires or films at room temperature ($\approx 70°F$)
Re	Reynolds number $u_R \delta_R / \nu_R$
Re_ℓ	Reynolds number based on length ℓ
s	dimensionless similarity variable, defined by Eq. 2.6
s_d	dimensionless similarity variable, defined by Table IV
s_o	dimensionless similarity variable, defined by Eq. 2.1
T	gas temperature
t	time, measured from expansion wave origin; dimensionless in Sec. 3
t_1	dimensionless slow time variable for multiple scales analysis, $= \varepsilon t$
u	mean value of velocity along x, parallel to wall
$U = \frac{u}{u_R}$	dimensionless component of mean velocity along x, parallel to wall
u_2	inviscid gas velocity along x behind shock wave (tube fixed coordinates)
u_R	representative reference value of u, usually $u_R = u_e$
u_s	velocity of shock wave
u'	disturbance velocity along x, parallel to wall
v'	disturbance velocity along y, perpendicular to wall

v	mean component of velocity along y, perpendicular to wall
v_g	dimensionless group velocity defined by Eq. 3.26
$V = \frac{v}{u_R}$	dimensionless component of mean velocity along y, perpendicular to wall
X	distance coordinate parallel to wall, measured from the expansion wave origin; dimensionless in Sec. 3 with arbitrary origin.
X_{sw}	distance from shock wave front
X_p	particle path length
X_s	distance from diaphragm location
X_1	dimensionless slow distance scale used in multiple scales analysis, $= \varepsilon x$
y	normal distance from the wall; dimensionless in Sec. 3

Greek Symbols

α_t	coefficient of thermal resistivity
β	$(\frac{2}{\gamma+1})$
$\gamma = C_p/C_v$	constant
δ	boundary layer thickness, defined by $u/u_e = .99$
δ_R	representative reference value of length for y direction
δ^*	local boundary layer displacement thickness $= \int_0^\infty (1-\frac{\rho u}{\rho_e u_e})dy$
$\bar{\varepsilon}$	$(\gamma-1)/(\gamma+1)$
ε	$1/Re = \nu_R/u_R\delta_R$
η	similarity variable, Eq. 2.14
μ	viscosity coefficient of the gas

λ	wave length of disturbance
ν	kinematic viscosity = μ/ρ
ρ	gas density
σ	gas Prandtl number $\mu C_p/k$
ζ	defined by Eq. 3.29
ζ^*	solution to Eq. 3.30
τ	time since wavehead arrival at observation station
τ_w	local shear stress at the wall
$\bar{\tau}_w$	non-dimensional skin friction, Eq. B-13
ϕ	amplitude of disturbance stream function of Eq. 3.3
$\bar{\phi}_1, \bar{\phi}_2$	solution vectors: $\bar{\phi}_1 = (\phi_1, \phi_1', \phi_1'', \phi_1''')$, $\bar{\phi}_2 = (\phi_2, \phi_2', \phi_2'', \phi_2''')$
ϕ_1, ϕ_2	solutions satisfying Eq. 3.4
θ	local boundary layer momentum thickness = $\int_0^\infty (1 - \frac{U}{U_e})\frac{U}{U_e}\frac{\rho}{\rho_e}\,dy$; or as defined in Sec. 3.3
θ_o	defined by Eq. 3.21
θ_1	defined by Eq. 3.34
ψ	disturbance stream function
$\omega = \frac{\omega'\delta_R}{u_R}$	dimensionless complex disturbance frequency, $\omega = \omega_r + i\omega_i$
ω'	complex disturbance frequency, $\omega' = \omega_r' + i\omega_i'$

<u>Subscripts</u>

cr	denotes critical value
e	denotes inviscid flow property
f	denotes film property
H	denotes wave head
i	denotes imaginary part of a complex quantity

0	denotes initial conditions, ahead of wave
p	denotes particle path
r	denotes real part of a complex quantity
R	denotes reference quantity
TR	denotes transition
w	denotes wall condition

CONTENTS

Acknowledgements	i
Abstract	ii
Nomenclature	iii
1.0 INTRODUCTION	1
2.0 THE MEAN FLOW PROPERTIES OF THE EXPANSION WAVE LAMINAR BOUNDARY LAYER	10
2.1 Definition of Inviscid Expansion Wave Flow and Coordinate System	10
2.2 Solution to the Laminar Boundary Layer Equations for the Expansion Wave Flow	13
3.0 STABILITY ANALYSES	19
3.1 Approximate Stability Analyses and Application to the Quasi-Steady Expansion Wave Boundary Layer	21
3.2 Numerical Solution of the Orr-Sommerfeld Equation for the Expansion Wave Boundary Layer	27
3.3 The Method of Multiple Scales for the Stability of Unsteady Boundary Layers	32
4.0 EXPERIMENTAL PROGRAM ON TRANSITION TIMES	46
4.1 Scope of Experimental Study	46
4.2 The Expansion Wave Tube	47
4.3 Static Pressure Measurements	51
4.4 Instrumentation for Detection of Boundary Layer Transition	51
Flush Hot-Film Anemometer	51
Hot-Wire Anemometer	52
Thin Film Resistance Thermometer	54
5.0 EXPERIMENTAL RESULTS FOR TRANSITION	56
5.1 Static Pressure	56
5.2 Flush Hot-Film Anemometer Results	59

5.3 Hot Wire Results 62

5.4 Thin Film Thermometer Results 63

5.5 Transition Times for the Shock-Wave Boundary Layer 65

5.6 Transition Times for the Expansion-Wave Boundary Layer 66

6.0 SUMMARY AND CONCLUSIONS 69

References 73

Tables

Figures

APPENDIX A: The Computer Program for Solution of the Orr-Sommerfeld Equation A-1

A.1 Program Description A-1

A.2 Operation of Integration Function Subroutine (F(X)) A-4

A.3 Program Listing

APPENDIX B: Interpretation of the Flush Hot-Film Anemometer Output for the Expansion Wave Boundary Layer B-1

1.0 INTRODUCTION

In the last few decades, there have been many investigations concerning laminar to turbulent transition of boundary layer flows. Most of these investigations have concerned steady flows, wherein the mean or base flow field is independent of time. The problems of laminar boundary layer stability and transition in unsteady flows, where the mean flow does vary with time, have by comparison received much less attention. The present study concerns both the stability and the transition characteristics of such time varying laminar boundary layers, with emphasis on a time variation of the mean flow which is non-periodic. In this study, a linear stability analysis is formulated, and particular application is made to the experimental situation of the unsteady, two-dimensional wall boundary layer formed by a plane unsteady expansion wave travelling into a gas at rest. As part of the study, experiments with such expansion waves were conducted to determine the time or position of transition of the initially laminar boundary layer over a range of pertinent conditions. The same experimental apparatus was also used to obtain transition time data behind plane shock waves for comparison with results of earlier investigators.

Regarding the motivation for the present study, the phenomena of stability and transition of unsteady boundary layers are of interest in the context of basic fluid dynamics research and also as regards various engineering applications. Applications of interest include the wall boundary layer behavior in various gas-dynamic devices such as shock tubes, expansion tubes, and combustion tubes, all of which utilize transient wave-induced flows, as well as unsteady boundary layer behavior in external flows over bodies. External flow applications include that of a body in

flight moving with a time dependent velocity. In this connection it may be noted that the expansion-wave wall boundary layer of interest in the present study is initially identical (close to the wavehead) to the unsteady laminar boundary layer formed on a semi-infinite flat plate undergoing a constant acceleration from rest.

The expansion wave flow was generated experimentally by the rapid rupture of a mylar diaphragm which sealed a pressurized tube of rectangular cross-section. An expansion wave (Fig.1a) travels into the tube accelerating the gas from rest (before the wavehead) in a direction opposite to the wave travel. A final constant state is reached following the wave tail. The expansion wavehead travels at the local speed of sound of the rest gas and the wave widens with distance or time from the origin. The wall boundary layer thus develops under the influence of a strong accelerating pressure gradient which is time dependent, the gradients decreasing with time. As the inviscid gas accelerates, it expands isentropically so that pressure, density, and temperature decrease monotonically with time. The inviscid gas is cooled below the wall temperature (which decreases only slightly with time) so that there is some heat transfer from the wall to the boundary layer gas.

The boundary layer induced on a plane wall behind a plane shock wave travelling at constant speed into a gas at rest is a steady flow phenomenon in a reference frame attached to the wave. Transition time data for the shock wave boundary layer in air have been obtained by a number of investigators [eg, 1,3,4,6]. Usually the time of transition at a fixed location was detected using thin-film resistance thermometers mounted flush on the surface and operated "cold" at minimal current levels to measure local surface temperature change with time. The time of transition after the arrival of the wave at a given station is typically indicated by a

pronounced increase in the slope of the surface temperature-time record. The data of most experiments except Thompson's [4] agree quite well when correlated in terms of a transition Reynolds number based on the distance of transition from the wave front. Thompson observed transition times on glass inserts which were two to five times larger than times observed by most other investigators, and his experiments were limited by the arrival of disturbances from the junction of the glass insert and metal wall. An important feature to be noted is that the transition Reynolds numbers deduced from most of the shock wave boundary layer experiments fall far below the critical stability Reynolds numbers predicted by a linear stability analysis done by Ostrach and Thornton [7]. The linear stability theory of Ref. 7 is based on the model of two-dimensional Tollmien-Schlichting disturbances arising in the compressible (steady) laminar boundary layer developed behind a plane shock, the boundary layer flow itself being assumed quasi-parallel for stability considerations. The shock wave experimental data therefore suggest that other factors or mechanisms were present in the experiments which dominated the occurrence of transition.

In contrast to the shock wave flow, the inviscid flow within an expansion wave is inherently unsteady in any frame of reference. The wall boundary layer transition within the expansion wave has apparently not received any previous attention except by Chabai [1] and Mack [40]. Using thin-film surface thermometers, Chabai [1] conducted careful transition time experiments for both shock-wave and expansion-wave boundary layers in nitrogen. The experiments used glass plate inserts in the wall of a duralumin tube of 3/8-inch by 4-inch rectangular internal cross-section. For the expansion wave flows, the initial tube pressure of nitrogen was

varied from .7 to 12 atmospheres and data was obtained at distances from 3 to 16 feet from the diaphragm station. Chabai found that transition times increased as the initial pressure level decreased and as the distance from the diaphragm location increased. However, he was not able to correlate the data with any form of Reynolds number, unlike the transition time data for the shock-wave boundary layer. Chabai also concluded that transition of the expansion-wave boundary layer was not significantly affected by glass-metal junctions or other small surface irregularities or steps, unlike the shock-wave boundary layer which was demonstrated to be very sensitive in that respect. Chabai's conclusion is at variance with the results of the present experiments which indicate transition of the expansion-wave boundary layer to be very sensitive to small roughness elements or joints in the tube walls. Generally, the transition times measured in the present study are very much greater than those reported by Chabai. The transition data obtained by Mack [40] using optical methods for the expansion wave at an initial pressure level of 1000 mm Hg correlate well in terms of a particle path-length Reynolds number of 2.5×10^6 at transition. However, data for other pressures could not be correlated by this particular Reynolds number.

There are various flow parameters other than Reynolds number which affect boundary layer transition; for example, both heat transfer and pressure gradients influence transition. Various other factors may also have significant effect on transition but cannot always be detected or completely eliminated, such as wall vibration, free stream disturbances, and wall roughness. For new flow situations particularly, experiments are usually necessary if the occurrence of transition is to be established with any certainty. Several comprehensive reviews of transition research

bring out the great complexities of transition phenomena and emphasize the lack of fundamental understanding and the difficulty of conducting truly meaningful experiments [33,34,48].

Dryden [20] utilized the transition data of several investigators and showed that a free stream turbulence level greater than .1% had a significant effect on transition of a flat-plate boundary layer. For disturbances which are sufficiently large ($\frac{u'}{u_e} > .2$), Elder [45] observed breakdown to turbulence to begin for Reynolds numbers below critical values predicted from linear stability analysis of self-excited disturbances.

The influence of wall roughness or protrusions on transition is dependent of h/δ and the Reynolds number $Re_h = \frac{u_h h}{\nu}$, where h is the height of the protrusion and u_h is the velocity at that distance from the wall. Squire [58] utilized linear stability theory for incompressible flow to demonstrate that two-dimensional disturbances such as might be produced by a wire placed at the wall and normal to the direction of the flow, are more effective in bringing about boundary layer instability than three-dimensional disturbances such as those produced by distributed roughness elements. For the two-dimensional roughness element consisting of a wire placed on the surface and perpendicular to the flow, Swigart [46] observed that transition was influenced when Re_h exceeded 50 to 150, whereas for distributed three-dimensional elements, the corresponding Re_h value exceeded 250 to 300. The ratio of the wire height to the boundary layer thickness δ is also important. Dryden [47] has shown that for $h/\delta > .15$, the effect on transition is significant. For the expansion wave flow the initial boundary layer thickness is zero at the time of wave head arrival. Protrusions can trip the boundary layer for some initial period even though

the Reynolds number is substantially below the critical Reynolds number determined from linear stability theory. If the Reynolds number remains below the critical Reynolds number and the boundary layer becomes sufficiently thick compared to the protrusion height then the tripped boundary layer could re-laminarize. The region of flow temporarily made turbulent in this manner is referred to herein as a "turbulent slug". This effect was observed in initial experiments of the present study but was not observed after small steps or protrusions were eliminated.

The effect of pressure gradient on stability and transition can be quite substantial. The critical stability Reynolds numbers for Falkner-Skan velocity profiles have been derived by Tetervin and Levine [44] from an approximate prediction method of Lin [12]. The results agree well with actual solutions to the Orr-Sommerfeld stability equation obtained by others [27,13,14,16]. In the presence of a favorable pressure gradient, the flow is accelerated and the critical Reynolds number thereby increases and instability is delayed. For an unfavorable pressure gradient, the velocity profile has a point of inflection and the opposite is true. For a sufficiently large favorable pressure gradient, a turbulent boundary layer or a boundary layer that has been tripped may become laminar again [17,18]. Lin's approximate method has been extended by Lees [36] to predict the stability of compressible boundary-layer flows and has been used by Tetervin [37] to predict the point of instability for Falkner-Skan profiles with heating at the walls. Lees' method was also used by Ostrach and Thornton [7] for the stability of the shock-wave wall boundary-layer, and the results agree well with the exact solution to the Orr-Sommerfeld stability equation for the flow induced by a very weak shock wave.

In the present study, the stability of the expansion-wave boundary layer, which has not hitherto been investigated, has been examined from

several points of view. The traditional approach in treating the stability of unsteady boundary layers has been to assume both a quasi-parallel and a quasi-steady model. That is, the base flow to be perturbed is assumed spatially parallel, thereby neglecting the influence of the change of boundary-layer thickness with streamwise distance, and steady-flow stability theory is then assumed to apply at any instant in time in terms of the actual instantaneous velocity profiles of boundary layer. Intuitively, the quasi-steady assumption might be expected to be more or less valid if the time characterizing change of the mean flow is sufficiently large compared to the time characterizing the disturbance field. In an early paper Shen [22] obtained a somewhat more quantitative criterion for a quasi-steady model to be reasonably valid. This criterion is that the characteristic time of the base flow be much larger than $Re_\delta^{1/3}$ times the characteristic time of the disturbance. Here Re_δ is the Reynolds number based on the inviscid free-stream velocity relative to the wall and the local boundary-layer thickness δ. Shen also pointed out that quasi-steady solutions could only indicate whether the boundary-layer flow in question was <u>momentarily</u> stable or not. The present study is mainly concerned with non-periodic unsteadiness of the mean flow. The analysis of the stability of unsteady <u>periodic</u> flows has received considerable attention in recent years, particularly by Davis [38] and his colleagues.

Over a fairly wide range of conditions, the expansion-wave boundary layer is found to satisfy reasonably well Shen's criterion for near quasi-steady stability. A quasi-steady, quasi-parallel model was therefore investigated first in the present stability study, with two approaches being followed in this respect. The first approach uses the approximate

method of Lees [36] to obtain the critical stability Reynolds numbers for the fully compressible expansion-wave boundary layer with heat-transfer effects included. The second approach has been to solve numerically the quasi-steady Orr-Sommerfeld equation and obtain the quasi-steady neutral stability curve for the near incompressible flow region close to the expansion wavehead.

Beyond the limiting results for a quasi-steady model, a logical next step or improvement for near quasi-steady boundary layers may be undertaken by a singular perturbation analysis using the method of multiple scales. In this approach, a slow time variable is introduced to characterize the mean flow time dependence. This is similar in spirit to Saric and Nayfeh's multiple scales analysis of spatial non-parallel effects in steady boundary layer flows [28]. Such an analysis is developed in Sec. 3 considering spatial non-parallel effects as well as a mean flow time dependence. The analysis is developed in a general form and is applicable to any unsteady boundary layer which is near quasi-steady.

In the present experimental study, a hot-wire anemometer in the boundary layer, a hot-film surface anemometer, and a "cold" thin-film surface resistance thermometer were all utilized to detect the occurrence of transition on the sidewalls of a specially constructed 4-foot long test section. The transition times observed for the expansion-wave boundary layer were some five to eight times larger than the times reported by Chabai [1] for corresponding conditions of initial pressure level, tube station, etc. The corresponding transition Reynolds numbers lie close to the calculated critical stability Reynolds numbers, and exceed the later values for some conditions.

The differences between the present data and those of Chabai for

the expansion wave boundary layer are at least partly attributed to the significant effects found on transition of very small wall roughness elements or surface junction steps, which were eventually eliminated in the final test section used. The presence of such effects was first revealed in the present studies by surface hot-film anemometer records. Analysis of the surface hot-film indicated it responded essentially to the local quasi-steady skin friction which, at the high Reynolds numbers concerned, undergoes an extremely rapid and large step-like increase on transition. In contrast, the surface temperature recorded by the cold thin-film resistance thermometer shows only a moderate change of slope on transition, and roughness effects can thereby be effectively masked.

In the present shock-wave boundary layer studies, transition Reynolds numbers based on distance behind the shock were observed to be several orders of magnitude higher than those reported by most previous investigators [1,3] but agree fairly well with or exceed the data of Thompson [4]. For some conditions, the present experimental Reynolds numbers at transition do in fact exceed the critical stability Reynolds numbers calculated by Ostrach and Thornton [7].

In the following sections, the mean flow properties of the expansion-wave boundary layer are first discussed in Sec. 2. The stability analyses are taken up in Sec. 3. The experimental program and apparatus for the transition studies are described in Sec. 4, and the experimental transition results are discussed in Sec. 5.

2.0 THE MEAN FLOW PROPERTIES OF THE EXPANSION WAVE LAMINAR BOUNDARY LAYER

2.1 Definition of Inviscid Expansion-wave Flow and Coordinate System

The inviscid flow outside of the boundary layer is assumed to be that generated by a plane isentropic expansion or compression wave. The Reynolds number is very large so that the boundary layer is extremely thin compared to the expansion or shock tube width. Boundary layer displacement thickness effects can thus be neglected. For the coordinate system of Fig. 1b, the basic equations governing mass and momentum balance for unsteady, inviscid, one-dimensional and compressible flow can be written as follows:

$$\frac{\partial \rho}{\partial t} + \rho \frac{\partial u}{\partial x} + u \frac{\partial \rho}{\partial x} = 0$$

$$\frac{\partial u}{\partial t} + u \frac{\partial u}{\partial x} = - \frac{1}{\rho} \frac{\partial p}{\partial x}$$

The gas is assumed to be thermally perfect with constant specific heats C_p and C_v, so that the specific heat ratio γ is constant. For centered expansion waves, the family of characteristics II as defined below have a unique origin in the x-t plane, Fig. 1a. The expansion wave under study is actually non-centered as shown in Fig. 1b especially at stations close to the diaphragm. The non-centered wave effects on the wall boundary-layer have been investigated by Hall et al [8] and Srinivasan [5]. The two families of mathematical characteristics governing the flow are as follows [9]:

Along I: $\frac{dx}{dt} = u_e + a_e$ and $\frac{\gamma-1}{2} u_e + a_e = P = \text{constant}$

Along II: $\frac{dx}{dt} = u_e - a_e$ and $\frac{\gamma-1}{2} u_e - a_e = Q = \text{constant}$

The gas is initially at rest and at a uniform state so that the relation

$$\frac{\gamma-1}{2} u_e + a_e = a_o = \text{constant}$$

applies locally throughout the flow, and the family of characteristics II are straight lines of slope

$$\frac{dx}{dt} = u_e - a_e = \frac{u_e}{\beta} - a_o$$

along which the flow properties are constant.

Because of the simple wave nature of the flow, any inviscid flow property Q satisfies the equation:

$$\frac{\partial Q}{\partial t} = -(\frac{u_e}{\beta} - a_o)\frac{\partial Q}{\partial x}$$

For the velocity u_e this gives

$$t' \frac{\partial u_e}{\partial t'} = [s_o - \frac{u_e}{(\beta\ a_o)}]\frac{\partial u_e}{\partial s_o} \qquad (2.1)$$

when transformed in terms of the similarity variable $s_o = (x + a_o t)/a_o t$ and $t' = t$. The magnitude of the similarity variable s_o, for a centered wave, is the ratio of the distance along x of any point x,t from the wavehead to the corresponding distance of the wavehead from the wave origin (Fig. 1a). s_o is positive for expansion waves, negative for compression waves, and becomes zero at the wavehead.

For a centered wave u_e depends only on s_o, and from Eq. (2.1) the centered wave solution is thus $u_e = \beta a_o s_o$, which makes $\partial u_e/\partial t'$ vanish identically throughout the flow field. For a non-centered wave u_e depends on t' as well as on s_o and $\partial u_e/\partial t'$ is generally not zero. At the wavehead, however, Eq. (2.1) indicates that $\partial u_e/\partial t'$ must still vanish for a non-centered wave because both s_o and u_e become zero at that point. This

implies that to first order derivatives any non-centered simple wave of the type considered here (i.e., non-vanishing first derivative at the wavehead) behaves at the wavehead as a centered wave. More formally, this may be shown by representing u_e as a power series expansion in s_o with coefficients dependent on t' determined via Eq. (2.1), which gives for the class of waves considered

$$u_e = \beta a_o s_o + b_2 s_o^2/t' + [\frac{b_3}{t'} + 2b_2^2/\beta a_o t'^2] s_o^3 + \ldots \qquad (2.2)$$

where the b's are arbitrary constants. Eqs. (2.1) and (2.2) also indicate that the non-centered wave tends asymptotically to have centered wave behavior as time t' increases, which is also evident on physical grounds that e becomes small compared to x. The first derivatives with respect to x and t of the inviscid flow properties at the wavehead are then found to be given by centered wave relations, in particular

$$(\frac{\partial u_e}{\partial t})_H = a_o(\frac{\partial u_e}{\partial x})_H = \beta a_o/t_H = -\beta a_o^2/x_H \qquad (2.3a)$$

or in terms of pressure p_e,

$$(\frac{\partial p_e}{\partial t})_H = a_o(\frac{\partial p_e}{\partial x})_H = -\gamma\beta p_o/t_H = \gamma\beta p_o a_o/x_H \qquad (2.3b)$$

The slope of the pressure-time record measured at the instant of wavehead arrival can thus be used to determine the origin of the x-t coordinate system of Fig. 1b.

In Fig. 1b, the distance e is the particular value of x at which the family II characteristic through any point x,t intersects the x-axis. e may also be regarded as the x displacement of the fluid particle at (x,t) from its position in the corresponding centered wave flow. It follows that for any such point (x,t) the relation

$$\frac{x - e}{t} = (\frac{dx}{dt})_{II} = \frac{u_e}{\beta} - a_o \qquad (2.4)$$

applies, from which u_e can be expressed in the form

$$u_e = \beta a_o s \tag{2.5}$$

where

$$s = (x + a_o t - e)/a_o t = s_o - \frac{e}{a_o t} \tag{2.6}$$

Here s is to be considered a new independent variable with e depending on x and t, which gives a local inviscid flow similarity for the non-centered waves analogous to s_o for centered waves. At the wavehead s = 0 as $x = -a_o t$ and e = 0 at that point. In terms of s, the relations for the other dependent variables of the inviscid (isentropic) flow may be summarized as follows:

$$\left(\frac{p_e}{p_o}\right)^{\bar{\varepsilon}/\gamma\beta} = \left(\frac{\rho_e}{\rho_o}\right)^{\bar{\varepsilon}/\beta} = \left(\frac{T_e}{T_o}\right)^{1/2} = \frac{a_e}{a_o} = (1 - \bar{\varepsilon}s) \tag{2.7}$$

For a non-centered expansion wave e can be determined from the time-pressure record by comparison of the value of s derived from Eq. (2.7) and s_o derived for a centered expansion wave. The difference is significant for locations close to the wavehead origin where e may be within an order of magnitude of x.

2.2 Solution to the Boundary Layer Equations for Expansion Wave Flow

The expansion-wave boundary layer velocity and temperature profiles obtained from previous studies are used in the stability analyses of Sec. 3. The following is a discussion of how those solutions are obtained.

The expansion wave boundary layer first received attention by Mirels [2] who considered the laminar and turbulent boundary layer behind a concentrated expansion wave of zero thickness. The laminar boundary layer formed within unsteady centered expansion waves was first studied by

Cohen [10] and Trimpi and Cohen [11]. Hall [57] extended the analysis of Cohen [10] to include the compression wave case, the effect of the wall temperature change due to the finite wall thermal conductivity and the displacement effect of the boundary layer on the inviscid flow. Hall et al. [8] also investigated the boundary layer developed within a non-centered wave.

For the purpose of stability analysis in the present study, the expansion wave is assumed to be a centered wave. The inviscid flow quantities u_e, p_e, T_e, ρ_e are then given by Eq. (2.7). The laminar boundary layer displacement thickness is typically less than one percent of the expansion tube width so that it does not affect the inviscid flow quantities.

The unsteady laminar boundary layer is governed by the usual two-dimensional boundary layer approximations. The equations for conservation of mass, momentum and energy in an unsteady compressible boundary layer are then respectively as follows:

$$\frac{\partial \rho}{\partial t} + \frac{\partial(\rho u)}{\partial x} + \frac{\partial(\rho v)}{\partial y} = 0 \tag{2.8}$$

$$\rho\left[\frac{\partial u}{\partial t} + u\frac{\partial u}{\partial x} + v\frac{\partial u}{\partial y}\right] = -\frac{\partial p}{\partial x} + \frac{\partial}{\partial y}\left(\mu\frac{\partial u}{\partial y}\right) \tag{2.9}$$

$$\rho C_p\left[\frac{\partial T}{\partial t} + u\frac{\partial T}{\partial x} + v\frac{\partial T}{\partial y}\right] = \frac{\partial p}{\partial t} + u\frac{\partial p}{\partial x} + \frac{\partial}{\partial y}\left(\frac{\rho C_p}{\sigma}\frac{\partial T}{\partial y}\right) + \mu\left(\frac{\partial u}{\partial y}\right)^2 \tag{2.10}$$

In addition, $\frac{\partial p}{\partial y} = 0$ so that $p = p_e(x,t)$ throughout the flow. The assumed perfect gas has the equation $p = \rho RT$. Eqs. (2.8)-(2.10) are governed by the following boundary conditions:

at $y = 0$: $u = 0$, $v = 0$, $T = T_w(x,t)$, $\rho = \rho_w(x,t)$

at $y = \infty$: $u = u_e(x,t)$, $T = T_e(x,t)$, $\rho = \rho_e(x,t)$, $p = p_e(x,t)$

At the wavehead ($x = x_H = a_o t_H$):

$$u = 0,\ T = T_o,\ \rho = \rho_o,\ p = p_e = p_o$$

Subscript o denotes conditions prior to the expansion wavehead arrival.

Typically the wall temperature $T_w(x,t)$ decreases only slightly from T_o due to the high heat capacity of the wall compared to air particularly for the steel wall used in the present study. The actual wall temperature, $T_w(x,t)$ may be determined from the simultaneous solution of the heat conduction equation governing heat flow in the walls and the gas boundary layer equations, as first done by Hall [57]. For the purpose of this study, it is reasonable to neglect the change in T_w and to assume $T_w = T_o$ = constant.

The boundary layer equations were solved by Cohen [10] assuming an isothermal wall and a centered expansion wave in terms of similarity variables η and s_o. The governing boundary layer eqs. (2.8)-(2.10) can be transformed in terms of new independent variables s_o, η, defined by

$$s_o = (x + a_o t)/a_o t$$
$$\eta = \frac{1}{(\nu_o s_o t)^{1/2}} \int_o (\rho/\rho_o)dy \qquad (2.11)$$

The differential equations can thus be written in terms of variables η and s_o instead of the three variables x, y and t. The magnitude of the similarity variable s_o is the ratio of the distance along x of any point (x,t) from the wavehead to the corresponding distance of the wavehead from the wave origin. It is convenient at this point to introduce new dependent variables $F(s_o,\eta)$ and $G(s_o,\eta)$ defined by:

$$u = u_e \frac{\partial F}{\partial \eta} = \beta a_o s_o \frac{\partial F}{\partial \eta} \tag{2.12}$$

$$T = T_w + (T_e - T_w)G = T_w + \Delta T\ G \tag{2.13}$$

where $\Delta T = Te - T_o$

as $\eta \to \infty$; $\frac{\partial F}{\partial \eta} = G = 1$

at the wall $\eta = 0$; $\frac{\partial F}{\partial \eta} = G = 0$

The local coefficient of viscosity μ is taken to be proportional to T so that the product $\rho\mu$ is constant across the boundary layer and is given in terms of the pressure by:

$$\rho\mu = \rho_o\mu_o = \rho_o\mu_o \frac{p_e}{p_o} \tag{2.14}$$

The terms in Eqs. (2.8)-(2.10) involving the normal velocity component v are eliminated by use of the continuity relation, Eq. (2.8). The final transformed equations governing F and G, which give the velocity and temperature distributions in the gas boundary layer, can be written as follows:

$$\frac{p_e}{p_o} F_{\eta\eta\eta} + (\frac{\eta}{2} + \frac{3}{2}\beta s_o F + \beta s_o^2 F_{s_o})F_{\eta\eta} - (s_o F_{s_o\eta} + F_\eta) \times$$

$$(1 - s_o + \beta s_o F_\eta) - \frac{p_e'}{\gamma\beta\ T_o p_e}(T_w + \Delta T\ G) = 0 \tag{2.15}$$

$$\frac{p_e}{\sigma p_o} G_{\eta\eta} + (\frac{\eta}{2} + \frac{3}{2}\beta s_o F + \beta s_o^2 F_{s_o})G_\eta - s_o(\frac{1 - s_o + \beta s_o F_\eta}{\Delta T}) \times$$

$$[(T_w + \Delta T\ G)_{s_o} - \frac{2\bar{\varepsilon}\ p_e'}{\beta\gamma\ p_e}(T_w + \Delta T\ G)]$$

$$+ \frac{2\varepsilon\ \beta\ T_o\ p_e}{p_o\ \Delta T} s_o^2 F_{\eta\eta}^{\ 2} = 0 \tag{2.16}$$

In Eqs. (2.15) and (2.16), p_e' denotes dp_e/ds_o, and the subscripts s_o, η, t denote partial derivatives.

Equations (2.15) and (2.16) are coupled nonlinear partial differential equations which can only be solved numerically. The main flow region of interest in the present study is that close to the wavehead where values of s_o tend to be small compared to unity. For small values of s_o we can assume a coordinate expansion in s_o of the form

$$F = F_o + F_1 s_o + F_2 S_o^2 + \ldots$$
$$G = G_o + G_1 s_o + G_2 s_o^2 + \ldots \tag{2.17}$$

where the coefficients F_i and G_i depend on η only. This procedure was used by Cohen [10]. Substitution of Eq. (2.17) into Eqs. (2.15) and (2.16) yields the sequence of linear equations:

$$F_i''' + \frac{\eta}{2} F_i'' - (i+1)F_i' = \overline{F_i}(F_{i-1}, G_{i-1})$$
$$\frac{1}{\sigma} G_i'' + \frac{\eta}{2} G_i' - (i+1)G_i = \overline{G_i}(F_{i-1}, G_{i-1}) \tag{2.18}$$

$i = 0, 1, 2, \ldots.$

at $\eta = 0$: $F_o' = G = 0$, $F_1' = F_2' = \ldots = 0$
and $G_1 = G_2 = \ldots = 0$

at $\eta = \infty$: $F_1' = G_1 = 1$, $G_1' = F_2' = \ldots = 0$
and $G_1' = G_2' = \ldots = 0$

where primes denote derivatives with respect to η. $\overline{F_i}$ and $\overline{G_i}$ denote nonhomogeneous terms which depend only on functions of lower order. For i = 0, the nonhomogeneous terms are $\overline{F_o} = \overline{G_o} = -1$ and the solutions for F_o' and G_o' are obtained in closed form for any values of γ and σ as

$$F_o' = G_o = 1 - (1+\eta^2/2)\mathrm{erfc}(\eta/2) + \eta/\pi^{1/2}\, e^{-\eta^2/4} \tag{2.19}$$

where

$$\mathrm{erfc}(\eta/2) = \frac{2}{\sqrt{\pi}} \int_{\eta/2}^{\infty} e^{-\theta^2}\, d\theta$$

Higher order functions for i = 1, 2, ..., require numerical solutions.

The first three terms of Eq. (2.18) were numerically evaluated by Cohen [10]. Mirels [2] pointed out that the boundary layer profile on a semi-infinite flat plate having a constant acceleration after initially being at rest is the same as the velocity profile given by Eq. (2.19). A modified Karman-Pohlhausen integral method used by Trimpi and Cohen [11] to solve the expansion wave boundary layer gives velocity profiles which agree with those from the finite series expansion [10]. The velocity profiles obtained by Srinivasan [5] and presented in Fig. 2 agree well with the solutions of Cohen [10] and Trimpi and Cohen [11] and are used herein for the approximate stability analyses.

3.0 STABILITY ANALYSES

For incompressible steady flow, Squire [58] showed that the stability problem for a three-dimensional parallel flow problem can be transformed to an equivalent two-dimensional problem at a lower Reynolds number. Conrad and Criminale [23] state that Squire's theorem can be extended to time dependent incompressible flows. From Squire's theorem, it may be concluded that for the nearly incompressible subsonic flow developed within expansion waves, two-dimensional disturbances are more dominant in promoting boundary layer instability than are three-dimensional disturbances. Similar conclusions were reached by Ostrach and Thornton [7] for the boundary layer flows developed behind weak shock waves (Mach number $M_s \approx 1$). However, for shock wave Mach numbers larger than 2.18 the approximate method of Lees and Lin [36] used to find the critical Reynolds number gave the result that the boundary layer is infinitely stable to two-dimensional disturbances.

In the absence of external disturbances, we may assume that transition from laminar to turbulent flow is initiated by instabilities of the laminar expansion wave boundary layer which take the form of two-dimensional velocity disturbances known as Tollmien-Schlichting waves. The disturbances are initially small and do not affect the mean flow. The exponential growth rate of the disturbances is initially independent of disturbance amplitude. The growth rate becomes dependent on disturbance amplitudes which are large enough to affect the mean laminar flow. When the disturbances become sufficiently large, non-linear effects become important. Soon after the non-linear region, spots of turbulent flow appear and grow in size as they move downstream. The spots coalesce resulting in fully turbulent flow.

Important objectives of stability theory are first to find a minimum

critical Reynolds number below which all disturbances are damped, second to specify which disturbances will amplify under the given flow conditions, and third to find the disturbance that has the most amplification as an aid in predicting the location of fully turbulent flow. Smith et al. [56] have shown good agreement of a prediction of transition based on an amplification factor of e^{10} with available airfoil data from low free stream turbulence tests. Smith's criteria for transition does not agree with transition data for some classes of boundary layer flows, and in particular does not agree with transition data for the expansion wave boundary layer examined herein.

Analytic solutions for the stability of the Blasius boundary layer were first obtained in 1929 by Tollmien and Schlichting [25] and were continuously refined as analytic and numerical methods improved [27]. The existence of Tollmien-Schlichting waves was not confirmed until 1948 by Schubauer and Skramstad [29] using a low turbulence wind tunnel. The results have since been confirmed by other investigators and recently by Ross et al. [30]. The stability of the Blasius boundary layer and other parallel flows is well presented in Ref. 26. For steady boundary layer flows, Saric and Nayfeh [28] have shown the critical Reynolds number to be less than that derived from parallel stability theory due to non-parallel flow effects.

In the inviscid limit (large Reynolds numbers), Lord Rayleigh [31] in 1880 showed that a necessary condition for the boundary layer to become unstable is that it has a point of inflection. Furthermore, Fjørtoft [32] has shown that for instability to occur, the absolute value of the vorticity of the primary flow must have a maximum in the domain of flow.

The point of inflection criteria was used by Tollmien [24] and

Schlichting [25] to show that since the viscosity of air increases with temperature, that a heating of the boundary layer would induce the occurrence of an inflection point in the velocity profile and thus make the velocity profile less stable. The point of inflection criteria can also be used to show that an accelerated flow is more stable, while a de-accelerated flow has a point of inflection and is thus less stable.

3.1 Approximate Stability Analyses and Application to the Quasi-Steady Expansion Wave Boundary Layer

Prior to attempting a solution to the present stability problem, it is useful to look into approximate methods for the prediction of the minimum critical Reynolds number. The use of such methods for predicting the stability and transition of some steady or quasi-steady, incompressible flows is well presented in Ref. 21. In this section, the applicability of the limiting assumptions of quasi-steady and quasi-parallel stability for the expansion wave boundary layer flows under investigation are demonstrated and results from Lees approximate method [36] are obtained for the critical Reynolds number. The disturbance equations describing the more detailed problem are first introduced to demonstrate the need for the approximations made and the usefulness of the approximate methods. The detailed problem is further examined in Sec. 3.2 and Sec. 3.3.

The disturbance field is assumed to be two-dimensional on the basis of Conrad and Criminale's result [23] that flow unsteadiness does not alter the conclusions of Squire's theorem [58]. The linearized differential equation describing the disturbances for accelerating unsteady and incompressible flow is obtained by the substitution of the disturbed stream function $\tilde{\psi}(x,y,t) = \bar{\psi}(x,y,t) + \psi(x,y,t)$ in the vorticity transport equation. The disturbance $\psi(x,y,t)$ is assumed to be much

smaller than the mean value of the stream function $\bar{\psi}(x,y,t)$. By retaining only linear terms and subtracting out the mean vorticity transport equation, the disturbance equation is then as follows:

$$(\nabla^2\psi)_t + \bar{\psi}_y(\nabla^2\psi)_x + (\nabla^2\bar{\psi})_x\psi_y - \bar{\psi}_x(\nabla^2\psi)_y$$

$$-(\nabla^2\bar{\psi})_y\psi_x = \frac{1}{Re}\nabla^4\psi \qquad (3.1)$$

Subscripts x, y and t denote derivatives with respect to those quantities. All quantities have been non-dimensionalized by means of a representative reference mean velocity u_R along x, measured with respect to the walls and a representative reference length δ_R of the flow for the y direction. The Reynolds number is $Re = u_R\delta_R/\nu_R$, where ν_R is a representative kinematic viscosity μ_R/ρ_R, $\nabla^2 = \partial^2/\partial x^2 + \partial^2/\partial y^2$, and $\nabla^4 = \partial^4/\partial x^4 + 2(\partial^4/\partial x^2\partial y^2) + \partial^4/\partial y^4$. The fluctuating velocity components u' and v' can be obtained from the definition of the stream function and are given as follows:

$$u' = \frac{\partial\psi}{\partial y}; \quad v' = -\frac{\partial\psi}{\partial x} \qquad (3.2)$$

For steady flow, assume ψ takes the customary form

$$\psi(x,y,t) = \phi(y)e^{i(kx-\omega t)} \qquad (3.3)$$

where $k = k_r + ik_i$ and $\omega = \omega_r + i\omega_i$ are complex quantities. k_r and ω_r are the wave number and frequency of the disturbance respectively, k_i and ω_i are the space and time amplification rates, either of which can be set equal to zero depending on the framework in which the problem is to be analyzed. The wave length λ is given by the expression $k_r = \frac{2\pi}{\lambda}$. Equation (3.1) then takes the well known Orr-Sommerfeld form (Ref. 59):

$$(\phi'' - k^2\phi)(U-c) - U''\phi = [\frac{1}{ikRe}][\phi'''' - 2k^2\phi'' + k^4\phi] \qquad (3.4)$$

Here $U = U(y)$ is the distribution of mean velocity parallel to the plane surface. Primes denote derivatives with respect to y. The phase velocity $c = \omega/k = c_r + ic_i$ is a complex quantity. c_r is the velocity of propagation of the disturbance phase in the x direction and c_i is related to the degree of damping or amplification.

For time-dependent flows, an estimated prediction of stability from Eq. (3.4) cannot be made solely on whether the disturbances grow or decay but might be made in terms of whether the ratio of the disturbance energy to the mean flow energy decreases or increases. Shen [22] thus introduced the concept of a growth factor given as follows:

$$\text{Gro} = \left(\frac{1}{2E}\right)\frac{\partial E}{\partial t} \tag{3.5}$$

where

$$E = \frac{\int_0^\delta \int_0^\lambda (u'^2 + v'^2)\,dx\,dy}{\lambda \int_0^\delta U^2\,dy} \tag{3.6}$$

λ is the wave length of the disturbance and δ is the local boundary layer thickness. Other criteria for the stability of time dependent flows, including whether or not the energy of the disturbances $\left(\int_0^\delta \int_0^\lambda (u'^2 + v'^2)\,dx\,dy\right)$ grows in time, were investigated by Conrad and Criminale [23]. These criteria were applied to oscillating and accelerating Couette and Poiseuille flows with the result that Shen's method produced the most reliable results. To use Shen's criteria, calculation of the eigenvalues k and c as well as the eigenfunctions $\phi(y)$ of the Orr-Sommerfeld equation (Eq. 3.4) are required.

For a boundary layer type flow of the form $U = T(t/t_o)U(y)$, where t_o is a characteristic mean flow time, Shen demonstrated that:

$$\text{Gro} < 0 \quad \text{if} \quad kc_i < \left(\frac{T'}{T^2}\right)\left(\frac{1}{t_o}\right) \tag{3.7}$$

where

$$T' = \partial T/\partial(t/t_o) \tag{3.8}$$

For Gro > 0, the boundary layer is momentarily unstable while for Gro < 0, it is stable.

For unsteady boundary layers, Shen [22] showed that in order for a quasi-steady approach to be valid, the characteristic time of the base flow must be much larger than $Re^{1/3}$ times the characteristic disturbance time. The quasi-steady assumption implies that the boundary layer profile and thickness change sufficiently slowly so as not to alter the disturbances which thus must have a much shorter characteristic time. This is somewhat analogous to the quasi-parallel assumptions used in the stability analysis of Falkner-Skan type flows and flows around submerged bodies.

The characteristic time of the mean flow t_f may be represented as $t_f = u_e/(\frac{\partial u_e}{\partial t})$ and that of the disturbances, t_D, may be roughly approximated as $t_D = \delta_R/u_e$. The ratio t_f/t_D is thus equal to $u_e^2/(\delta_R \partial u_e/\partial t)$. This must be much larger than $Re^{1/3}$ to satisfy Shen's criteria, where Re is based on $u_R = u_e$. For the expansion wave boundary layer,

$$u_e = \beta a_o s \quad \text{and} \quad \delta \simeq 4\sqrt{\nu_o s t} \tag{3.9}$$

so that

$$t_f/t_D = \frac{\beta a_o s^2 t}{4\sqrt{\nu_o s t}\,(1-\varepsilon s)} \quad . \tag{3.10}$$

For $s < 1$, $s \ll 1$ so that this becomes

$$t_f/t_D = \frac{\beta a_o s^{3/2}}{4}\sqrt{t/\nu_o} \tag{3.11}$$

and

$$Re^{1/3} = (4\beta a_o)^{1/3}(t/\nu_o)^{1/6}s^{1/2} \tag{3.12}$$

The largest time derivatives occur at stations x_s closest to the diaphragm location (2 feet) and at the wavehead. Under these conditions, and at a typical initial pressure level of five atmospheres, it can be shown that $t_f/t_D >> Re^{1/3}$ for $s >> .017$. Since the observed expansion-wave boundary-layer transitions occur at $s > .4$, the criteria for a quasi-steady, quasi-parallel stability analysis would seem to be reasonably well satisfied. This leads to some degree of confidence in the use of steady-flow approximate methods for stability prediction.

Lin [12] derived an approximate method for estimating the critical Reynolds number for the incompressible boundary layer. Lin's method was used by Tetervin and Levine [44] to predict the point of instability for the boundary layers developed under the influence of a pressure gradient and with blowing or suction. The results are well correlated with a shape factor $H = \delta^*/\theta$ (δ^* is the displacement thickness and θ the momentum thickness) and agree well with solutions to the Orr-Sommerfeld equation for critical Reynolds numbers by others [27,13-16]. The displacement thickness and momentum thickness for a compressible boundary layer can be defined as follows:

$$\delta^* = \int_o^\infty (1 - \frac{\rho}{\rho_e}\frac{u}{u_e})dy, \quad \theta = \int_o^\infty (1 - \frac{u}{u_e})\frac{\rho}{\rho_e}\frac{u}{u_e}\,dy \tag{3.13}$$

The ratio $H = \delta^*/\theta$ derived for the expansion wave boundary layer is a function of s only as shown in Fig. 3. The Reynolds number based on θ is zero at the wavehead and increases rapidly as s and H also increase; the boundary layer thus becomes less stable. For incompressible flow,

it is expected that the increasing Re_θ and H will intersect the curve derived by Tetervin and Levine at some point H_{cr} and $Re_{\theta_{cr}}$ which will indicate the point of instability. Figure 4 illustrates this process along the particle path of particles observed to undergo transition at 8.16 feet from the diaphragm location. For values of s in excess of .4, H is larger than the value for an incompressible Blasius boundary layer even though the pressure gradient is still quite favorable.

Lees [36] obtained a similar formula to that of Lin for the compressible boundary layer given by:

$$Re_{\delta^*_{cr}} = 25\left(\frac{u'_w \delta^*}{c^4}\right)\frac{\left(\frac{T_c}{T_e}\right)^{1.76}}{\sqrt{1-Me^2(1-c)^2}} \tag{3.14}$$

and

$$k_{cr} = u'_w c \tag{3.15}$$

where u'_w is the dimensionless velocity gradient at the wall, c is the dimensionless wave speed, Me is the Mach number of the inviscid flow and T_c is the temperature at the point in the boundary layer where u = c (i.e., at the critical point). The critical point is found by searching for the location in the boundary layer where the following expression is satisfied:

$$.58 + \pi \frac{u'_w c}{\left(\frac{T_w}{T_e}\right)} \left[\frac{(T/T_e)^2}{u'^3} \frac{d}{dy} \left(\frac{u'}{(T/T_e)}\right)\right]_{u=c} = 0 \tag{3.16}$$

Lees approximate method has been used by many for predicting the stability of steady compressible flows; Tetervin [37] has used this method for predicting the stability of Falkner-Skan type flows with heating. Ostrach et al. [7] have also used Lees' method to predict the stability of flows behind moving shock waves of different strength and shows the significant effect of wall cooling. Ostrach found very good agreement between the

prediction and the value of $Re_{\delta^*_{cr}}$ obtained from the solution to the Orr-Sommerfeld equation for very weak shocks.

For the expansion wave boundary layer, Srinivasan's [5] velocity and temperature profiles were used in conjunction with Eq. (3.14) to predict the point of instability. Figure 5 shows the variation of $Re_{\theta_{cr}}$ with the similarity parameter s. Figure 6 shows the variation of c_{cr} and k_{cr} with s.

At s = 0, H = 2.16 and $Re_{\theta_{cr}} = 9.2 \times 10^3$ is obtained from Tetervin and Levine's results [44] presented in Fig. 3, compared with 12.3×10^3 derived from direct use of Lees' formula. The difference is due to the velocity profile at s = 0 not being the same as that of the Falkner-Skan profile corresponding to H = 2.16. The agreement between the two values of $Re_{\theta_{cr}}$ is considered to be quite good and the approximate method of Lees can be used for comparison with experimental data and as a starting point for stability calculations of the Orr-Sommerfeld equation.

3.2 Numerical Solution of the Orr-Sommerfeld Equation for the Expansion Wave Boundary Layer

In order to confirm the accuracy of Lees' or Lin's method as applied to the expansion wave flow, it is desired to make some comparison with results obtained by more exact solution of the quasi-steady, quasi-parallel stability model. Towards this purpose, the Orr-Sommerfeld equation (Eq. 3.4) was solved numerically to obtain the quasi-steady, quasi-parallel neutral stability curve. Because of the large stabilizing pressure gradients in the expansion wave, the Reynolds numbers for the neutral stability curve are much larger than those typically encountered in stability studies. The large Reynolds numbers made this numerical analysis considerably more difficult than at first anticipated. The calculations were therefore limited to the case of the boundary layer flow at the expansion wave head

($s = 0$) which can be assumed to be incompressible. The velocity profile close to the expansion wave head ($s \approx 0$) is identical to the unsteady laminar boundary layer formed on a semi-infinite flat plate undergoing a constant acceleration from rest (Ref. 2).

The technique used to find the neutral stability curve is the well known shooting method. The method of orthonormalization is used to improve accuracy. The eigenvalues k and c were specified to be real and the values of k and c satisfying the boundary conditions at the wall were searched for. The integration is started outside the boundary layer at $\eta = 6$ which is 1.5 times the boundary layer thickness and where the asymptotic behavior of the eigenfunction solutions are known. Outside the boundary layer, the inviscid form of the Orr-Sommerfeld equation (Eq. 3.4) is given by:

$$[\frac{i}{Re}][(\phi'''' - 2k^2\phi'' + k^4\phi)] + (k-\omega)(\phi'' - k^2\phi) = 0 \qquad (3.17)$$

The solutions to the fourth order differential equation (Eq. 3.17) are

$$\phi_1 = e^{-k\eta}; \quad \phi_2 = e^{-\sqrt{k^2+iRe(k-\omega)}\,\eta}$$

$$\phi_3 = e^{k\eta}; \quad \phi_4 = e^{\sqrt{k^2+iRe(k-\omega)}\,\eta}$$

Where $\phi = \phi_1 + A.\phi_2 + B.\phi_3 + C.\phi_4$. Since ϕ must decay as η becomes large, $B = C = 0$. At the wall, the following boundary conditions must be satisfied

(a) $\phi_1 + A\phi_2 = 0$

and (3.18)

(b) $\phi_1' + A\phi_2' = 0$

The asymptotic solutions ϕ_1 and ϕ_2 are used to integrate the Orr-

Sommerfeld equation (Eq. 3.4) from $\eta = 6$ to the wall. At the wall the second of the boundary conditions is used to determine A. The value of A is then used to determine if the first boundary condition is satisfied. If not, new eigenvalues c and k are used and the process repeated until the boundary conditions are satisfied to within 10^{-5} accuracy. The values of ϕ_1, ϕ_2, ϕ_1' and ϕ_2' determined from the final orthonormalization performed at the wall are used for the above mentioned convergence test.

A program called STABIL was developed for the above mentioned purpose. The program used a single precision, predictor-corrector type subroutine called CHPCG which performed the integration of the Orr-Sommerfeld equation for different eigenvalues. At several stages along the path of integration, the solution vectors $\bar{\phi}_1$ and $\bar{\phi}_2$ were orthonormalized using the Gram-Schmidt procedure. The solution vectors $\bar{\phi}_1$ and $\bar{\phi}_2$ are given by the solutions ϕ_1, ϕ_2 and their derivatives as follows:

$$\bar{\phi}_1 = (\phi_1, \phi_1', \phi_1'', \phi_1''')$$

$$\bar{\phi}_2 = (\phi_2, \phi_2', \phi_2'', \phi_2''')$$

For each orthonormalization performed, $\bar{\phi}_1$ and $\bar{\phi}_2$ were normalized so that they both became unit vectors. The normalized vector $\bar{\phi}_2$ was then corrected by the Gram-Schmidt procedure so that it was orthogonal to $\bar{\phi}_1$ (i.e., $\bar{\phi}_1 \cdot \bar{\phi}_2 = 0$). The integration was resumed using the new orthonormal vector solutions. Orthonormalizations were performed at the beginning of the integration ($\eta = 6$) and at the wall ($\eta = 0$) as well as in between.

The use of orthogonalization or orthonormalization ensures that the solutions ϕ_1 and ϕ_2 remain orthogonal and its use is standard in correcting for error built up due to integration, especially at large Reynold numbers as is the case in the present study. An optimization technique was used

to find the eigenvalues which gave the smallest value of the first boundary condition. Optimization subroutine CONGRA which uses the conjugate gradient method, Ref. 52, was used to find the eigenvalues to four significant figures. The program was first tested on the plane Poiseuille flow and the Blasius boundary layer flow. The search for the eigenvalues was started using previous results [27,39] for the test problems and using the approximate method results already obtained in Sec. 3.1 for the present problem ($s = 0$).

The program was tested for the Blasius boundary layer and yielded eigenvalues which agreed with Jordinson [27] to the fourth decimal place. These are summarized in Table I. The eigenfunctions of the Blasius boundary layer for $Re_{\delta^*} = 998$, $k = .3086 - i\ .0057$ and $\omega = .112$ were computed <u>without</u> orthonormalizing. For ϕ_r, agreement is good with Jordinson's results even though the integration was started at $y/\delta^* = 3.4$ rather than 6. The imaginary part of the eigenfunction ϕ_i and its derivative ϕ_i' are much smaller than the real parts ϕ_r and ϕ_r', so that the relative error for $y/\delta^* > 1.2$ was much larger. The errors are due to the orthogonalization not being used for the eigenfunction computations. Attempts were made to perform the eigenfunction evaluations using orthogonalization but the subroutine developed did not succeed for unknown reasons. The use of orthogonalization for eigenfunction evaluation is almost a necessity for high Reynolds numbers ($Re_{\delta^*} > 1000$).

Results for the Expansion Wave Boundary Layer

For the expansion wave boundary layer, the flow is incompressible at the wave head ($s = 0$) and the velocity $U(\eta)$ may be given by Eq. (2.18) as follows:

$$U(\eta) = 1 - \left(1 + \frac{\eta^2}{2}\right)\mathrm{erfc}\left(\frac{\eta}{2}\right) + \frac{\eta}{\pi^{1/2}}\, e^{-\eta^2/4}$$

This expression for $U(\eta)$ is used in Eq. (3.4) to determine the eigenvalues k_r and ω_r on the neutral stability curve. The starting point of the integration was chosen as $\eta = 6$ at which point $U = 1.0000$ and $U'' = -.00005$. Due to the large Reynolds numbers involved, the eigensolution ϕ_2 was found to be very small ($|\phi_2| < e^{-300}$) so that when squared in the first orthonormalization, it was set equal to zero. ϕ_2 and its derivatives were multiplied by a constant (e^{200}) prior to the first orthonormalization. Due to the large Reynolds numbers involved, 24 orthogonalizations and 384 equal steps were used in integrating from $\eta = 6$ to $y = 0$ for $Re_{\delta*} < 30{,}000$. For $Re_{\delta*} > 30{,}000$, the number of steps was doubled.

At the wall, the second boundary condition of Eq. (3.18) was used to evaluate the constant A which was used to test if the first boundary condition ($\phi = 0$) was satisfied. If not, new eigenvalues were selected and the process outlined above repeated. The second boundary condition could not be satisfied exactly except within approximately 5×10^{-5}.

The search for eigenvalues on the neutral stability curve is conducted by setting $k_i = \omega_i = 0$ and finding k_r and ω_r for given $Re_{\delta*}$. From the approximate analysis of Sec. 3.2, $Re_{\delta*_{cr}} \approx 26609$, $k_{cr} = .4039$, and $\omega_{cr} = .0728$. The numerical integration for $Re_{\delta*} = 26609$ gave $k_{cr} = .4085$ and $\omega_{cr} = .0786$. Neutral curve eigenvalues were subsequently determined for other values of $Re_{\delta*}$. The resulting eigenvalues are shown in Table II and the neutral curve is shown in Fig. 7. The critical Reynolds number $Re_{\delta*_{cr}}$ is found to be 25488, about 4% less than that predicted by Lees' approximate method. The computer program used is further discussed in Appendix A.

3.3 The Method of Multiple Scales for the Stability of Unsteady Laminar Boundary Layers

Section 3.2 dealt with numerical solution of the Orr-Sommerfeld equation describing a quasi-parallel, quasi-steady model of the stability of the expansion-wave boundary layer. The nature of this flow permits development of a singular perturbation technique to obtain more accurate results in the case of small departures from this limiting quasi-parallel, quasi-steady model. This section outlines such a perturbation analysis in fairly general terms, applicable to any unsteady boundary layer with such small departures. Full numerical application of the method to a specific problem is a large undertaking and was beyond the scope of the present study. However, the first step of such application (and probably the most difficult) is the solution of the limiting quasi-steady, quasi-parallel model, which was done as has been described in Sec. 3.2.

The perturbation method used is an extension of the method of multiple scales used by Saric and Nayfeh [28] to account for spatial nonparallel effects only. The mean boundary layer flow is assumed to vary in both time and space much more slowly than the disturbance field. For simplicity in the initial development of the method the unsteady mean flow is assumed to be incompressible, and both the mean flow and the disturbance field are assumed two-dimensional. The starting point is therefore Eq. (3.1) governing the (linearized) disturbance stream function ψ

$$(\nabla^2\psi)_t + \bar{\psi}_y(\nabla^2\psi)_x + (\nabla^2\bar{\psi})_x\psi_y - \bar{\psi}_x(\nabla^2\psi)_y - (\nabla^2\bar{\psi})_y\psi_x = \frac{1}{Re}\nabla^4\psi \tag{3.1}$$

where $\bar{\psi} = \bar{\psi}(x,y,t)$ is the mean flow stream function which satisfies

$$\nabla^2\bar{\psi}_t + \bar{\psi}_y\nabla^2\bar{\psi}_x - \bar{\psi}_x\nabla^2\bar{\psi}_y - \frac{1}{Re}\nabla^4\bar{\psi} = 0 \tag{3.19}$$

The boundary conditions on ψ are assumed such that $U' = \partial\psi/\partial y$ and $V' = -\partial\psi/\partial x$ are 0 at $y = 0$ and vanish as $y \to \infty$. Equation (3.19) is the exact Navier Stokes equation governing the mean flow. The customary boundary layer representation of the mean flow is the leading approximation to Eq. (3.19) for large Reynolds number $Re = u_R\delta_R/\nu_R$. The boundary conditions on the mean flow velocity components $U = \partial\bar{\psi}/\partial y$ and $V = -\partial\bar{\psi}/\partial x$ may be taken as $U = V = 0$ at $y = 0$ and $U = U_e(x,t)$ at $y \to \infty$.

The dimensional quantities δ_R and u_R, by which $x,y,t,\bar{\psi}$ and ψ are made nondimensional, specify a representative dimension of the mean flow along y and a representative velocity of the mean flow along x, respectively. It is assumed that the disturbance field is characterized by time and x- length scales of roughly the order of magnitudes of δ_R/u_R and δ_R, respectively, i.e., by unit magnitude of x and t. The spatial variation of the mean flow along x is assumed to be characterized by a "slow" space variable $x_1 = \varepsilon x$, where $\varepsilon << 1$ is a small parameter yet to be chosen. The introduction of x_1 in place of x in Eq. (3.19) for the mean flow then suggests the introduction of an analogous slow time variable $t_1 = \varepsilon t$ to characterize the mean-flow time variation, and further indicates a convenient choice for ε to be $\varepsilon = 1/Re = \nu_R/(u_R\delta_R)$. To summarize the functional dependencies at this point, we now have $\psi = \psi(x,x_1,y,t,t_1;\varepsilon)$ and $\bar{\psi} = \bar{\psi}(x_1,y,t_1;\varepsilon)$.

The perturbation analysis to follow requires $\varepsilon << 1$, or $Re >> 1$. It is of interest to note that ε may be expressed as

$$\varepsilon = \frac{\delta_R/u_R}{\delta_R^2/\nu_R}$$

Written in this way, ε represents the ratio of two characteristic times: the time δ_R/u_R, which is of the order of the disturbance time, and δ_R^2/ν_R which is of the order of the time for shear effects to diffuse across the mean flow. Thus $\varepsilon << 1$ implies that the disturbance shear field is localized and dependent primarily on local instantaneous conditions in the mean flow. The interpretation of Shen's criterion for quasi-steady stability (discussed in Sec. 3.1) in terms of ε gives $\varepsilon << (\nu_R t_f/\delta_R^2)^{3/2}$ as the requirement, where t_f is the time characterizing change of the mean flow. If $t_f \geq \delta_R^2/\nu_R$, then Shen's criterion is thus always satisfied when $\varepsilon << 1$. In particular, this will always be so for mean flows which are near quasi-steady, since in that case $t_f >> \delta_R^2/\nu_R$ tends to apply. When $t_f < \delta_R^2/\nu_R$, smaller values of ε are presumably necessary in order to satisfy Shen's criterion.

Perturbation Equations

Extending the approach of Ref. 28, the disturbance stream function ψ is assumed to have the form

$$\psi = \phi(x_1, t_1, y; \varepsilon) e^{i\theta_o} \tag{3.20}$$

where the amplitude function ϕ depends on x_1, t_1, and ε, in addition to y. θ_o is a new independent variable of phase whose x and t derivatives

$$\begin{aligned} \partial\theta_o/\partial x &= k_o(x_1, t_1) \\ \partial\theta_o/\partial t &= -\omega_o(x_1, t_1) \end{aligned} \tag{3.21}$$

define disturbance wave number k_o and angular frequency ω_o, both of which are assumed to depend on x_1 and t_1 in general. Equation (3.1) is next transformed as regards the x and t derivatives of ψ by means of the relations

$$\frac{\partial}{\partial x} = k_o \frac{\partial}{\partial \theta_o} + \varepsilon \frac{\partial}{\partial x_1}$$

$$\frac{\partial}{\partial t} = -\omega_o \frac{\partial}{\partial \theta_o} + \varepsilon \frac{\partial}{\partial t_1}$$

The amplitude ϕ is then expanded as a power series in ε, i.e., $\phi = \phi_o(x_1,y,t_1) + \varepsilon\phi_1(x_1,y,t_1) + \ldots$, where $\varepsilon\phi_1 << \phi_o$, etc. is assumed. Likewise the x and y velocity components of the mean flow, U and V, respectively, are expanded in similar form, i.e., $U = U_o(x_1,y,t_1) + \varepsilon U_1(x_1,y,t_1) + \ldots$, and $V = \varepsilon V_o(x_1,y,t_1) + \varepsilon^2 V_1(x_1,y,t_1) + \ldots$. U_o and V_o are thus the leading boundary layer approximations for the mean flow velocities; U_1, V_1 etc. represent higher order boundary layer effects. When like coefficients of the various powers of ε are finally equated, the equations governing ϕ_o and ϕ_1 are obtained as follows:

$$L(\phi_o) = \left(\frac{\partial^2}{\partial y^2} - k_o^2\right)^2 \phi_o - iRek_o\left[\left(U_o - \frac{\omega_o}{k_o}\right)\left(\frac{\partial^2 \phi_o}{\partial y^2} - k_o^2 \phi_o\right) - \frac{\partial^2 U_o}{\partial y^2}\phi_o\right] = 0 \tag{3.22}$$

with boundary conditions

$$\begin{aligned} &\phi_o = \partial\phi_o/\partial y = 0 \text{ at } y = 0 \\ &\phi_o \to 0 \text{ as } y \to \infty \end{aligned} \tag{3.23}$$

$$L(\phi_1) = [Re(2k_o\omega_o - 3U_ok_o^2 - \frac{\partial^2 U_o}{\partial y^2}) + 4ik_o^3]\frac{\partial\phi_o}{\partial x_1} + (ReU_o - 4ik_o)\frac{\partial^3\phi_o}{\partial y^2\partial x_1}$$

$$+ ReV_o(\frac{\partial^3\phi_o}{\partial y^3} - k_o^2\frac{\partial\phi_o}{\partial y}) - Re\frac{\partial^2 V_o}{\partial y^2}\frac{\partial\phi_o}{\partial y}$$

$$+ [(Re\omega_o - 3ReU_ok_o + 6ik_o^2)\phi_o - 2i\frac{\partial^2\phi_o}{\partial y^2}]\frac{\partial k_o}{\partial x_1}$$

$$+ iRek_o[U_1(\frac{\partial^2\phi_o}{\partial y^2} - k_o^2\phi_o) - \frac{\partial^2 U_1}{\partial y^2}\phi_o]$$

$$- Rek_o^2\frac{\partial\phi_o}{\partial t_1} + Re\frac{\partial^3\phi_o}{\partial y^2\partial t_1} - 2Rek_o\phi_o\frac{\partial k_o}{\partial t_1} \tag{3.24}$$

with boundary conditions

$$\begin{aligned} &\phi_1 = \partial\phi_1/\partial y = 0 \text{ at } y = 0 \\ &\phi_1 \to 0 \text{ as } y \to \infty \end{aligned} \tag{3.25}$$

Equation (3.22) governing ϕ_o is seen to be identical in form to Eq. (3.4), the Orr-Sommerfeld equation for steady parallel base flow, except that k_o, ω_o, and U_o now depend on x_1 and t_1. Equation (3.22) thus defines a secular equation of the form $F(\omega_o,k_o,x_1,t_1,Re) = 0$. For given values of x_1, t_1, and Re, the eigenvalues k_o and ω_o and the eigenfunction ϕ_o are thus determined as for the case of a steady parallel base flow. However, ϕ_o is only so determined to within an arbitrary multiplying function $A = A(x_1,t_1)$ which will depend on x_1 and t_1 in general. In order to obtain a valid leading approximation for ϕ_o, $A(x_1,t_1)$ must then be chosen such as to satisfy a certain solvability condition on Eq. (3.24) governing ϕ_1.

Along with the secular equation $F(\omega_o,k_o,x_1,t_1,Re) = 0$ we have

the implied functional relations $\omega_o = \omega_o(x_1,t_1)$ and $k_o = k_o(x_1,t_1)$. For given values of x_1, t_1, and Re there are thus three relations to be satisfied by ω_o and k_o. Thus for arbitrary changes dx_1 and dt_1 in x_1 and t_1 at a fixed value of Re, the corresponding changes $d\omega_o$ and dk_o cannot be independent but must be uniquely related, i.e.,

$$\left(\frac{\partial\omega_o}{\partial k_o}\right)_{Re} = v_g \tag{3.26}$$

where v_g is a group velocity dependent on x_1, t_1, Re, k_o, ω_o.

Because $k_o = \partial\theta_o/\partial x$ and $\omega_o = -\partial\theta_o/\partial t$, it follows that $\partial k_o/\partial t = -\partial\omega_o/\partial x$, or,

$$\frac{\partial k_o}{\partial t_1} = -\frac{\partial\omega_o}{\partial x_1} \tag{3.27}$$

If the mean flow depends on both x_1 and t_1, as for the expansion wave boundary layer, then both k_o and ω_o will depend on x_1 and t_1 also. If the mean flow is steady, i.e., independent of t_1, then $\partial k_o/\partial t_1 = 0$ and therefore $\partial\omega_o/\partial x_1 = 0$ from Eq. (3.27). In this case k_o varies with x_1 but ω_o does not, and $v_g = 0$. If the mean flow is independent of x_1 then $\partial\omega_o/\partial x_1 = 0$. It then follows from Eq. (3.27) that ω_o varies with t_1 but k_o does not, and $v_g = \infty$. An example here is the mean flow generated in the Rayleigh-type problem, i.e., an infinite plane wall undergoing acceleration. The group velocity v_g relates the x_1 and t_1 derivatives of k_o and ω_o. For subsequent use the pertinent relations may be summarized as follows:

$$v_g = \frac{\partial\omega_o/\partial x_1}{\partial k_o/\partial x_1} = \frac{\partial\omega_o/\partial t_1}{\partial k_o/\partial t_1} = -\frac{\partial k_o/\partial t_1}{\partial k_o/\partial x_1} = -\frac{\partial\omega_o/\partial t_1}{\partial\omega_o/\partial x_1} \tag{3.28}$$

These relations follow from the differential expressions for $d\omega_o$ and dk_o.

Regarding the nonhomogeneous Eq. (3.24) for ϕ_1, the right side terms

are associated with the following departures from the case of a parallel steady base flow: a dependence of ϕ_o and k_o on x_1 and t_1, a normal velocity component εV_o, and a higher-order boundary-layer velocity increment εU_1.

Method of Solution

As previously mentioned, ϕ_o is only determined from Eq. (3.22) to within a multiplying function $A(x_1,t_1)$, so that (following the notation of Ref. 28) ϕ_o may be expressed in the form

$$\phi_o = A(x_1,t_1)\zeta(y;x_1,t_1) \tag{3.29}$$

where $L(\zeta) \equiv 0$, with boundary conditions on ζ the same as Eq. (3.23). The condition determining A is the solvability condition for Eq. (3.24), which is that the right side or non-homogeneous terms be orthogonal to the eigenfunction $\zeta^*(y;x_1,t_1)$ which solves the adjoint homogeneous equation

$$L^*(\zeta^*) = \left(\frac{\partial^2}{\partial y^2} - k_o^2\right)^2\zeta^* - iRek_o\left[\left(U_o - \frac{\omega_o}{k_o}\right)\left(\frac{\partial^2\zeta^*}{\partial y^2} - k_o^2\zeta^*\right) + 2\frac{\partial U_o}{\partial y}\frac{\partial\zeta^*}{\partial y}\right] = 0 \tag{3.30}$$

with boundary conditions $\zeta^* = \frac{\partial\zeta^*}{\partial y} = 0$ at $y = 0$

$$\zeta^* \to 0 \text{ as } y \to \infty.$$

Substitution of $\phi_o = A\zeta$ into the right side of Eq. (3.24) gives $L(\phi_1) = ReJ$ where

$$J = [B_1\zeta + B_2 \frac{\partial^2\zeta}{\partial y^2}]\frac{\partial A}{\partial x_1} + [B_1 \frac{\partial\zeta}{\partial x_1} + B_2 \frac{\partial^3\zeta}{\partial y^2\partial x_1}$$

$$+ (B_3\zeta + B_4 \frac{\partial^2\zeta}{\partial y^2})\frac{\partial k_o}{\partial x_1} + B_5\zeta + B_6 \frac{\partial\zeta}{\partial y} + B_7 \frac{\partial^2\zeta}{\partial y^2}$$

$$+ B_8 \frac{\partial^3\zeta}{\partial y^3} + \frac{\partial^3\zeta}{\partial y^2\partial t_1} + B_9\zeta \frac{\partial k_o}{\partial t_1} + B_1 \frac{\partial\zeta}{\partial t_1}]A$$

$$+ [\frac{\partial^2\zeta}{\partial y^2} + B_{10}]\frac{\partial A}{\partial t_1} \tag{3.31}$$

and

$$B_1 = 2k_o\omega_o - 3U_ok_o^2 - \frac{\partial^2 U_o}{\partial y^2} + 4ik_o^3/Re$$

$$B_2 = U_o - 4ik_o/Re$$

$$B_3 = \omega_o - 3U_ok_o + 6ik_o^2/Re$$

$$B_4 = -2i/Re$$

$$B_5 = -ik_o(\frac{\partial^2 U_1}{\partial y^2} + k_o^2U_1)$$

$$B_6 = -\frac{\partial^2 V_o}{\partial y^2} - k_o^2V_o \qquad B_7 = ik_oU_1$$

$$B_8 = V_o \qquad B_9 = -2k_o \qquad B_{10} = -k_o^2$$

The solvability condition requiring orthogonality is then

$$\int_o^\infty J\zeta^* dy = 0$$

which can be expressed in the form

$$g_1 \frac{\partial \ell nA}{\partial x_1} - g_2 + f_1 \frac{\partial \ell nA}{\partial t_1} - f_2 = 0 \tag{3.32}$$

where

$$g_1 = -\int_0^\infty (B_1\zeta + B_2 \frac{\partial^2\zeta}{\partial y^2})\zeta^* dy$$

$$g_2 = \int_0^\infty [(B_1 + \frac{\partial^2 B_2}{\partial y^2})\zeta^* + 2 \frac{\partial B_2}{\partial y} \frac{\partial \zeta^*}{\partial y} + B_2 \frac{\partial^2 \zeta^*}{\partial y^2}]\frac{\partial \zeta}{\partial x_1} dy$$

$$+ \int_0^\infty [(B_3\zeta + B_4 \frac{\partial^2\zeta}{\partial y^2})\frac{\partial k_o}{\partial x_1} + B_5\zeta + B_6 \frac{\partial \zeta}{\partial y} + B_7 \frac{\partial^2\zeta}{\partial y^2} + B_8 \frac{\partial^3\zeta}{\partial y^3}]\zeta^* dy$$

$$f_1 = -\int_0^\infty (\frac{\partial^2\zeta}{\partial y^2} + B_{10}\zeta)\zeta^* dy$$

$$f_2 = \int_0^\infty (\frac{\partial^2\zeta^*}{\partial y^2} + B_{10}\zeta^*)\frac{\partial \zeta}{\partial t_1} + \int_0^\infty B_9 \frac{\partial k_o}{\partial t_1} \zeta\zeta^* dy \tag{3.33}$$

If A is expressed in the form $A = A_o e^{i\varepsilon\theta_1}$, where A_o is an arbitrary constant, then

$$\frac{\partial \ell nA}{\partial x_1} = i\varepsilon \frac{\partial \theta_1}{\partial x_1} = i \frac{\partial \theta_1}{\partial x} = ik_1(x_1,t_1)$$

$$\frac{\partial \ell nA}{\partial t_1} = i\varepsilon \frac{\partial \theta_1}{\partial t_1} = i \frac{\partial \theta_1}{\partial t} = -i\omega_1(x_1,t_1)$$

The leading approximationg for ψ then becomes

$$\psi \simeq \phi_o e^{i\theta_o} = A\zeta e^{i\theta_o} = A_o\zeta e^{i(\theta_o+\varepsilon\theta_1)} = A_o\zeta e^{i\theta}$$

where, in summary,

$$\theta = \theta_o + \varepsilon\theta_1$$

$$\frac{\partial\theta}{\partial x} = \frac{\partial\theta_o}{\partial x} + \varepsilon\frac{\partial\theta_1}{\partial x} = k_o(x_1,t_1) + \varepsilon k_1(x_1,t_1) = k(x_1,t_1;\varepsilon)$$

$$\frac{\partial\theta}{\partial t} = \frac{\partial\theta_o}{\partial t} + \varepsilon\frac{\partial\theta_1}{\partial t} = -\omega_o(x_1,t_1) - \varepsilon\omega_1(x_1,t_1) = -\omega(x_1,t_1;\varepsilon) \tag{3.34}$$

εk_1 and $\varepsilon\omega_1$, which depend on both x_1 and t_1 in general, are thus corrections to ω_o and k_o on account of the x_1 and t_1 dependence of the mean flow. In terms of ω_1 and k_1 Eq. (3.32) becomes

$$ik_1g_1 - g_2 - i\omega_1f_1 - f_2 = 0 \tag{3.35}$$

Equation (3.35) provides one relation determining ω_1 and k_1, and a second relation is therefore needed. To obtain this, consider the secular relation governing ω_o and k_o to be expressed in the form $\omega_o = f(k_o,x_1,t_1,Re)$ along with the implicit relations $\omega_o = \omega_o(x_1,t_1)$ and $k_o = k_o(x_1,t_1)$. These three relations lead to the result that $\left(\frac{\partial\omega_o}{\partial k_o}\right)_{Re} = v_g$, where the group velocity v_g is a unique point function of ω_o, k_o, x_1, t_1, Re. An arbitrary choice of k_o, x_1, t_1, and Re determines ω_o from the above secular relation and must therefore determine ω_1 and k_1 also. Thus, implicitly at least, we can similarly write $\omega_1 = g(k_o,x_1,t_1,Re)$ and $k_1 = h(k_o,x_1,t_1,Re)$, along with the implicit relations $\omega_1 = \omega_1(x_1,t_1)$ and $k_1 = k_1(x_1,t_1)$. It follows that the quantities $(\partial\omega_1/\partial k_o)_{Re}$ and $(\partial k_1/\partial k_o)_{Re}$ must also be point functions of ω_o, k_o, x_1, t_1, Re, as is v_g. The following differential expressions apply for arbitrary changes dx_1 and dt_1 with Re constant.

$$d\omega_1 = \frac{\partial\omega_1}{\partial x_1}dx_1 + \frac{\partial\omega_1}{\partial t_1}dt_1$$

$$dk_1 = \frac{\partial k_1}{\partial x_1}dx_1 + \frac{\partial k_1}{\partial t_1}dt_1$$

Because $\partial\omega_1/\partial k_o$ and $\partial k_1/\partial k_o$ are point functions and dx_1, dt_1 are arbitrary

changes, it then follows that $\partial\omega_1/\partial k_o = (\partial\omega_1/\partial x_1)/(\partial k_o/\partial x_1)$ (putting $dt_1 = 0$) and $\partial k_1/\partial k_o = (\partial k_1/\partial t_1)/(\partial k_o/\partial t_1)$ (putting $dx_1 = 0$). Dividing these last two expressions and using the fact that $\partial k_1/\partial t_1 = -\partial\omega_1/\partial x_1$ gives $(\partial\omega_1/\partial k_1)_{Re} = -(\partial k_o/\partial t_1)/(\partial k_o/\partial x_1) = v_g$. Now v_g does not depend on either ω_1 or k_1, so that the last expression can be integrated to give

$$\omega_1 = v_g k_1 \tag{3.36}$$

where the arbitrary constant must be zero in order that $\omega_1 = 0$ for $v_g = 0$ (which occurs when the base flow depends on x_1 only). In a less formal way Eq. (3.36) follows from interpreting $\varepsilon\omega_1$ and εk_1 as small differential changes $d\omega_o$ and dk_o in ω_o and k_o, respectively, and the result that $d\omega_o/dk_o = v_g$ for Re constant.

From Eqs. (3.35) and (3.36), ω_1 and k_1 may now be expressed as

$$\begin{aligned} i\omega_1 &= \frac{g_2 + f_2}{g_1 - v_g f_1} v_g \\ ik_1 &= \frac{g_2 + f_2}{g_1 - v_g f_1} \end{aligned} \tag{3.37}$$

Both ω_1 and k_1 will be nonzero when the mean flow varies with both x_1 and t_1. If the mean flow is steady then $v_g = 0$ and $f_2 = 0$ (Eq. (3.33)), so that $\omega_1 = 0$ and $ik_1 = g_2/g_1$ in that case, in agreement with Ref. 28. If the mean flow is independent of x_1 then $v_g = \infty$ and $g_2 = 0$ (Eq. (3.33), with $V_o = U_1 \equiv 0$), so that $k_1 = 0$ and $i\omega_1 = -f_2/f_1$.

Evaluation of ω_1 and k_1

In order to evaluate ω_1 and k_1 from Eq. (3.37) the functions f_1, f_2, g_1, g_2, and v_g must be evaluated. The f and g functions, defined in Eq.

(3.33), require determination of ζ, ζ^*, $\partial\zeta/\partial x_1$, $\partial\zeta/\partial t_1$, $\partial k_o/\partial x_1$, and $\partial k_o/\partial t_1$. ζ and ζ^* are obtained by solution of $L(\zeta) = 0$ and $L^*(\zeta^*) = 0$ (Eqs. 3.22 and 3.30, respectively) which have the same eigenvalues ω_o and k_o. Differentiation of $L(\zeta) = 0$ with respect to x_1 and t_1 leads to, respectively,

$$L\left(\frac{\partial\zeta}{\partial x_1}\right) = h_1 + h_2 \frac{\partial k_o}{\partial x_1} + h_3 \frac{\partial \omega_o}{\partial x_1}$$

$$L\left(\frac{\partial\zeta}{\partial t_1}\right) = h_4 + h_2 \frac{\partial k_o}{\partial t_1} + h_3 \frac{\partial \omega_o}{\partial t_1} \tag{3.38}$$

with boundary conditions

$$\frac{\partial\zeta}{\partial x_1} = \frac{\partial^2\zeta}{\partial x_1 \partial y} = \frac{\partial\zeta}{\partial t_1} = \frac{\partial^2\zeta}{\partial t_1 \partial y} = 0 \text{ at } y = 0$$

$$\frac{\partial\zeta}{\partial x_1} \text{ and } \frac{\partial\zeta}{\partial t_1} \to 0 \text{ as } y \to \infty$$

The h functions in Eq. (3.38) are

$$h_1 = iRek_o\left[\left(\frac{\partial^2\zeta}{\partial y^2} - k_o^2\zeta\right)\frac{\partial U_o}{\partial x_1} - \zeta\frac{\partial^3 U_o}{\partial y^2 \partial x_1}\right]$$

$$h_2 = 4k_o\left(\frac{\partial^2\zeta}{\partial y^2} - k_o^2\zeta\right) + iRe\left(U_o\frac{\partial^2\zeta}{\partial y^2} - 3U_o k_o^2\zeta + 2\omega_o k_o\zeta - \frac{\partial^2 U_o}{\partial y^2}\zeta\right)$$

$$h_3 = -iRe\left(\frac{\partial^2\zeta}{\partial y^2} - k_o^2\zeta\right)$$

$$h_4 = iRek_o\left[\left(\frac{\partial^2\zeta}{\partial y^2} - k_o^2\zeta\right)\frac{\partial U_o}{\partial t_1} - \zeta\frac{\partial^3 U_o}{\partial y^2 \partial t_1}\right] \tag{3.39}$$

Equation (3.38) permits numerical solution for $\partial\zeta/\partial x_1$ and $\partial\zeta/\partial t_1$ when the x_1 and t_1 derivatives of k_o and ω_o entering the right side are known. The latter are determined from the solvability condition for Eq. (3.38) which requires that the right side terms be orthogonal to ζ^*.

This condition can be expressed as

$$I_1 + I_2 \frac{\partial k_o}{\partial x_1} + I_3 \frac{\partial \omega_o}{\partial x_1} = 0$$

$$I_4 + I_2 \frac{\partial k_o}{\partial t_1} + I_3 \frac{\partial \omega_o}{\partial t_1} = 0 \tag{3.40}$$

where

$$I_1 = \int_o^\infty h_1 \zeta^* dy = -iRek_o \int_o^\infty (k_o{}^2 \zeta\zeta^* + \zeta \frac{\partial^2 \zeta^*}{\partial y^2} + 2 \frac{\partial \zeta}{\partial y} \frac{\partial \zeta^*}{\partial y}) \frac{\partial U_o}{\partial x_1} dy$$

$$I_2 = \int_o^\infty h_2 \zeta^* dy \qquad\qquad I_3 = \int_o^\infty h_3 \zeta^* dy$$

$$I_4 = \int_o^\infty h_4 \zeta^* dy = -iRek_o \int_o^\infty (k_o{}^2 \zeta\zeta^* + \zeta \frac{\partial^2 \zeta^*}{\partial y^2} + 2 \frac{\partial \zeta}{\partial y} \frac{\partial \zeta^*}{\partial y}) \frac{\partial U_o}{\partial t_1} dy \tag{3.41}$$

From Eq. (3.28) for v_g and Eq. (3.40), v_g is obtained explicitly as

$$v_g = - \frac{I_4}{I_1} \tag{3.42}$$

and the derivatives of ω_o and k_o as

$$\frac{\partial \omega_o}{\partial x_1} = - \frac{I_1 v_g}{I_2 + I_3 v_g} \qquad \frac{\partial k_o}{\partial x_1} = - \frac{I_1}{I_2 + I_3 v_g}$$

$$\frac{\partial \omega_o}{\partial t_1} = - \frac{I_4 v_g}{I_2 + I_3 v_g} \qquad \frac{\partial k_o}{\partial t_1} = - \frac{I_4}{I_2 + I_3 v_g} \tag{3.43}$$

All of the basic relations necessary to apply the analysis have now been obtained.

Numerical Application of the Analysis

The numerical application of the foregoing perturbation analysis to a specific unsteady boundary layer flow is clearly a rather formidable task which, as mentioned previously, was beyond the scope of the present study. However, it is of interest to note briefly the procedural steps involved in the application to calculation of a neutral stability curve.

In general, both ω_1 and k_1 may be nonzero complex quantities whose imaginary parts will therefore contribute to the amplification or decay of disturbances in time and space. Extending the approach of Ref. 28 for steady boundary layer flows, the condition for neutral stability may be taken to be $\omega_{oi} + \varepsilon\omega_{1i} = k_{oi} + \varepsilon k_{1i} = 0$, where subscript i denotes the imaginary part of the complex quantity $\omega_{oR} + i\omega_{oi}$, etc. With this definition of neutral stability, the overall calculation could proceed *interatively as follows:*

1. For given values of x_1, t_1, Re determine the eigenvalues k_o and ω_o for which $k_{oi} = \omega_{oi} = 0$. This entails solution of $L(\zeta) = 0$ (Eq. 3.22 with $\phi_o = \zeta$) which is effectively the quasi-parallel, quasi-steady problem as calculated in Sec. 3.2 for the expansion-wave boundary layer.
2. For the given x_1, t_1, Re, and the eigenvalues ω_o and k_o obtained in step 1 determine k_1 and ω_1 (Eq. 3.37).
3. Using k_1 and ω_1 from step 2, recalculate step 1 to obtain new k_o and ω_o values for which $k_{oi} = -\varepsilon k_{1i}$ and $\omega_{oi} = -\varepsilon\omega_{1i}$.
4. Repeat step 2 etc. until satisfactory convergence is obtained.

4. EXPERIMENTAL PROGRAM ON TRANSITION TIMES

4.1 Scope of Experimental Study

As mentioned in the introduction, the experimental investigation was primarily concerned with the detection of laminar to turbulent boundary layer transition for the expansion wave flow, but some experiments were performed for the detection of shock wave boundary layer transition. The basic apparatus used to generate these flows is an expansion wave tube sealed by a diaphragm which ruptures under an initial pressure difference. For generation of the expansion waves, the tube is initially pressurized above atmospheric or room pressure, and the tube flow discharges directly to the room. For the generation of shock waves, the tube is partially evacuated to a pressure level below room pressure and the apparatus functions like a shock tube of infinite area ratio with a driver pressure of one atmosphere. Although the tube was initially designed for boundary layer studies, it became necessary in the course of the investigation to substantially redesign some portions as described in Sec. 4.2. In all experiments, piezoelectric pressure transducers were used to measure local static pressure histories; these are described briefly in Sec. 4.3.

Three methods were used to detect boundary layer transition: a flush hot-film surface anemometer, a thin film surface temperature thermometer, and a hot-wire anemometer. A few experiments were performed using the flush hot-film enamometer at a low constant current so that it responded to surface temperature. The devices used to detect boundary layer transition are described in Sec. 4.4. For the expansion wave, most of the transition

time data was obtained at distances of 2.17, 4.7 and 8.17 feet from the diaphragm location. The pressure transducers were located within 2 inches of the above distances, either at 2.0, 4.53 or 8.0 feet from the diaphragm. The initial pressure level in the expansion tube was varied from 35 to 145 psia in order to assess the effect of density. The test gas used was commercially bottled dry air. For the shock wave experiments, transition times were measured at 7.63 feet from the diaphragm location and at initial pressures of 1 psia to 7 psia. The preceding range of experimental conditions was effectively determined by the limitations of the apparatus. Figure 9 shows a schematic of the expansion-tube and shock tube configurations.

The flow times involved were typically of the order of a few milliseconds. All signal outputs were displayed on a Tektronix Dual Beam-Type 555-Oscilloscope and photographed. The oscilloscope sweep was triggered by the breaking of an aluminum foil due to the diaphragm rupture. The outputs from the anemometers and the charge amplifiers were simultaneously displayed on the lower beam by using a Tektronix 1A-4 plug-in unit. The output from the thin film thermometer required a much higher gain and was displayed independently on the upper beam using a Tektronix 1A-7 differential amplifier. The oscilloscope sweep calibration was checked using a Hewlett-Packard signal generator.

4.2 The Expansion Wave Tube

The expansion wave tube used consists primarily of a steel tube with rectangular interior cross-section of 1-1/2 x 5 inches. The total length of the tube is 15-1/2 feet made up of four interchangeable sections of 6, 4 and 4 feet and one section of 19 inches. The largest three sections are milled out of solid stock and in the form of a channel covered by a top

plate. The 19-inch section is made up of two aluminum blocks clamped between two steel plates. The channel and the top plates are held together tightly by socket head cap screws at 3 inch intervals.

Instrumentation ports of 2-inch diameter are provided in each section at 1-foot intervals for the 6-foot section, at 3-inch intervals in one of the 4-foot sections, and at 1 foot from one end of the 19-inch section. The 4-foot test section made especially for the present experiments is composed of a channel which has a 2-inch diameter port located 5-1/2 inches from one end, mainly used for hot wire instrumentation. The test channel is covered by a steel plate which has an instrumentation port located 4-1/2 inches from the end, used for static pressure measurements. The test plate also has two small ports at 6-1/2 inches from the end, designed to accommodate the flush hot-film anemometer to very close tolerances. The flush hot-film anemometer ports are at the same location as the hot-wire anemometer on the opposite wall. The centerline of all but one of the instrumentation ports coincide with the centerline of the 5-inch side wall. One of the flush hot-film anemometer ports is located 1.75 inches above the centerline (.75 inches from corner) to observe the effect of the corner flow on transition. Figure 9 shows the test section configurations.

The 5-inch side wall is 5/8 inches thick so that the maximum wall deflection for the highest pressure used (145 psia) was less than .002 inches. The expansion tube is designed especially for boundary layer studies so that the interior surface finish is of high quality. All steel parts of the tube were plated by Kanigen* Electrodeless Nickel to prevent rust. The finish of the mirror-like interior surface is such that the surface roughness

---

*Trade name for 92% pure Nickel and 8% Nickel Phosphide.

is less than 20μ inches. The only significant protrusions affecting the boundary layer are those due to the small steps made by the flush hot-film anemometer probe. For the special test section used, the protrusions due to the flush hot-film and the hot-wire instrumentation plug are less than .0005 inch; the hot-wire instrumentation plug was specially ground and plated while positioned in the channel.

An air line at the tube end connects through tubing to the air supply, the vacuum pump, and the pressure gauges. For initial pressure levels above atmospheric, Heise Bourdon gauges are used to measure initial tube pressure. Pressure levels below atmospheric were measured using a Wallace and Tiernan precision vacuum gauge which was calibrated against a U-tube manometer and a precision barometer (at room pressure). The initial tube temperature was obtained from the average reading of two precision thermometers which are in good thermal contact with the tube and accurate to .1°C.

The expansion waves are formed by rapid rupture of a mylar diaphragm. The diaphragm is clamped to seal the tube end using clamping plates of different opening areas. The mylar diaphragms used were either 1, 3, 5 or 7 thousandth inch in thickness. The clamping plate and the mylar thickness are chosen such that the mylar withstands the initial pressured used and ruptures rapidly when subjected to electrical heating from a wire taped to the diaphragm. The wave form of the shock wave is generated by puncturing a 1 thousands inch mylar diaphragm.

One external factor present in all shock-tube type studies of wall boundary layer transition is transient vibration of the tube walls due to the transient loading imposed (following the diaphragm burst) by the formation and propagation of the wave, whether shock or expansion wave. In addition to any direct effects of the wall motion on boundary layer stability (e.g., due to the changed wall velocity boundary conditions) the

wall motion will also generate an acoustic or pressure disturbance field whose components will have wavelengths dependent on the spectrum of wall frequencies as well as on the gas sound speed. No previous investigations appear to have been made of the possible influence of such wall vibration on the boundary-layer transition times observed in wave induced flows. A study of the wall vibration effects on transition was beyond the scope of the present work. However, some brief comments on the question are in order.

The wall mounted pressure transducers used in the present study (Sec. 4.3) showed effects of tube wall vibration at the highest initial tube pressure. This is illustrated by the pressure-time records of Fig. 58 for an initial tube pressure level of 125 psia and for several distances from the diaphragm location. The fluctuations in pressure start before the expansion wavehead arrival and continue to be superimposed on the pressure record after wave arrival. The observed lowest frequency of the oscillations is roughly 2500 Hz and the amplitude approximately .5 psi. The actual wall response to the travelling load is transient and is a complex superposition of the eigen modes of vibration. An estimate of the lowest natural frequency of vibration was made for clamped wall edges and simply supported wall edges giving 3700 Hz and 1660 Hz respectively. The tube wall edges are actually neither clamped nor simply supported, so that the observed frequency of oscillation (2500 Hz) is in between these estimates. Figure 59 shows a simultaneous record of wall acceleration versus time obtained with a Kistler 808 quartz accelerometer mounted at the midpoint of the 5-inch sidewall. The high frequency components are very evident in the acceleration. The maximum acceleration for the conditions shown is of the order of 1 g (i.e., 32 ft/sec^2).

4.3 Static Pressure Measurements

The local static pressure at the wall is measured using 603A Kistler piezoelectric pressure transducers which are mounted flush in the center of 2-inch instrumentation plugs. The transducers are embedded in a phenolic laminated core to minimize transmission of mechanical shock. The sensing diaphragm of the transducer is less than 0.2 inches in diameter, so that the spatial resolution was more than adequate for the expansion wave forms. The high impedence output of the transducers is connected by special low noise cables to Kistler 505-A charge amplifiers. The transducers and connectors were cleaned frequently using Freon solvent to maintain the high impedence and minimize charge leakage. The dynamic calibration of the transducers was obtained using the flow behind a shock wave and agree within ±5% of the calibration supplied by the manufacturer.

4.4 Instrumentation for Detection of Boundary Layer Transition

Three techniques were used to detect boundary layer transition: a flush hot-film anemometer, a hot-wire anemometer, and a thin-film surface temperature thermometer. The experimental data is interpreted in Secs. 5.2-5.4.

Flush Hot-Film Anemometer

A DISA 55A90 flush mounting anemometer probe was utilized as the primary instrument to detect boundary layer transition. The probe is composed of a quartz rod on which a nickel film is sputtered on the .187 inch diameter plane end. A thin protective quartz coating is applied to the sensor. The film is .2mm long and 1mm wide and the quartz coating is approximately .5μm thick. The film has a film resistance of approximately

15Ω at room conditions and a temperature coefficient of resistance of .25% per °C. A picture of the probe is shown in Fig. 13.

The probe was mounted in a 2-inch diameter aluminum instrumentation plug as well as being directly placed in the small ports of the special test section. The probes were installed such that they were recessed or protruded by less than .0005 inches from the surface. This was accomplished by use of brass shims which varied in thickness from .0005 to .005 inches. Proper alignment of the film so that the 1mm width was closely perpendicular to the flow direction was achieved visually prior to channel and cover plate assembly.

The probes were connected by a special probe connector and a shielded 5 meter cable to a DISA 55D01 anemometer. The anemometer maintains the probe resistance and thus the temperature at some constant value determined by the decade resistance setting on the anemometer. Standard constant temperature anemometer procedures were used as outlined in the Disa 55D01 manual to obtain the best results. A square wave was used to adjust for cable length and capacitance yielding a frequency response greater than 10 KHz, as illustrated by Fig. 12. Typical overheat ratios used were .2, .3, .5 and .6 corresponding to temperatures above ambient of 80°C, 120°C, 200°C and 240°C, respectively. The interpretation of the flush hot-film results are discussed in Sec. 5.2.

Hot-Wire Anemometer

Three types of hot-wire probes supplied by Thermo Systems, Inc., were used in this investigation; a straight probe, a right angle probe and an 86.5° probe. The last two probes are particularly useful for measurements close to the wall. The straight probe was only used for observing inviscid

flow properties. All probe angles referred to are measured between the wire supports and the probe stem which protrudes from the side wall. Figure 15a is a schematic showing an 86.5° probe mounted in the side wall. The hot wire is mounted in a 2-inch diameter steel plug which was ground and plated while installed in the channel and is thus perfectly flush with the channel surface. The probe stem hole is located at the edge of the instrumentation plug, so that right angle or similar type probes can be turned in a way that the plug edge does not interfere with the observed boundary layer flow and so that the probe is at the same location as the flush hot-film on the opposite wall. A photograph of this installed probe is shown in Fig. 15b.

The hot wire probe is secured in a 40 threads to the inch screw which varies its location from the wall. A disc attached to the probe body indicates the alignment of the hot wire with respect to the flow direction and is used to rotate the probe while maintaining the same distance away from the wall. The hot wire location from the wall is determined for right angle type probes by bringing the wire within a few wire diameters of the plug surface. At that point, the mirror image appears on the highly polished surface and is observed under a microscope. The distance between the wire and its image is compared with some reference length, such as the wire diameter or some known shim stock thickness, which is at the same approximate location under the microscope. Half of this distance is then used as the reference point for locating the wire. The hot-wire orientation with respect to the flow direction is determined by aligning the screw attached to the disc so that it points in the same direction as the wire supports. The disk is secured to the probe stem and rotates with it. The above mentioned visual alignment is estimated to be within 5° accuracy. The probes were connected by an adapter and a shielded 5 meter cable to

a Disa 55D01 anemomter unit and a procedure similar to that of the previous section was used for measuring the hot wire output.

Using incompressible potential flow theory, King [57] considered the heat loss from small diameter cylinders of infinite length placed normal to a stream of fluid and developed the following relation:

$$I^2R_w = (A\sqrt{u} + B)(T_w - T_s) \tag{4.1}$$

where $B = K\ell$, $A = \ell\sqrt{2\pi KC_p\rho d}$, T_s is the stagnation temperature for an unheated wire, T_w is the wire temperature, ℓ the wire length and d the diameter. Experimental studies with hot wires have shown that King's law is not exact but that experimental evaluation of the constants A and B yield good results. A and B can be treated as constants only as long as no large change in temperature or density occurs. For compressible flows, it thus becomes necessary to re-write King's law in the following form (Ref. 46).

$$I^2R_w = (A\sqrt{\rho u} + B)(T_w - T_s) \tag{4.2}$$

The interpretation of the hot-wire data is presented in Sec. 5.3.

Thin Film Resistance Thermometer

The initial studies made in the present apparatus on boundary layer transition utilized a thin gold film resistance thermometer evaporated onto a pyrex disk which was flush mounted at the surface. The film had a width of 2mm, a length of 1-1/2 inches and a thickness of about 150 Å. The response time of this film is less than 10^{-5} seconds so that it responds to the instantaneous temperature at the surface on which it is mounted.

The thin film is used as a resistance thermometer of nominal resistance $R_o \approx 500$ ohms in series with a much larger resistance $R_B = 12{,}000\Omega$ in a constant voltage circuit. The almost constant current is kept to a minimum to reduce the effect of electrical heating and is typically less than 5 milli-amps. Small changes in surface temperature are proportional to the change in film voltage ΔE and are given by:

$$\Delta T_w(t) = \frac{C\Delta E(t)}{E_f \alpha_T} \tag{4.3}$$

where E_f is the initial film voltage, α_T is the temperature coefficient of resistance of the thin film, and $C = (1 + R_o/R_B)$ is a correction factor which compensates for the slight change in current due to resistance change. Figure 16 shows a photograph of the film and Fig. 17 a schematic of the circuit used. A Hewlett Packard HP 6207B power supply was used as the constant voltage source. The film resistance thermometer used was developed as part of a previous study and a more detailed description of its construction and operation is given by Srinivasan [5].

The flush constant-current anemometer data was obtained by using the Disa 55A90 flush mounted anemometer probe at a constant low current level. The probe thus responds to the surface temperature in a manner which is very similar to the thin film resistance thermometer. Results for the thin-film resistance thermometer and the flush constant-current anemometer are discussed in Sec. 5.4 and comparisons with flush hot-film, hot-wire, and flush constant current anemometer data made.

5.0 EXPERIMENTAL RESULTS FOR TRANSITION

As previously mentioned, the main concern of the experiments was the determination of transition times for the expansion-wave wall boundary layer for which very little previous data exists A series of experiments with shock-wave induced wall boundary layers was also carried out in order to make comparisons with the very extensive amount of shock-wave transition data reported by previous investigators. The transition Reynolds numbers for the shock-wave boundary layer (presented in Sec. 5.6) exceeded those of previous investigators, which indicated the surface of the expansion-tube to be extremely smooth.

The responses of the pressure transducer and transition detection instruments for the expansion wave boundary layer are discussed in Secs. 5.1-5.4. The transition times for the shock-wave boundary layer and the expansion-wave boundary layer are discussed in Secs. 5.5 and 5.6, respectively.

5.1 Static Pressure

The local pressure-time record was used to find the origin of the x-t coordinate system, to determine the inviscid flow quantities, and to confirm that the waveform and inviscid flow were free from extraneous disturbances. At the 8.17 foot location the pressure record also indicated the arrival of the reflected wave. For the shock wave experiments, two pressure transducers placed a known distance apart were used to measure the speed of the shock wave. The local static pressure was recorded for all experiments. Typical pressure-time traces for the expansion wave are shown in Figs. 18-31. The arrival of the expansion wave head at the pressure transducer is indicated by a sudden change in the slope of the pressure-time

record. The expansion-wave head arrives at the hot-wire locations and the flush hot-film locations approximately $.15 \times 10^{-3}$ seconds later.

As mentioned in Sec. 2.1, the expansion wave is assumed to be plane and isentropic with the family of mathematical characteristics I being straight lines in the x-t plane as in Figs. 1a and 1b. Ideally, the first derivatives of the inviscid flow quantities for non-zero initial acceleration are discontinuous at the wave head. This was indeed the case in the experiments except for a few cases of poor diaphragm rupture.

The partial derivatives of the inviscid flow quantities at the wave head determine the origin of the x-t coordinate system of Figs. 1a and 1b. As described in Sec. 2.1, the slope of the pressure-time record at the time of wave head arrival can be used to find the origin from the following expression:

$$X_o = \frac{\gamma \beta P_o a_o}{\left(\frac{\partial P_e}{\partial t}\right)_H}$$

The origin is uniquely determined for each experiment; $t_o = -X_o/a_o$ is the time that the wave head of an expansion wave originating at $X = 0$ takes to arrive at $X = X_o$.

For a centered expansion wave, the similarity parameter s_o and thus all other inviscid quantities can be determined once t_o is known. $s_o = \tau/(t_o + \tau)$ where τ is the time elapsed following the time of wave head arrival at a location $X = X_o$. At locations close to the diaphragm, the wave forms generated are non-centered and the inviscid flow quantities must be determined from the similarity parameter s of Eq. (2.6), i.e., $s = s_o + e/a_o t$. e is the x displacement of fluid particles having velocity u_e from their respective centered wave position, as shown in Fig. 1b. s can be determined from the pressure time record using the relation

$$\frac{P_e}{P_o} = (1-\bar{\varepsilon}s)^{\gamma\beta/\bar{\varepsilon}}.$$

The wave form as observed at 2.17 feet from the diaphragm location is non-centered while those observed at 4.7 and 8.17 feet are closer to being centered. Table IV shows a comparison of the similarity parameters s and s_o at the observed times of boundary layer transitions. Values of s larger than s_o indicate the presence of non-centered wave effects. Some values of s are substantially smaller than s_o indicating that the pressure had essentially ceased to drop prior to the observed transition, i.e., that transition occurred in a region of essentially steady outer inviscid flow. The laminar boundary layer of the constant inviscid flow region is still unsteady, but its stability is no longer influenced by a favorable pressure gradient. In this region there is still heat being added to the flow at the wall. This has a destabilizing effect on stability and transition in that it promotes the occurrence of a point of inflection in the velocity profile (Tollmien [24]).

Most experiments were performed with the expansion tube end fully open in order to observe transition within the wave and before the constant flow property region. Due to the large transition times observed, this was not always possible, as shown in Fig. 18, especially for low initial tube pressure levels and stations close to the diaphragm. The lowest pressure behind the expansion wave is determined by the chocking conditions at the open end due to the boundary layer displacement effect and any obstruction due to the ruptured diaphragm. For low tube pressure levels (<45 psia) the flow at the open tube end is often unchocked and the wave tail as determined by the time-pressure record is not well defined.

5.2 Flush Hot-Film Anemometer Results

The primary instrument used to detect boundary layer transition was the flush hot-film anemometer. This instrument was found to be the most sensitive of the instruments used for this task. Theoretical analysis of its response indicated that it should response to the local surface shear stress in an essentially quasi-steady fashion. This was born out by a series of calibration experiments. The theoretical analysis of the flush hot-film response as presented in Appendix B shows the shear stress to be approximately proportional to the probe current to the third power. The probe temperature and its resistance are maintained at a set initial level by the Disa 55D01 anemometer unit.

Expansion Wave Results

For the high transition Reynolds numbers and accelerating pressure gradient involved, transition occurs abruptly as shown in the expansion wave records of Figs. 18-37. Figures 18 and 19 show typical response of the flush hot-film anemometer (FHFA) to transition. Signals labelled a are the static pressure versus time records, while b and c are the simultaneous hot-film outputs respectively placed 1.75 inches off the centerline of the 5-inch side wall (labelled FHFA at corner) and on the centerline of the 5-inch side wall. At transition shear stress at the wall increases. This is demonstrated by the sudden increase in heat transfer from the probe and the accompanying increase in probe current level required to maintain the probe at the desired temperature level. The anemometer output almost doubles, indicating that the skin friction increases by a factor of 6 to 8 over its laminar value.

Early experiments with the flush hot-film to detect expansion-wave boundary layer transition times were made by mounting the probe in a 2-inch diameter aluminum instrumentation plug. The aluminum plug was in turn inserted at the center of the 5-inch side wall so that it was essentially flush with the steel surface to within .001 inches. For some of these records, such as those shown in Figs. 32-34, it was observed that after approximately 1.5×10^{-3} seconds, the anemometer output suddenly increased for a time period, then dropped for some further time period, and finally increased again. The flow associated with the intermediate time interval characterized by a high anemometer output is herein termed a turbulent slug. It is interpreted as follows. Initially the expansion-wave boundary layer thickness is very small at the time of wave head arrival. The protrusion by the edge of the plug can trip the boundary layer (Dryden [47]) for some initial period even though the Reynolds number is substantially below the critical value determined from stability theory. If the Reynolds number remains below the critical Reynolds number and the boundary layer becomes sufficiently thick compared to the protrusion height then the boundary layer may re-laminarize. The sequence of records of Figs. 32-34 show that the turbulent slug almost disappears below a certain pressure level and that for increasing pressure levels the duration of the slug gets longer until finally it merges with what might be termed the untripped turbulent boundary layer.

In later attempting to repeat some of the results of Figs. 32-34, it became apparent that the situation was very sensitive to the degree to which the plug was tightened in the tube wall. The step size as measured using a micrometer was less than .0005 inches and could have easily been altered by tightening or loosening the bolts securing the plug. Shimming

the plug permitted the observation of longer transition times. Ultimately the anemometer probes were mounted directly in the tube wall as previously described, which eliminated the turbulent slug and gave the longest transition times. Occasionally, the aluminum plug was fortuitously mounted in the side wall so that the turbulent slug was not observed over a large range of pressures. Figures 35-38 show results for such a case where the aluminum plug was mounted in the channel wall and a second hot-film probe was inserted at the center of the opposite side wall (plate side). The simultaneously observed transition times are in good agreement, especially at the lower pressure levels (Figs. 35, 36). For initial tube pressure levels larger than 85 psia, the probe mounted in the aluminum plug indicated transition times which were increasingly smaller than those indicated by the probe mounted directly into the wall.

Shock-Wave Results

Figure 14 shows a schematic of the thermal boundary layer developed over the flush hot-film anemometer. Note that the momentum boundary layer is developed over a much larger length than the length of the hot-film and is therefore much larger than the thermal boundary layer thickness. For the expansion-wave the gas temperature is lower than the wall temperature and the temperature at the edge of the thermal boundary layer developed over the flush hot-film is slightly lower than the surrounding wall temperature. For the shock-wave boundary layer flows, the gas temperature is substantially higher than the wall temperature and the temperature at the edge of the thermal boundary layer is larger than that of the surrounding wall. For sufficiently strong shock waves the temperature at the edge of the thermal boundary layer can be large enough so that

upon transition the hot-film anemometer output drops rather than rises.

For the weak shock wave experiments of Figs. 39-42, there is a sudden increase in the hot-film anemometer output at the time of shock-wave arrival followed by a second increase which is interpreted as boundary layer transition. For the weakest shocks of Figs. 39-41 an overheat ratio a = .2 (film temperature ≈ 100°C) was used. The shock wave of Fig. 41 is stronger than those of Figs. 39 and 40 so that the sudden increase in anemometer output is difficult to detect. An increase or decrease in the film overheat ratio would result in a more clear indication of transition. For the stronger shock of Fig. 42 an overheat ratio a = .3 (film temperature ≈ 140°C) was used in order to observe a rise in anemometer output at transition.

Expansion-wave and shock-wave boundary layer transition times and their interpretations are discussed in Secs. 5.6 and 5.5 respectively.

5.3 Hot-Wire Results

In the present study, the hot-wire was used to confirm the transition times for the expansion wave boundary layer interpreted from the flush hot-film results. Figures 43-47 show simultaneous records of the response of the hot-wire anemometer located at distances of .035 and .02 inches from the wall, and the response of the flush hot-film anemometer at the same X location on the opposite wall. As seen in Fig. 44, the hot-wire response (labeled b) abruptly declines at about the same time that the flush hot-film response (labeled c) abruptly increases. The sudden drop in hot-wire anemometer output is interpreted as an indication of transition. Agreement of interpreted transition times from the hot-wire and the flush hot-film was considered to be very good, especially since

the two probes are on opposite walls.

The sudden decline in hot-wire output is believed to be due to the boundary layer suddenly becoming thicker at transition. The wire, which is initially close to the edge of the laminar boundary layer, is suddenly engulfed by a slower moving gas, and thus a drop in anemometer output results. The use of the hot-wire for measurements in the boundary layer is difficult since the boundary layer is typically less than .05 inches in thickness and is changing in thickness from a zero initial value. The physical properties also change across the boundary layer when compressibility effects are significant.

5.4 Thin-Film Resistance Thermometer Results

Some experiments were performed in order to make a direct comparison of expansion-wave transition times interpreted from the flush hot-film anemometer and a thin-film resistance thermometer. The flush hot-film probe was mounted directly in the cover plate of the modified test section while the thin-film resistance thermometer plug was installed almost directly opposite in the channel wall. Figures 50-52 show typical results. Figure 51 shows a linear drop in film-voltage (labeled c) for about the initial millisecond after wave heat arrival. This is followed by a slightly steeper linear drop in film output for about three milliseconds and finally a sharp decrease in slope and some fluctuations in the film output. This last change in slope could be interpreted as being due to a natural boundary layer transition but, in fact, is believed to be due to tripping by the edge of the instrumentation plug. Note that the flush hot film on the opposite wall indicated a transition time which is more than double the 4.4 milliseconds indicated by the thin-film resistance thermometer.

Figure 50 shows similar results to those of Fig. 51 except that at the lower pressure of 45 psi the thin-film thermometer indicates a rise in film temperature after twelve milliseconds which could be interpreted as the end of the turbulent slug (Sec. 5.2). The rise in thin film thermometer voltage output peaks and drops again at about the same time that the flush hot-film indicates transition. These records (Figs. 50-52) show how the thin-film resistance thermometer output could be mis-interpreted to give a transition time which is smaller than that which would occur for an untripped boundary layer. It is possible that the small expansion-wave boundary layer transition times observed by Chabai [1] using a thin film resistance thermometer might have been due to boundary layer tripping.

Flush Constant-Current Anemometer Results

Operated cold and at a low constant current level the same probe used as a flush hot film can be operated to measure the wall surface temperature. For this purpose the constant-current anemometer was inserted in an aluminum instrumentation plug which was inserted in the center of the channel wall and at 4.6 feet from the diaphragm location. Most of the flush hot-film data was obtained on the opposite wall at 4.7 feet from the diaphragm location.

Figures 53-55 show the flush constant-current anemometer output (labeled b) for the expansion-wave boundary layer. The current level used in 3.35 milli-amps and the film voltage change is amplified about 2300 times by the Disa 55D01 anemometer. The abrupt change in the slope of the anemometer output (as in Fig. 53, 14 milliseconds after wave head arrival), is interpreted as boundary layer transition. The indicated transition times (Figs. 53-55) are in good agreement with transition times indicated by the flush hot-film results on the opposite wall (Sec. 5.6).

5.5 Transition Times for the Shock-Wave Boundary Layer

As previously mentioned, the purpose of the shock-wave boundary layer experiments was to make comparisons with the extensive shock-wave transition data reported by previous investigators [1,3,4,6]. A summary of the shock-wave boundary layer transition times measured in the present study for shock wave Mach numbers M_s of 1.17 to 1.81 are presented in Table V. X_p is the particle path length based on the observed transition time τ and the inviscid flow velocity. Particle path lengths larger than 3.5 feet are beyond the joining of the special 4-foot section with the contiguous section. For these particle paths, the possibility exists that any step due to the joining could have tripped the boundary layer (example: M_s = 1.79 and 1.81). Transition Reynolds numbers based on particle path length at transition seem to correlate well with a value $Re_{X_p} \approx (4.0 \pm 1) \times 10^6$. Also shown in Table V is the transition Reynolds number $Re_{X_{TR}}$ based on distance X_{TR} from the shock-wave front at which transition occurs. Figure 56 shows the present shock-wave transition data ($Re_{X_{TR}}$) and that of previous authors shown as a function of wall-to-free stream temperature ratio (T_w/T_e). The kinematic viscosity of the inviscid flow, $\nu_e = \mu_e/\rho_e$, is used in all Reynolds number calculations. Note that $Re_{X_{TR}}$ decreases with increasing T_w/T_e (weaker shocks) which is opposite to the trend suggested by Ostrachs stability calculations. It is worth noting from the results of Table V that transition Reynolds numbers based on the particle path length are better suited for the prediction of transition.

The curve of Ostrach and Thornton [7] shown in Fig. 56 is the critical stability Reynolds number calculated by them from linear stability theory for the compressible shock-wave induced boundary layer using the approximate method of Lees [36]. The most striking feature here is that

most of the experimental transition Reynolds numbers are very much less than the critical Reynolds number $Re_{x_{cr}}$ calculated from linear stability theory. As pointed out by Ostrach and Thornton, this probably indicates the presence of dominant effects or factors influencing transition other than the internal Tollmien-Schlichting disturbances of the stability analysis. The shock-wave data of the present study agree fairly closely with those of Thompson which generally lie the closest to the critical stability curve. The present data actually slightly exceed the critical stability Reynolds number for the weakest shock waves studied. The results of the present shock-wave transition experiments were gratifying in that they verified modifications made to the present apparatus (e.g., elimination of very small surface discontinuities, as previously described) and provided some confidence that the expansion-wave boundary-layer transition experiments should be as free as reasonably possible from dominant gross effects of surface discontinuities or irregularities. In this respect, it might be noted that transition of the shock-wave induced boundary layer is very sensitive to small surface discontinuities or isolated roughness elements (Chabai [1]).

5.6 Transition Times for the Expansion-Wave Boundary Layer

For the expansion-wave boundary layer transition times were observed at the center of the 5-inch wall as well as 1.75 inches off the center to observe corner effects on transition times. As discussed in Secs. 5.3 and 5.4, most transition times indicated by other instruments agreed very well with those times indicated by the flush hot-film results. Only transition time data from the flush hot-film is therefore analyzed in this section. For the flush hot-film probes at the center and corner, experimental

transition times (after wave head arrival) are summarized in Table III. Quantities expressed as a ratio indicate the presence of a turbulent slug where the small time indicates the beginning of the slug and the large time the final indication of transition. For low initial tube pressure levels, where the turbulent slug was not observed, transition times detected by both probes were in good agreement. The turbulent slug phenomenon was only observed for the corner probe. The reason for this is not known, but it might be pointed out that the 1.5 inch top wall was rougher than the 5-inch side wall.

The particle path length for most of the observed transition times are less than the maximum of 3.5 feet of "clean" length necessary to avoid tripping of the boundary layer by the joint with the contiguous tube section. At 4.6 feet from the diaphragm location, observed center probe transition times for initial pressures of 55 psia or less are almost constant, possibly due to the particle path lengths being larger than 3.5 feet. For the 8.17 foot location from the diaphragm, center probe transition times for initial pressure levels lower than 92 psia occur in the reflected wave region where the gas is de-accelerated. Some of the observed transition times in the reflected wave region occur as much as 5 milliseconds after the arrival of the reflected wave.

The flush hot film located at the center of the 5-inch wall indicated the longest transition times. As expected, the transition times increased with distance from the diaphragm location and decreased with increasing pressure. At the higher pressures, there appears to be an abrupt change in the transition time with increasing pressure, possibly because of the increasing importance of wall roughness. The transition times observed are in general four times greater than those observed previously by

Chabai [1].

As mentioned in Sec. 5.1, some of the observed expansion-wave transition times occurred under the influence of a non-centered expansion wave or in a constant flow region. Table IV summarizes the values of the centered (s_o) and non-centered (s) similarity parameters at which transition is indicated by the center-line flush hot film. Values of s_o smaller than s indicate that non-centered wave effects are present, while values of s_o substantially larger than s indicate that the observed transition occurred in the constant flow region behind the wave. In the constant flow region, the stabilizing favorable pressure gradient is no longer present, and the boundary layer is under the destabilizing effect of the wall heating (Tollmien [24]).

Figure 57 illustrates the present expansion-wave transition data in terms of the local Reynolds number at transition, $Re_{\delta^*_{TR}}$, based on the local displacement thickness δ^* (tube fixed coordinates) versus the local streamwise similarity coordinate s. The curve in Fig. 57 is the critical stability Reynolds number, $Re_{\delta^*_{cr}}$, calculated by the approximate method of Lees [36] as previously discussed. As in the case of the shock-wave results (Sec. 5.4) the trend of the experimental data do not follow the critical stability curve. However, the magnitudes of the experimental transition Reynolds numbers are generally much closer to the theoretical critical stability values than in the case of the shock-wave boundary layer discussed in Sec. 5.5. The observed transition Reynolds number, $Re_{\delta^*_{TR}}$, varies between 4.5 and 10^3 to 7.5×10^3, and is either slightly above or below the predicted critical value. All Reynolds numbers are evaluated using the kinematic viscosity ν_e of the inviscid flow.

6.0 SUMMARY AND CONCLUSIONS

The chief interest of the present study has been the stability and transition characteristics of the unsteady laminar wall boundary layer developed within plane expansion waves travelling into gas at rest. Such previous studies of wave induced boundary layers have mainly concerned the case of the shock wave where the boundary layer is inherently steady (in wave fixed coordinates) and the inviscid outer flow is uniform or constant in space. In contrast, the expansion wave boundary layer is inherently unsteady, and the inviscid flow is characterized by strong spatial gradients. This type of unsteady wave induced flow is of interest in various unsteady flow devices and also closely simulates the unsteady boundary layer development on an accelerating plate.

The linear stability of the expansion wave boundary layer has been investigated theoretically from several viewpoints in the present work. It has been shown that the stability behavior should be near quasi-steady over an appreciable range of conditions. On this basis, two approaches were used to evaluate the linear stability under the limiting assumptions of quasi-parallel and quasi-steady flow. The first approach used the approximate method of L. Lees to determine the minimum critical Reynolds number for the compressible expansion-wave boundary layer, with heat transfer, over a range of the streamwise similarity coordinate S from 0 to 1. Because of the accelerating pressure gradient, the critical Reynolds number is substantially greater than for the classical Blasius boundary layer and decreases from a maximum value at the wavehead (S = 0) as S increases.

The second approach used for the quasi-parallel, quasi-steady

assumption was exact numerical solution of the Orr-Sommerfeld equation governing the linear stability. This was done only for the limiting case of S = 0 (i.e., at the wavehead) where incompressible flow approximations apply. The neutral stability curve was calculated, and the minimum or critical Reynolds number so obtained agrees closely with the value obtained by Lees' approximate method for S = 0.

For such unsteady boundary layer flows in which the stability behavior is close to quasi-steady, a suitable perturbation of the limiting quasi-steady, quasi-parallel model should provide a first estimate of unsteadiness effects. Such a general perturbation method was developed using the method of multiple scales in which slow time and space coordinates were introduced to allow for both time and space variations of the mean flow. In general, the effects of the mean flow unsteadiness may be expected to be of the same order as effects due to spatial variations of the mean boundary layer flow, so that both the time and space variations of the mean flow must be considered together. Numerical application of the perturbation method is clearly a very considerable task and was beyond the scope of the present study. However, the first step of the application is the solution of the limiting quasi-steady, quasi-parallel model, which was done for the expansion wavehead boundary layer as previously mentioned. The perturbation method is applicable to any unsteady boundary layer whose linear stability behavior is close to quasi-steady. In particular, the method is applicable whenever the mean flow itself is close to quasi-steady.

In the present experimental study, boundary-layer transition times were measured for the laminar wall boundary layers induced by plane shock waves as well as expansion waves travelling into air at rest.

Three methods of detecting transition were used: a surface hot-film anemometer, a surface thin-film resistance thermometer, and a hot wire anemometer located in the boundary layer. Generally, the transition times determined by these different methods were in close agreement. However, the surface hot-film anemometer proved a particularly useful and sensitive indicator of transition in the expansion wave flows. It was shown that the hot film behavior was essentially quasi-steady and thereby responsive to the local skin friction which undergoes a very large and rapid increase on transition. The hot film revealed transition of the expansion wave boundary layer to be readily produced by tripping due to very small surface steps or proturbances, contrary to results reported by previous investigators. This effect is believed to be responsible for the turbulent slug phenomenon observed under some conditions. On the basis of the hot film indication of such effects, the test section used was modified to eliminate minute surface steps originally present.

Transition Reynolds numbers previously measured for shock wave boundary layers generally fall well below the critical stability Reynolds numbers predicted by linear stability theory. The present shock wave transition data agree fairly well with Thompson's data which generally lie closest to the critical stability curve. For the weakest shock waves studied, the present data slightly exceed the stability prediction. The relatively high transition Reynolds numbers observed in the present shock wave experiments were interpreted as indicating the test section surface to be very smooth and free from significant roughness elements.

The transition times measured in the present expansion wave experiments are some five to eight times larger than those reported from an earlier study by Chabai who used surface thin-film resistance

thermometers as the method of detection. As for the shock wave data, the expansion wave transition Reynolds numbers do not follow the trend of the theoretical critical stability curve. Likewise, most of the data lie below the stability curve.

The relatively low transition Reynolds numbers of the expansion wave boundary layer as compared to the critical stability Reynolds numbers predicted by the linear stability theory would suggest, as in the shock wave case, that transition was dominated by mechanisms or disturbances not accounted for in the linear stability theory used. One such disturbance present to some degree in all shock-tube type experiments is that of tube wall vibrations. Another disturbance of interest in this connection is that of secondary flows induced by the rectangular tube cross-section. It would be of interest to investigate such effects in future studies.

REFERENCES:

1. Chabai, A.J., "Measurement of wall heat transfer and of transition to turbulence during hot gas and rarefaction flows in a shock tube," PhD dissertation, Lehigh Univ., Institute of Research, Tech. Report 12, 1958.

2. Mirels, H., "Boundary layer behind a shock or thin expansion wave moving into a stationary fluid," NACA TN 3712, May 1956.

3. Hartunian, R.A., Russo, A.L., and Marrone, D.V., "Boundary-layer transition and heat transfer in shock tubes," Journal of the Aerospace Sciences, August 1960.

4. Thompson, W.P., and Emrich, R.J., "Turbulent Spots and Wall Roughness Effects in Shock Tube Boundary Layer Transition," Phys. Fluids V. 10, 17(1967). Also Thompson, W.P., Lehigh Univ. Institute of Research Tech. Rept. 16(1963).

5. Srinivasan, G., "Investigation of laminar wall boundary layers developed within non-centered unsteady waves," PhD dissertation, State Univ. of New York at Buffalo, Department of Mechanical Engineering, May 1974.

6. Smith, W.E., et al., "Schlieren studies of the flow field behind strong shocks," Meet. of Amer. Phys. Soc., Div. of Fluid Mech., Nov. 1954.

7. Ostrach, Simon and Thornton, P.R., "Stability of compressible boundary layers induced by a moving wave," Journal of the Aerospace Sciences, March 1962.

8. Hall, J.G., Srinivasan, G. and Rathi, J.S., "Influence of non-centered wave geometry on unsteady wall boundary layer development," in Recent Develop. in Shock Tube Research, Proc. of 9th Inter. Shock Tube Sym., Stanford Univ. Press, 1973, Ed. Daniel Bershader and Wayland Griffith, pp. 486-497.

9. Courant, R. and Friedrichs, K.O., Supersonic Flow and Shock Waves, Chap. III B, Intersci. Publishers, Inc., NY, 1948.

10. Cohen, N.B., "A power series solution for the unsteady laminar boundary layer flow in an expansion wave of finite width moving through a gas initially at rest," NACA TN 3943, 1957.

11. Trimpi, R.L. and Cohen, N.B., "An integral solution to the flat plate laminar boundary layer flow existing inside and after expansion waves and after shock waves moving into quiescent fluid with particular application to the complete shock tube flows," NACA TN 3944, 1957.

12. Lin, C.C., The Theory of Hydrodynamic Stability, Cambridge Univ. Press, 1966.

13. Schlichting, H. (1940), "Uber die theoretische Berechenung der Kritischen Reynoldsschen Zahl einer Reibungsschicht in beschleunigter und verzogerter Stromung," Jb. dtsch. Luftfahrft. 1, 97-112.

14. Pretsch, J., "Die Stabilitat einer ebenen Laminarstromung bei Druckgefalle und Druckansteig," Jb. dtsch. Luftfahrtf. 1, 158-175.

15. Hahnemann, E., Freeman, J.C. and Finston, M., "Stability of boundary layers and of flow in entrance section of channel," Journal of the Aerospace Sciences, 15, 493-496.

16. Wazzan, A.R., Okamura, T.T., and Smith, A.M.O., "Spatial and temporal stability charts for the Falkner-Skan boundary layer profiles," Douglas Aircraft Co., Report No. DAC-67086, 1968.

17. Narayan, M.A.B., "An experimental study of reverse transition in two dimensional channel flow," Journal of Fluid Mechanics, 31, 609-624, 1968.

18. Narayan, M.A.B., and Ramjee, V., "On the criteria for reverse transition in a two-dimensional boundary layer flow," Journal of Fluid Mechanics, 35, 225-241, 1969.

19. Liepmann, H.W., and Fila, G.H., "Investigation of effect of surface temperature and single roughness elements on boundary layer transition," NACA TN 1196, 1947, NACA Report 890, 1947.

20. Dryden, H.L., "Transition from laminar to turbulent flow at subsonic and supersonic speeds," Proc. of Conf. on High Speed Aero., Polytechnic Inst. of Brooklyn, Jan. 20-22, 1955.

21. Jaffe, N.A., Okamura, T.T., and Smith, A.M.O., "Determination of spatial amplification factors and their application to predicting transition," AIAA Jour., 8, No. 2, 1970.

22. Shen, S.F., "Some considerations on the laminar stability of time-dependent flows," Journal of the Aerospace Sciences, May 1961.

23. Conrad, P.W. and Criminale, W.O., Jr., "The stability of time-dependent laminar flow: parallel flows," J. Appl. Math. Physics, Vol. 16, pp. 233-254, 1965.

24. Tollmien, W., "The production of turbulence," NACA TN 609, 1931.

25. Schlichting, H., "Amplitudenverteilung und Energiebilanz der Kleinen Storungen bei der Plattenstromung," Nach. Gesell. d. Wiss. Z. Gottingen, Math. Phys. Klasse, Bd. I., 1935, pp. 4778.

26. Betchov, R. and Criminale, W., Stability of Parallel Flows, Academic Press, NY, 1967.

27. Jordinson, R., "The flat plate boundary layer. Part 1. Numerical integration of the Orr-Sommerfeld Equation," Journal of Fluid Mechanics, 43, October 1970, 801-811.

28. Saric, W.S. and Nayfeh, A.H., "Nonparallel stability of boundary-layer flows," The Physics of Fluids, Vol. 18, #8, Aug. 1975, pp. 945-950.

29. Schubauer, G.B. and Skramstad, H.K., "Laminar boundary layer oscillations and transition on a flat plate," NACA Report 909, 1948.

30. Ross, J.A., Barnes, F.H., Burns, J.G., and Ross, M.A.S., "The flat plate boundary layer. Part 3. Comparison of theory with experiment," Journal of Fluid Mechanics 43, October 1970, 819-832.

31. Rayleigh, Lord (1880), "On the stability or instability of certain

fluid motions," Scientific papers, Vol. 1, pp. 474, 487, Cambridge Univ. Press, England.

32. Fjørtoft, R., "Application of integral theorems in deriving criteria of stability for laminar flows and for the baroclinic circular vortex," Geophy. Publ., 17(5), 1950.

33. Reshotko, Eli, "Boundary layer stability and transition," Annual Reviews of Fluid Mechanics 8, 1976, pp. 311-350.

34. Tani, Itiro, "Boundary layer transition," Annual Reviews of Fluid Mechanics 1, 1969, pp. 169-196.

35. Obremski, H.J., et al., A portfolio of stability characteristics of incompressible boundary layers, AGARDOGRAPH report 134, March 1969.

36. Lees, L. (1947). The stability of the laminar boundary layer in a compressible fluid. NACA Tech. Rept., No. 876.

37. Tetervin, N. (1959). "Charts and tables for estimating the stability of the compressible laminar boundary layer with heat transfer and arbitrary pressure gradient." NASA Memo 5-4-59L.

38. Davis, Stephen H., "The stability of time periodic flows," Annual Reviews of Fluid Mechanics 8, 1976, pp. 57-74.

39. Davey, A., "A simple numerical method for solving Orr-Sommerfeld problems," School of Mathematics, Univ. of Newcastle upon Tyne, October 1972 (unpublished).

40. Mack, J.E., "Density measurements in shock tube flow with the chrono-interferometer," Lehigh Univ., Inst. of Research, Tech. Rept. 4 (1954).

41. Brown, G.L., "Theory and application of heated films for skin friction measurements," Proc. of the 1967 Heat Trans. and Fluid Mech. Inst., pp. 361-381.

42. Liepmann, H.W., "A simple derivation of Lighthill's heat transfer formula," Journal of Fluid Mechanics, 3, pp. 357-360, 1958.

43. Curle, N., The laminar boundary layer equations, Oxford Mathematical Monograms, 1962.

44. Tetervin, N. and Levine, D.A., "A study of the stability of the boundary layer as affected by changes in the boundary layer thickness in regions of pressure gradient and flow through surfaces," NACA TN 2752, 1952.

45. Elder, J.W., "An experimental investigation of turbulent spots and breakdown to turbulence," Journal of Fluid Mechanics 9, 235-246, 1960.

46. Swigart, R.J., "Roughness induced boundary layer transition on blunt bodies," AIAA J10, 1355-1356, October 1972.

47. Dryden, H.L., "Review of published data on the effect of roughness on transition from laminar to turbulent flow," Journal of the Aerospace Sciences, 20, p. 477, 1953.

48. Morkovin, M.V., "On the many faces of transition," Viscous Drag Reduction, Plenum Press, 1969.

49. Bellhouse, B.J. and Schultz, D.L., "Determination of mean and dynamic skin friction, separation and transition in low-speed flow with a thin-film heated element," Journal of Fluid Mechanics 24, 379-400, 1966.

50. King. L.V., "On the convection of heat from small cylinders in a stream of fluid," Phil. Trans. Royal Soc. (London), V. A214, p. 373, 1914.

51. Billington, I.J., The hot-wire anemometer and its use in non-steady flow, Univ. of Toronto, UTIA, Tech. Note #5, September 1955.

52. Afimiwala, K., M.S. Thesis, State University of New York at Buffalo, Mechanical Engineering, 1974.

53. Lowel, R.L. and Roshotko, E., "Numerical study of the stability of a heated water boundary layer," Case Western Reserve University,

Report FTAS TR73-93, January 1974.

54. Asbridge, J.R., An Interferometer study of shock tube boundary layers, Lehigh University Tech Rep. 14, 1959.

55. Gooderum, P.B., An experimental study of the turbulent boundary layer on a shock tube wall, NACA TN 4243, 1958.

56. Jaffe, N.A., Okamura, T.T. and Smith, A.M.O., "Determination of spatial amplification factors and their application to predicting transition," AIAA Journal, February 1970.

57. Hall, J.G., "Laminar boundary layers developed within unsteady expansion and compression waves," AIAA Journal, V. 10, #4, 1972, 499-505.

58. Squire, H.B., "On the stability of three-dimensional distribution of viscous fluid between parallel walls," Proc. of the Royal Society of London, A.142, pp. 621-628(1933).

59. Orr, W.M., Proc. Royal Irish Acad. [A] 27, p. 69-138, 1907.

TABLE I

$Re = \frac{U_\infty \delta^*}{\nu}$	Jordinson		Present	
	k_r	ω_r	k_r	ω_r
2600	.2973	.0947	.29734	.09465
1800	.3212	.1088	.32123	.10876
1000	.3512	.1306	.3512	.1306
520	.3012	.1193	.30122	.11927
764	.2011	.0697	.20111	.06967
964	.1746	.0568	.17457	.05681
1364	.1455	.0433	.1455	.04333
2164	.1289	.036	.1285	.0344

Test problem, comparing eigenvalues on the Blasius neutral curve obtained by Jordinson [27] with those of the presently used program (STABIL).

TABLE II

$Re_{\delta_1} = \frac{U_e \delta^*}{\nu_e}$	$k_r = k_r' \delta^*$	$\omega_r = \frac{\omega_r' \delta^*}{U_e}$
47,520	.3186	.0260
43,200	.3234	.0350
38,880	.3320	.0436
34,560	.3428	.0544
30,240	.3588	.064
26,609	.3838	.07063
25,920	.3918	.0739
25,488	.4022	.0773
25,920	.4080	.0788
26,609	.4085	.0786
30,240	.4050	.0708
34,560	.3929	.0627
38,880	.3780	.0555
43,200	.3636	.0484
47,520	.3482	.0412

Neutral stability eigenvalues k_r and ω_r for the expansion wave boundary layer at $s = 0$.

	X_S = 2.17 ft		X_S = 4.6 ft		X_S = 8.17 ft	
P_o (psia)	CENTER	CORNER	CENTER	CORNER	CENTER	CORNER
30			13.4	10.9	14.0, 14.1	13.8, 14.0
40	12.35	11.75	13.9	13.2		
45	11.15, 11.10	11.25, 11.20	13.8, 13.9, 13.8, 13.9	13.0, 13.0	16.9, 16.9	14.65, 15.25
55	11.5, 11.55	Relaminarize* $\frac{5.8}{11.5}$, $\frac{5.75}{11.45}$	13.6	11.2		
65	8.85, 9.0	4.65, 4.41	10.9, 11.3, 11.25, 11.3	Relaminarize $\frac{5.7}{12.6}$, $\frac{5.75}{10.3}$, $\frac{5.7}{12.7}$	15.65, 15.80	14.90, 14.95
85	5.7, 5.75	3.7, 3.75	8.0, 8.1, 8.1	5.0, 5.15	12.15, 12.1	6.50, 6.60
90					11.95	6.5
92					11.2, 11.1	6.55, 6.60
95					10.0	5.95
105	4.95, 4.9 4.8, 4.75	Relaminarize $\frac{1.95}{3.40}$, $\frac{1.90}{3.50}$	6.2	4.9	7.35, 7.50	5.7, 5.75
110					5.25	5.55
115	4.75, 5.0	1.75, 1.80	5.95, 6.05	4.55, 4.6	Relaminarize 5.70, 5.75	5.45, 5.35
125	3.25, 3.20	1.75, 1.90	5.9, 5.95	4.5, 4.35	4.75, 4.75	Undetectable
145	3.1, 3.0	Undetectable	5.3, 5.3	4.35, 4.35	4.4, 4.45	Undetectable

TABLE III OBSERVED EXPANSION-WAVE BOUNDARY TRANSITION TIMES IN MILLISECONDS.

* $\frac{\text{initial time of jump in FHFA output}}{\text{final time of jump in FHFA output}}$

TABLE IV

p_o (psia)	$-X_s$=2.17 ft			$-X_s$=4.5 ft			$-X_s$=8.17 ft		
	s_o	s	s_d	s_o	s	s_d	s_o	s	s_d
45.0	.797	.66	.853	.721	.583	.773	.656	.695	.701
55.0	.774	.659	.857	.708	.570	.770	----	----	----
65.0	.728	.654	.823	.646	.578	.735	.641	.627	.685
85.0	.634	.532	.749	.578	.557	.665	.588	.504	.627
90.0	----	----	----	----	----	----	.586	.550	.623
92.0	----	----	----	----	----	----	.569	.530	.607
95.0	----	----	----	----	----	----	.542	.515	.580
105.0	.558	.651	.719	.514	.501	.604	.447	.448	.507
110.0	----	----	----	----	----	----	.365	.364	.421
115.0	.587	.628	.715	.500	.498	.596	.390	.388	.442
125.0	.492	.559	.627	.497	.489	.593	.346	.354	.397
145.0	.481	.560	.641	.482	.469	.566	.332	.345	.380

Observed values of s_o, s and s_d at transition of expansion-wave boundary

τ = observed transition time

$$s_o = \frac{\tau}{\tau + t_{WH}} = \frac{X + a_o t}{a_o t}$$

$$s = (X + a_o t - e)/a_o t = s_o - \frac{e}{a_o t}$$

$$s_d = \frac{\tau}{\tau + t_d}, \quad t_d = -\frac{X_s}{a_o}$$

$$X_s = X + \bar{d}$$

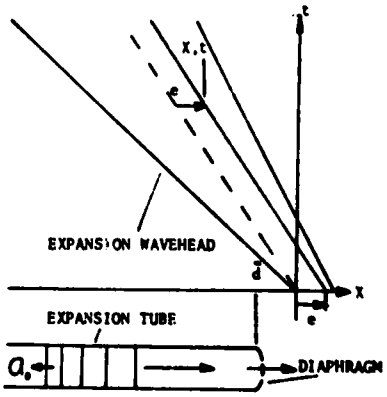

Location of the origin of X-t coordinate system along the wave-head path for plane non-centered waves.

TABLE V

P_o mm Hg	Record #	M_s	τ m sec	U_s ft/sec	u_2 ft/sec	X_p ft	Re_{X_p} x 10^{-6}	$Re_{X_{TR}}$ x 10^{-6}
50	820	1.79	1.7	2026	1161	4.62	3.72	2.77
50	820	1.81	1.45	2026	1161	4.0	3.17	2.36
52	821	1.81	1.20	2049	1186	3.38	2.90	2.11
52	821	1.81	1.15	2049	1186	2.36	2.78	2.02
99	806	1.56	1.78	1766	870	3.03	3.29	3.43
99	805	1.43	2.2	1623	682	2.59	2.20	3.03
99	805	1.43	2.55	1623	682	3.00	2.53	3.49
125	809	1.49	2.52	1675	773	4.23	4.98	4.97
189	813	1.37	3.55	1551	604	3.5	4.55	7.14
189	813	1.37	3.40	1551	604	3.35	4.36	6.84
251	815	1.26	4.00	1426	438	2.53	2.91	6.55
251	816	1.31	4.25	1483	516	3.37	3.99	7.48
251	816	1.31	4.20	1483	516	3.30	3.94	7.39
377	818	1.17	8.05	1324	297	3.08	3.45	11.57
377	818	1.17	9.15	1324	297	3.50	3.92	13.15
377	819	1.18	8.35	1336	314	3.43	3.98	12.92

Results of Present Shock-Wave Boundary Layer Transition Experiments

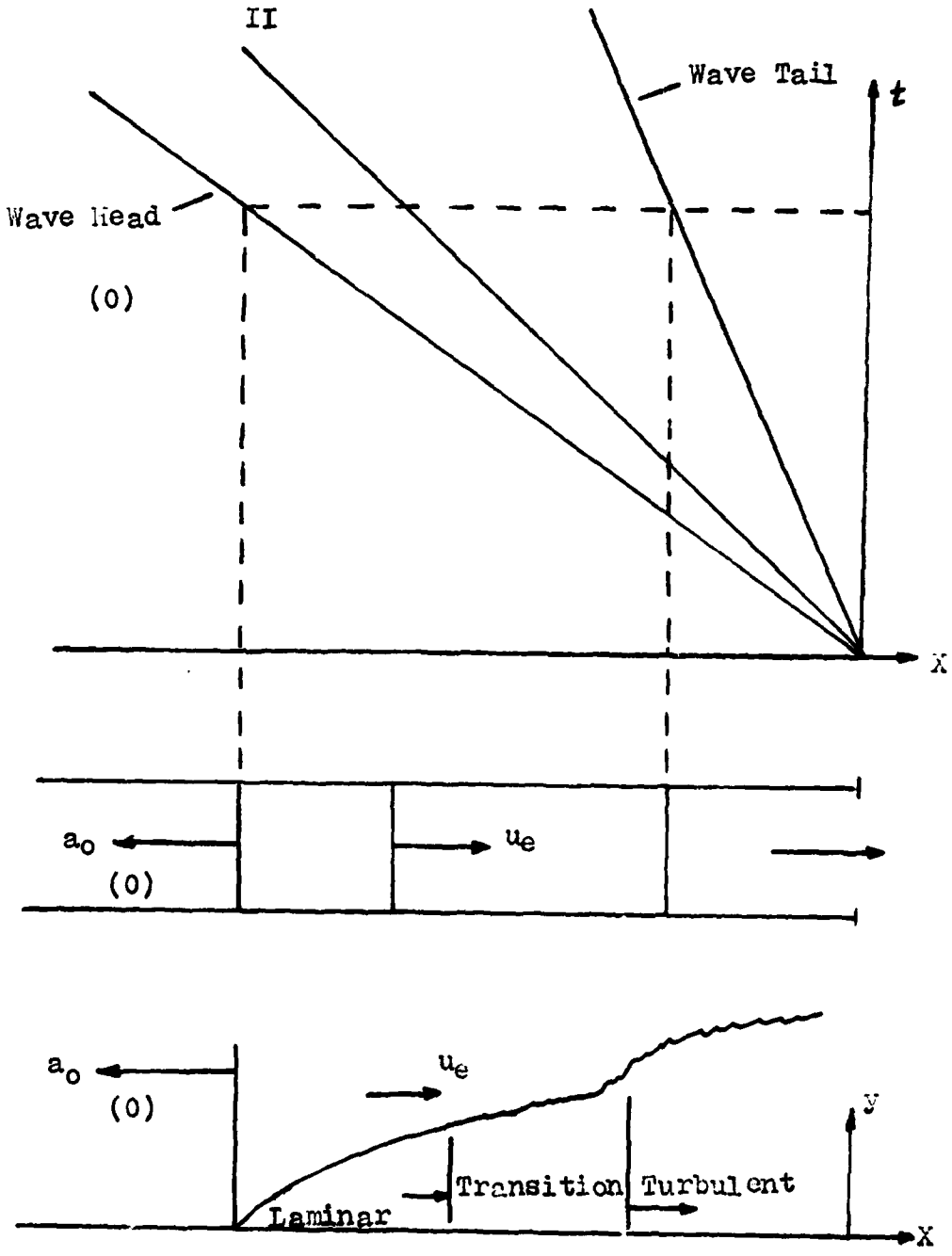

Figure 1a: Characteristic diagram and coordinates for centered expansion wave flow.

AD-A082 534 STATE UNIV OF NEW YORK AT BUFFALO FLUID AND THERMAL S--ETC F/G 20/4
STABILITY AND TRANSITION OF WALL BOUNDARY LAYERS INDUCED BY MOV--ETC(U)
JUL 79 J G HALL, Y M AMR AFOSR-74-2719

UNCLASSIFIED AFOSR-TR-80-0231 NL

2 OF 2

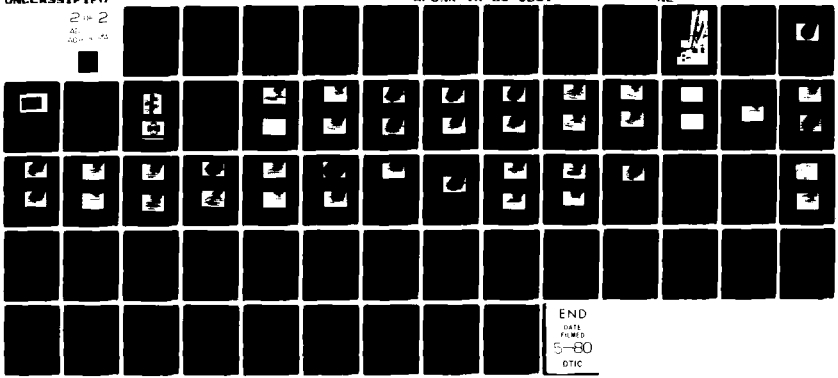

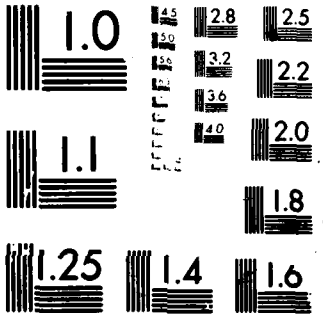

MICROCOPY RESOLUTION TEST CHART
NATIONAL BUREAU OF STANDARDS-1963-A

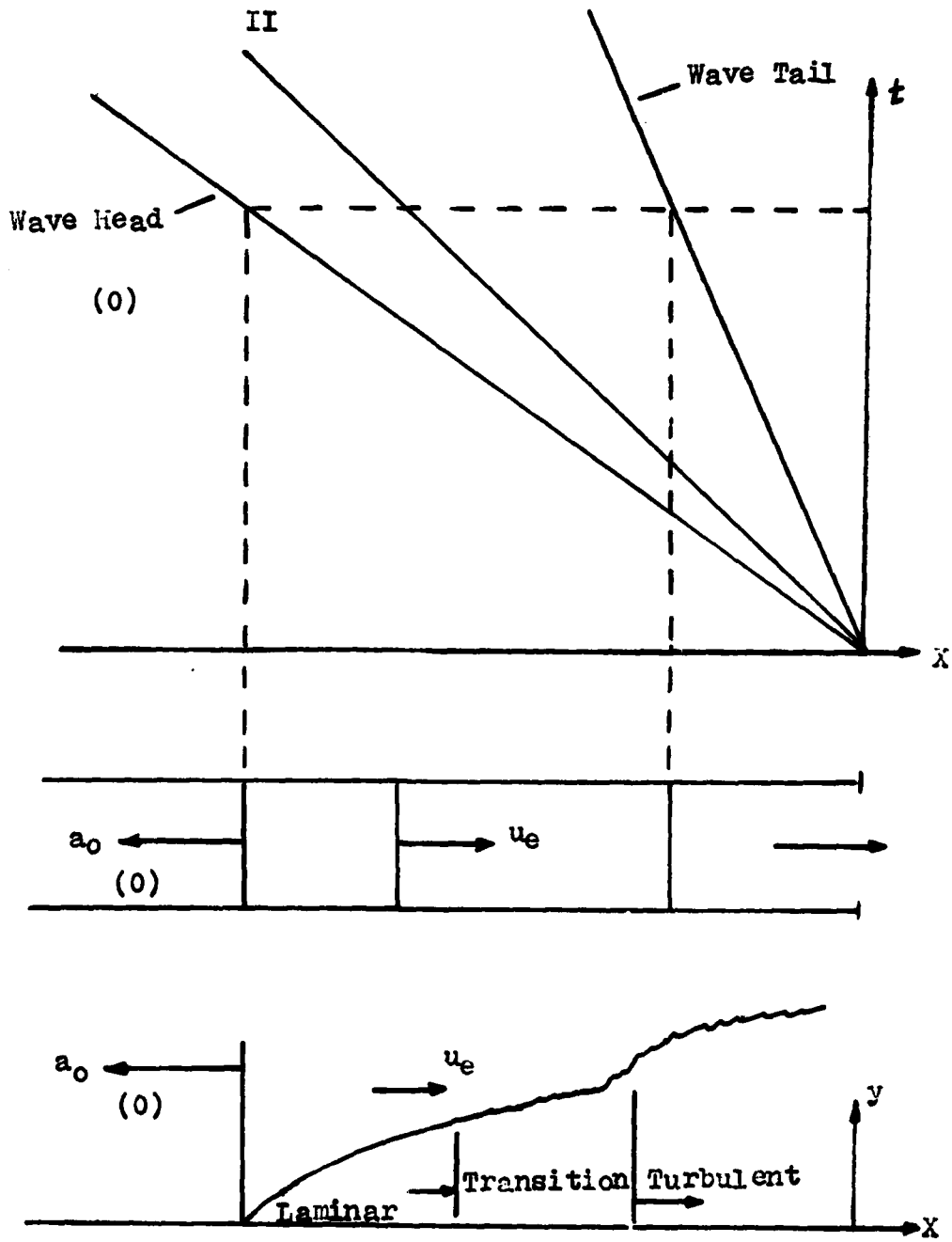

Figure 1a: Characteristic diagram and coordinates for centered expansion wave flow.

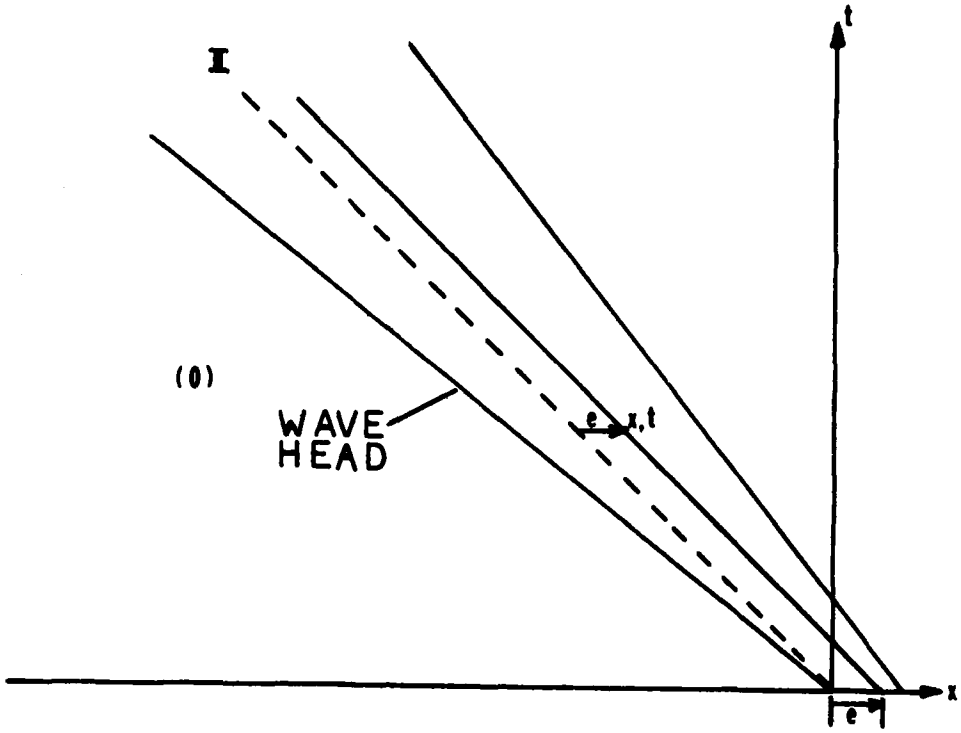

Figure 1b: Characteristic diagram and coordinates for non-centered expansion-wave flow.

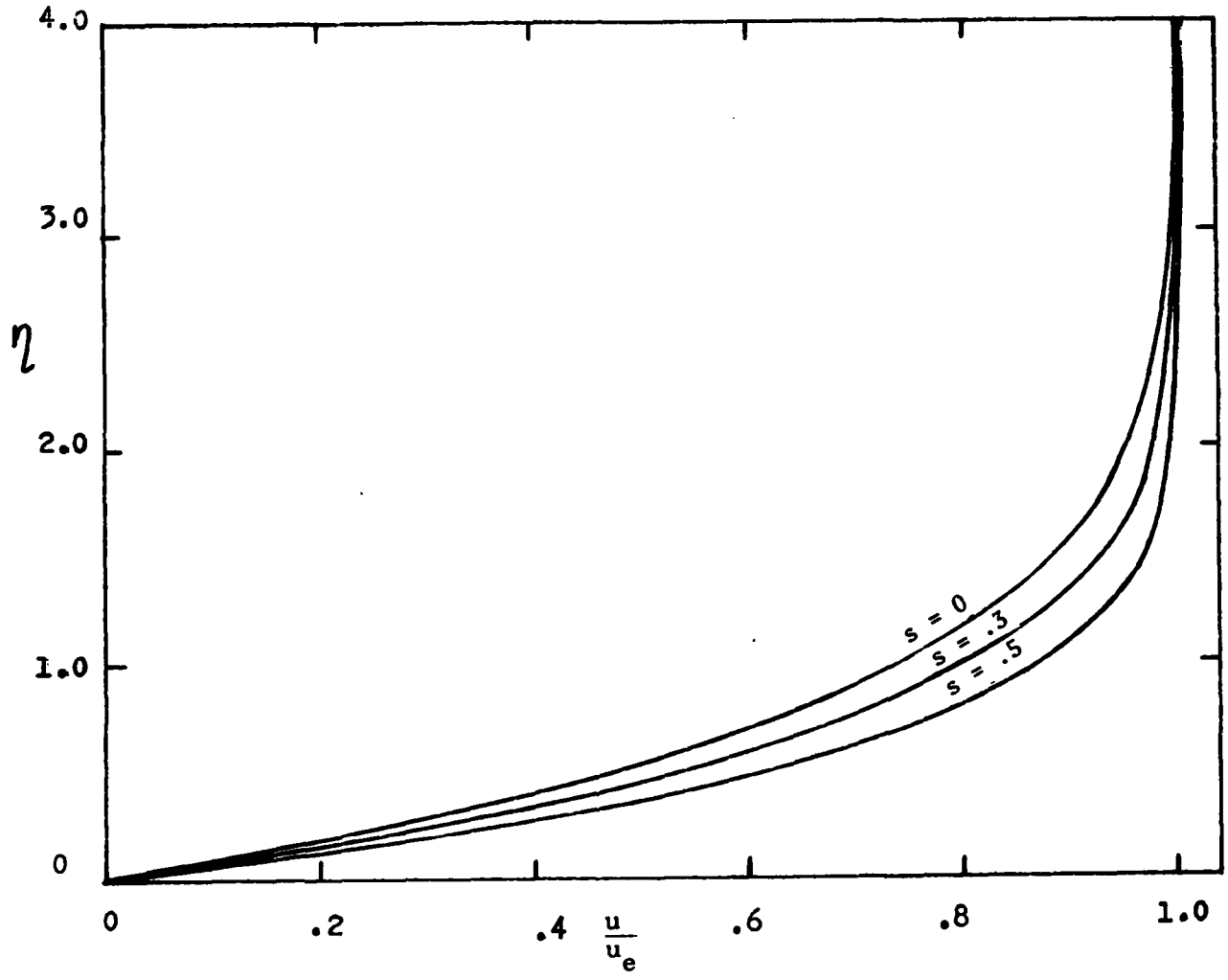

Figure 2: Velocity profiles of expansion wave boundary layer for different s.

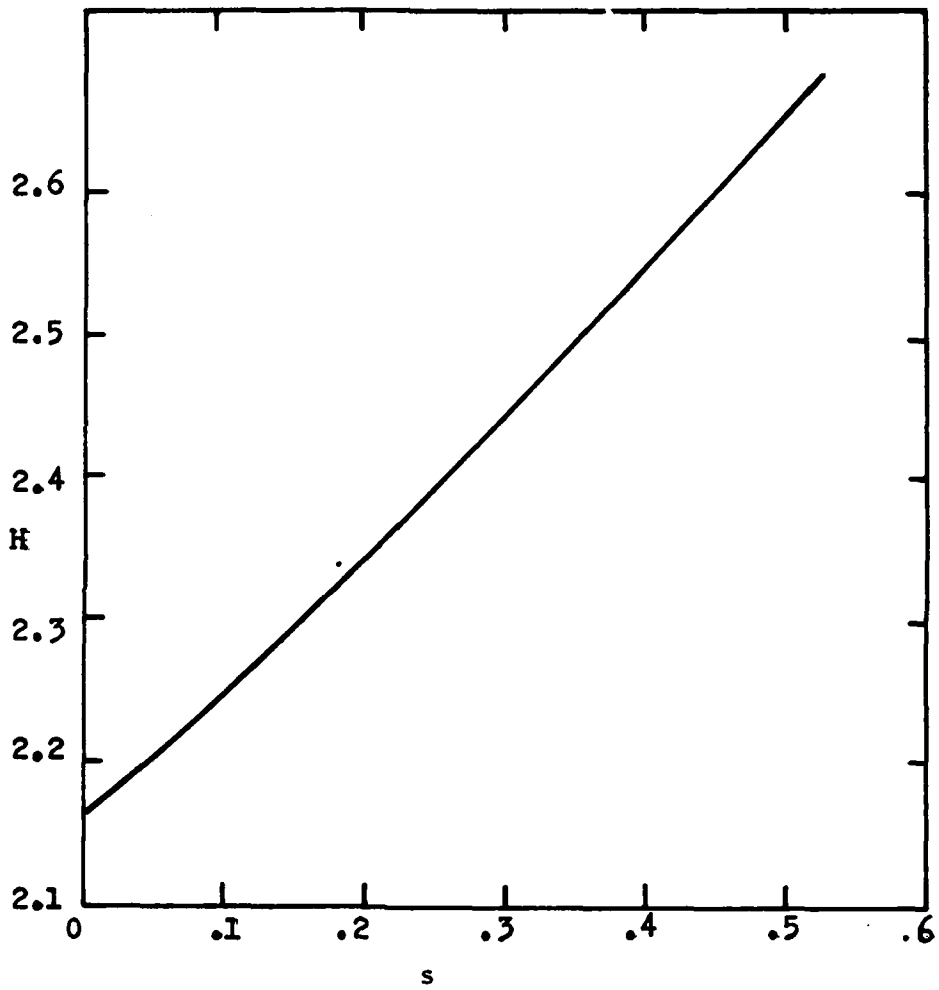

Figure 3: Shape parameter $H(s) = \delta^*/\theta$ for expansion wave boundary layer flow.

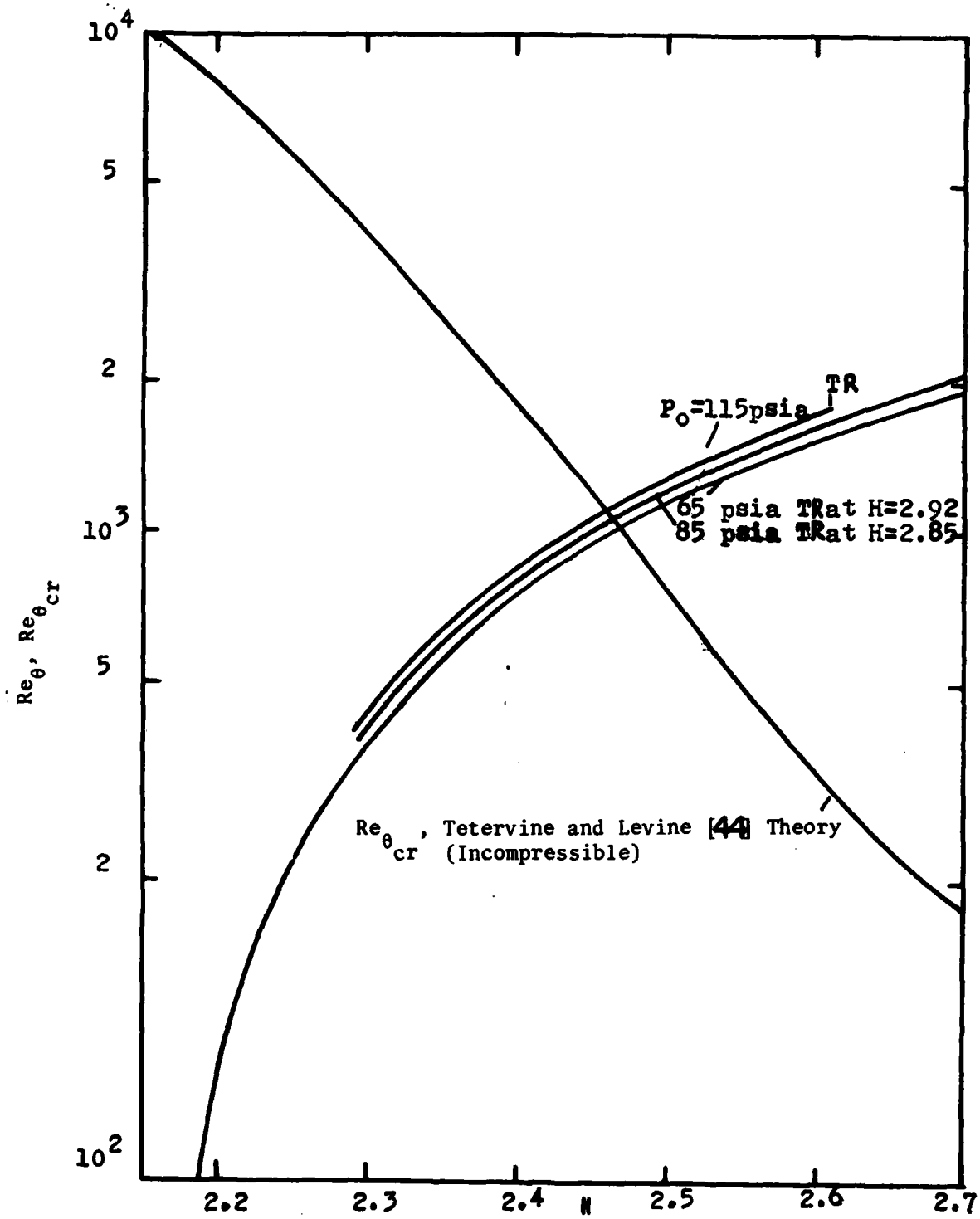

Figure 4: $Re_{\theta_{cr}}$ and Re_θ vs shape parameter H(s) along path of particles observed to undergo transition at tube station x_5 = 8.17 ft. TR = transition.

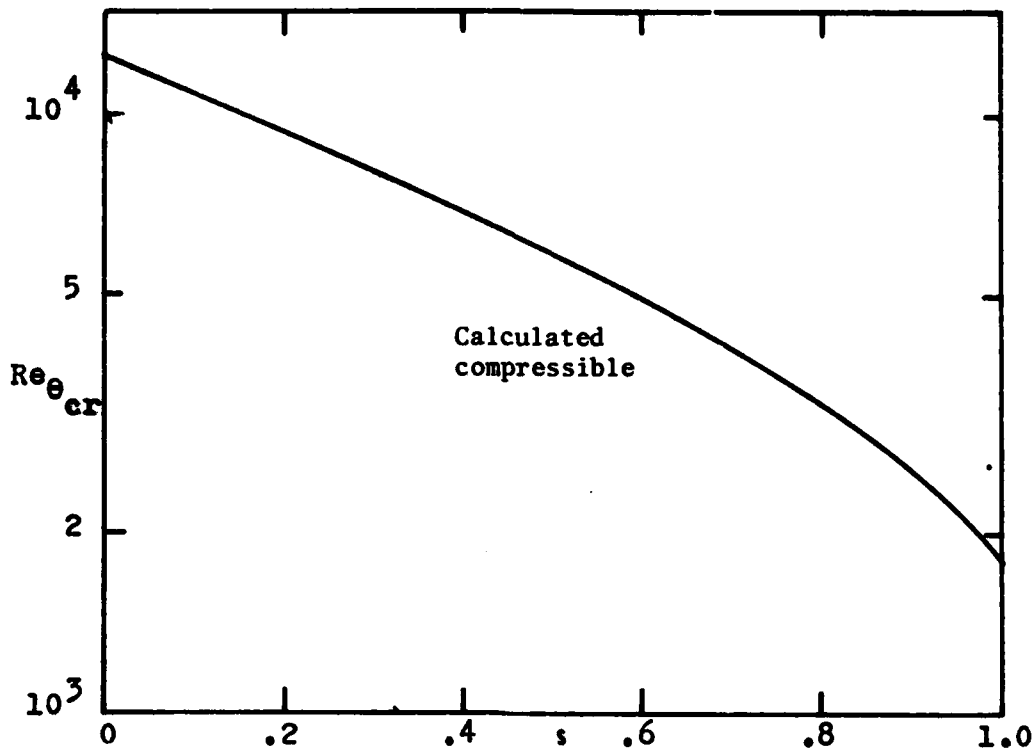

Figure 5: Calculated $Re_{\theta_{cr}}$ (s) for expansion-wave compressible boundary layer (eq. 3.14).

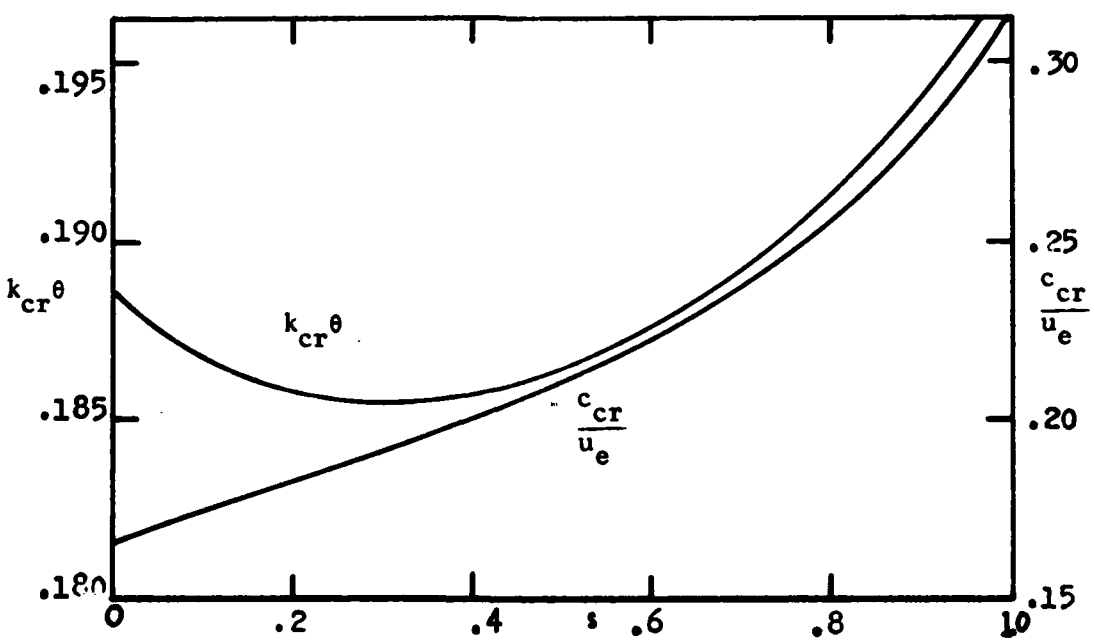

Figure 6: Calculated c_{cr} and k_{cr} for expansion wave compressible boundary layer (eq. 3.15).

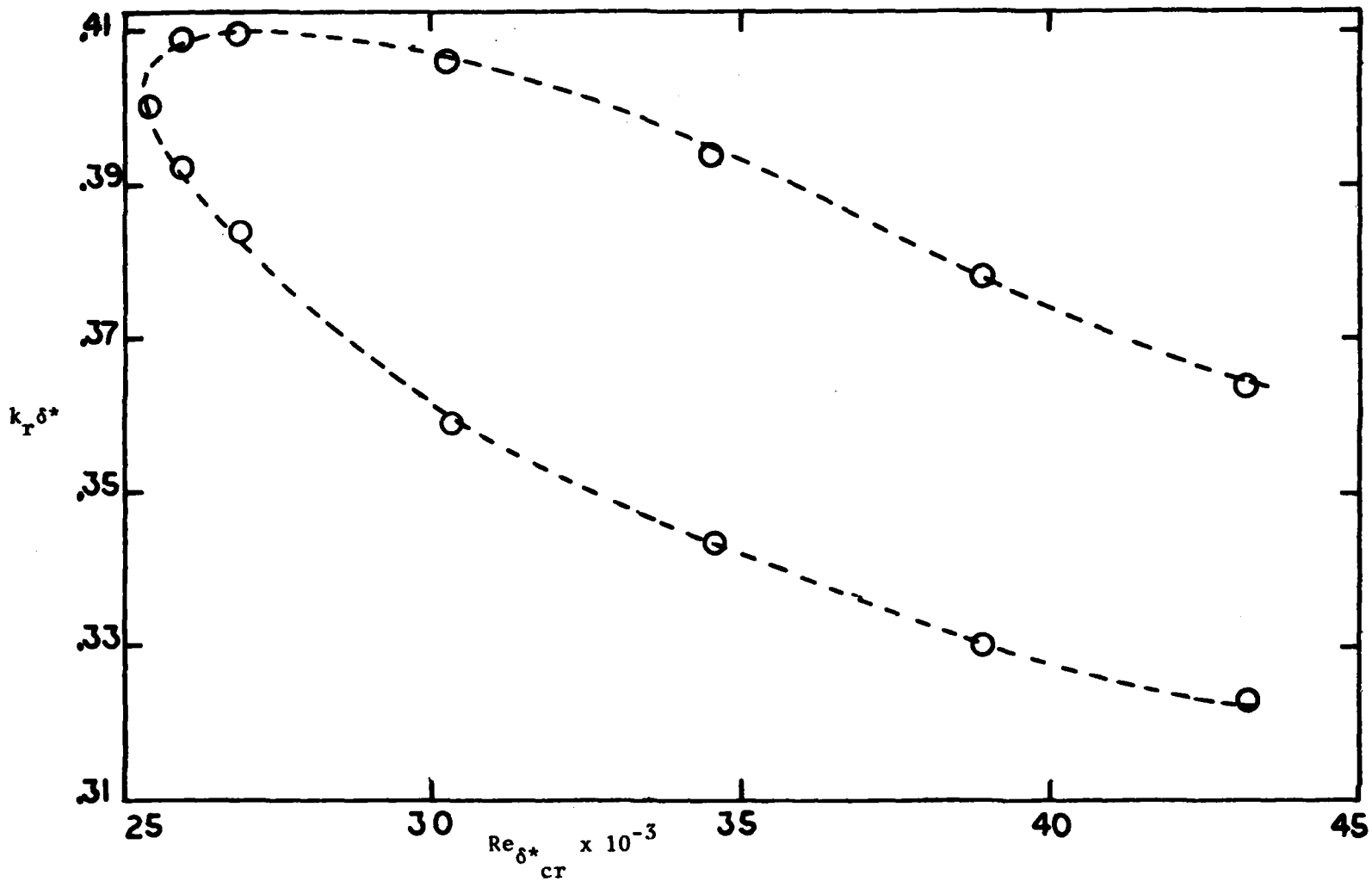

Figure 7: Calculated neutral stability curve for expansion wave boundary layer at the wavehead.

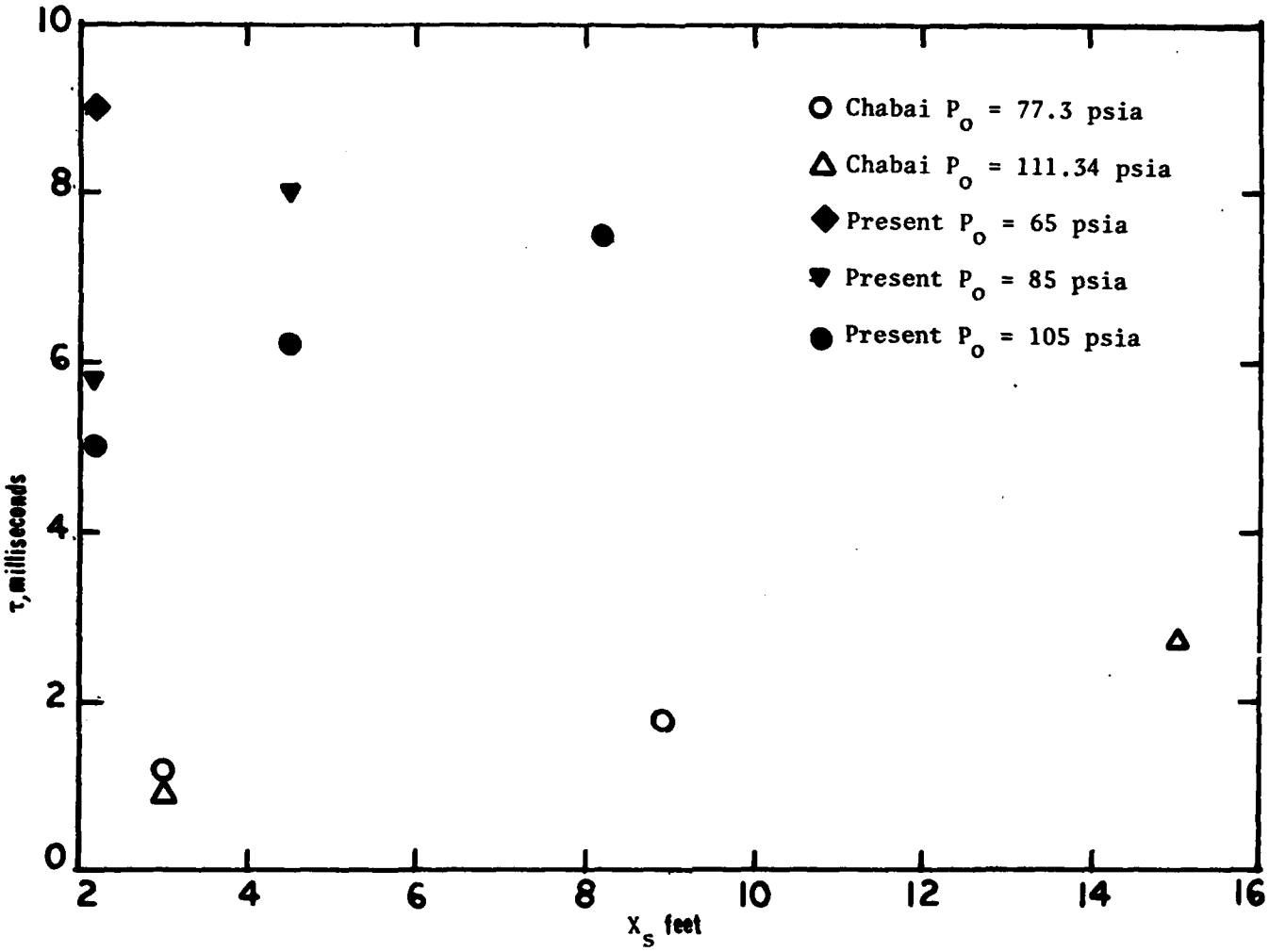

Figure 8: Some comparison of expansion wave boundary layer transition times τ observed by Chabai (N_2) and in the present experiment (dry air).

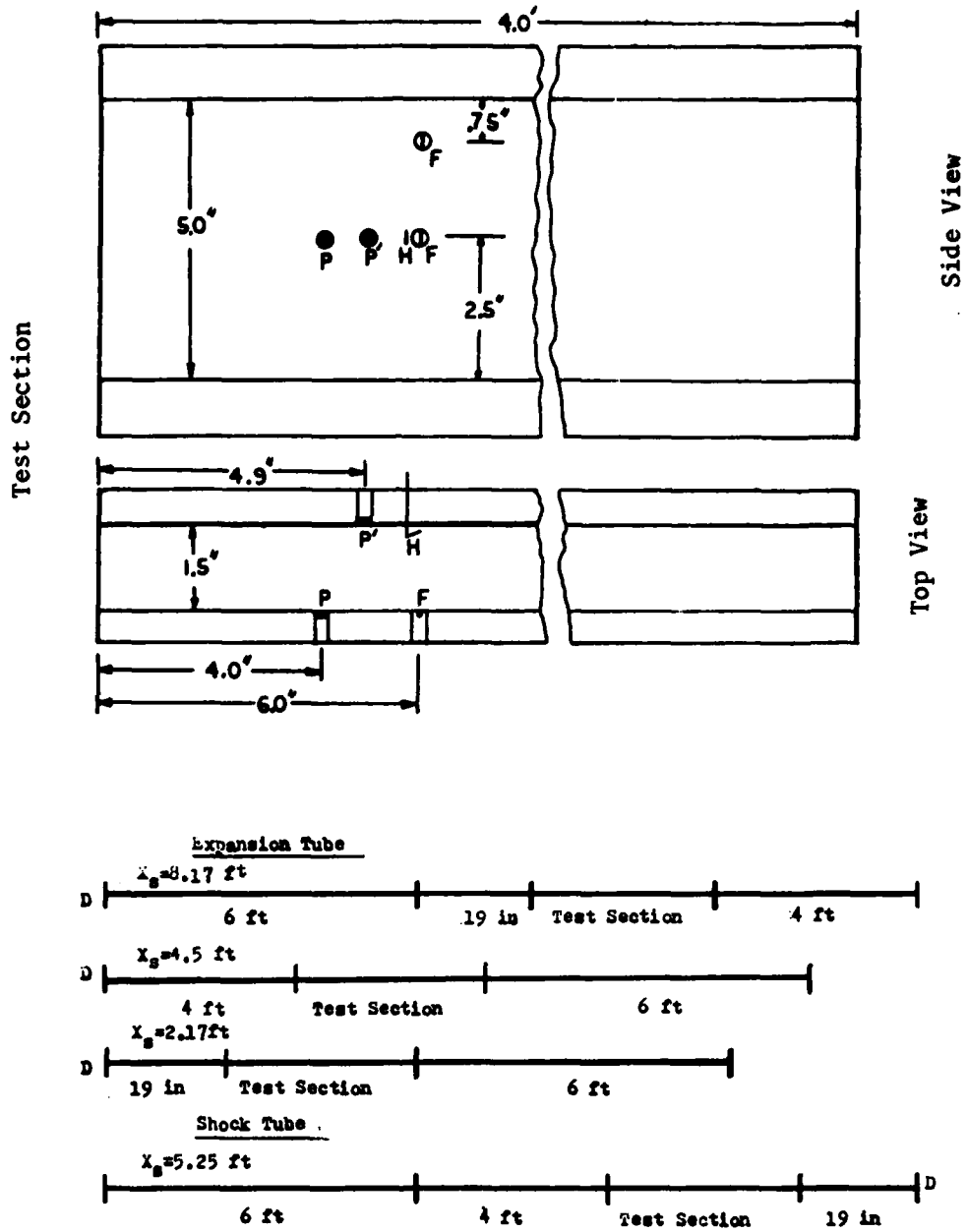

P': Pressure Transducer when Hot Wire is not used

P: Pressure Transducer

H: Hot-Wire Anemometer

F: Flush Hot-Film Anemometer

D: Mylar Diaphragm

Figure 9: Expansion and shock tube configurations.

Figure 10: Photograph of apparatus.

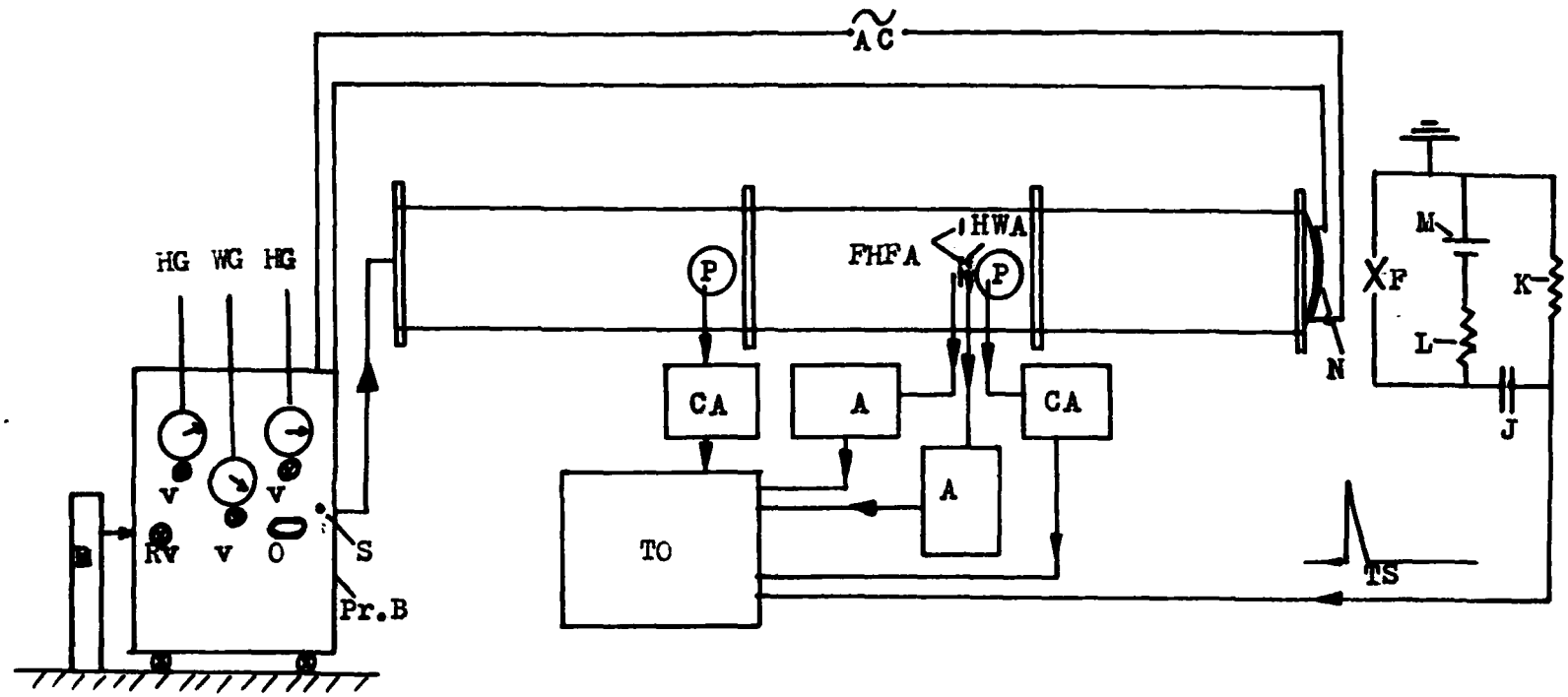

A : Disa 55D01 Anemometer.
AC: Rheostat controled AC Source.
B : Compressed Dry Air Bottle.
CA: Charge Amplifier.
F : Aluminum Foil.
HG: Heise Pressure Gauges.
J : Condenser (.01 MF).
K : Resistor (1 Mega Ω).
L : Resistor (.1 Mega Ω).
FHFA: Flush Hot Film Probe.
HHWA : Hot Wire Anemometer.

M: Battery(9 volts).
N: Nichrome Wire.
O: One Way Vacuum Valve.
P: Kistler Pressure Transducers.
Pr.B: Pressure Board.
Rv: Pressure Regulating Valve.
S: Push Button on-off switch.
TO: Tektronix 555 dual beam-Oscilloscope.
WG: Wallace & Tiernan Vacuum-Gauge.

Figure 11 .: Schematic of experimental apparatus and recording equipment.

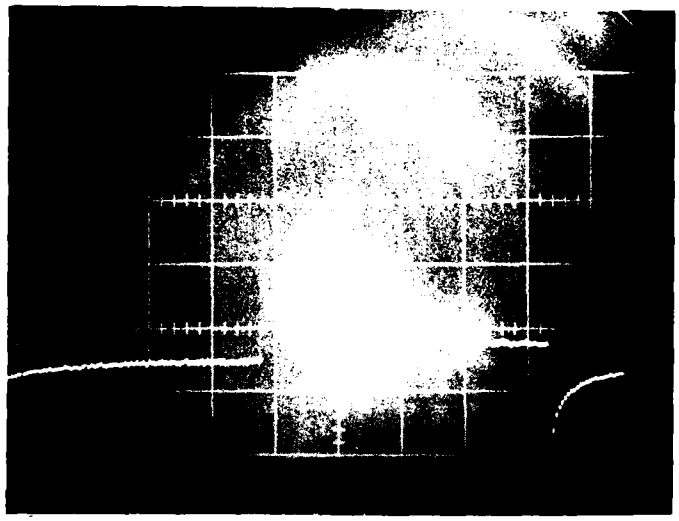

Figure 12: Response of flush hot-film anemometer to a 1.0 volt square-wave signal of approximate frequency 2k Hz, P_o = 14.6 psia.

a(film over heat ratio) = .2,

oscilloscope gain = .5 volt/cm,

sweep time = .1 m-sec/cm,

HF(anemometer high frequency setting) = 2,

Gain(anemometer gain setting) = 7.

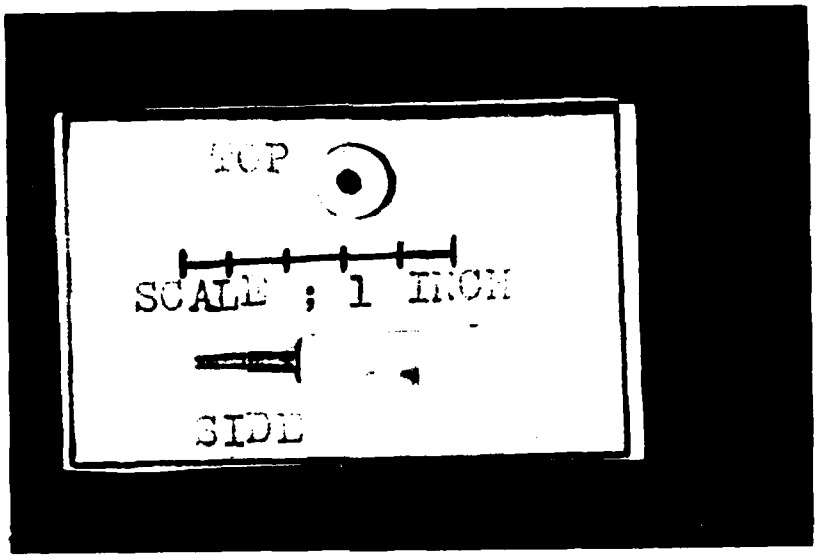

Figure 13: Photograph of FHFA viewed from top and side.

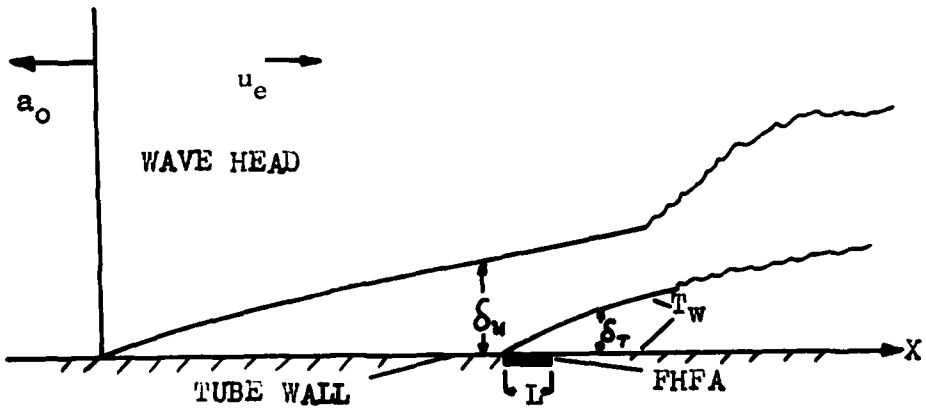

Figure 14: Instantaneous velocity and thermal boundary-layers over wall with FHFA of length L and uniform temperature T_f.

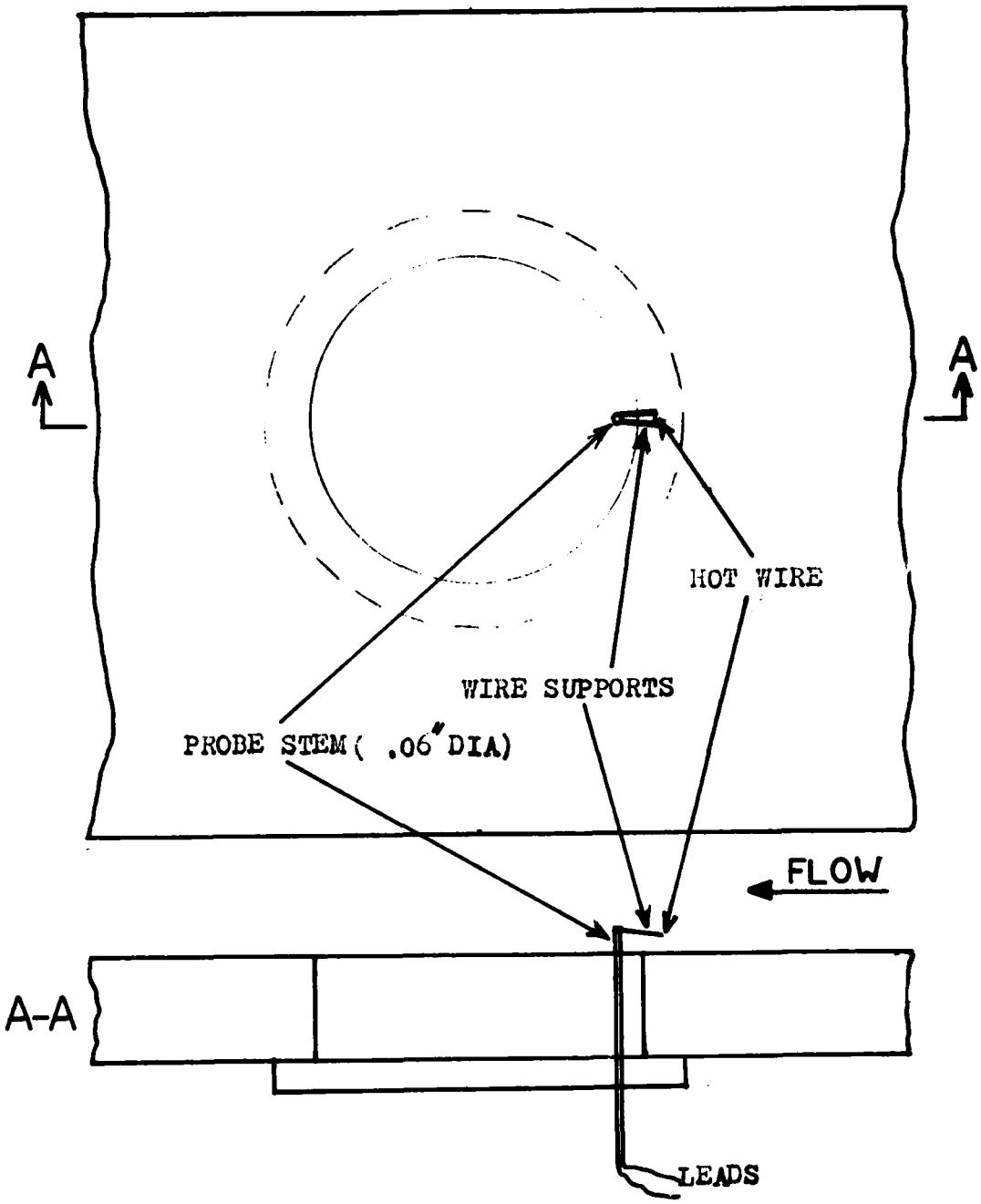

Figure 15a. Schematic diagram of hot-wire configuration.

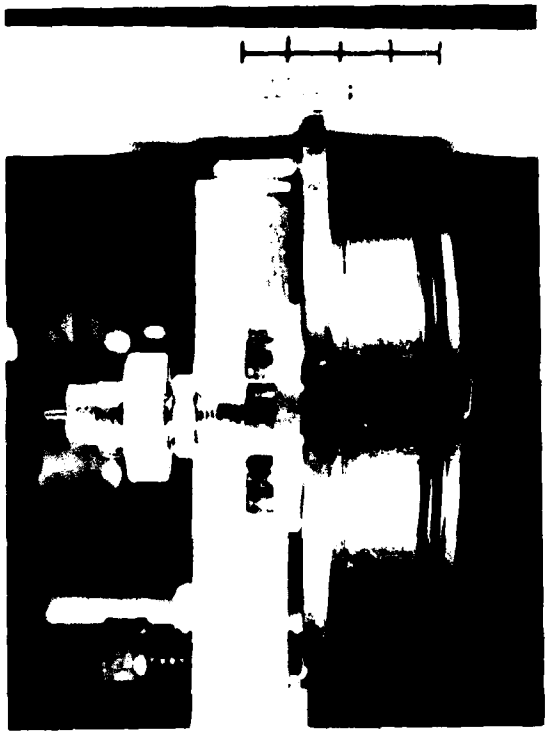

Figure 15b: Photograph of hot-wire mounted in instrumentation plug.

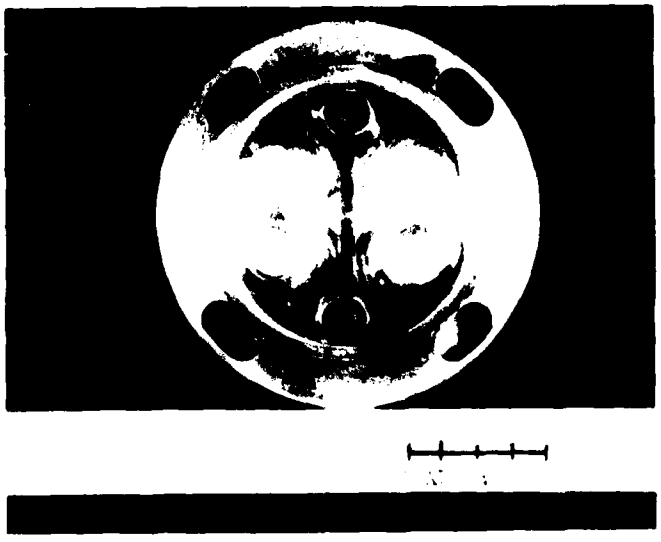

Figure 16: Photograph of thin-film thermometer.

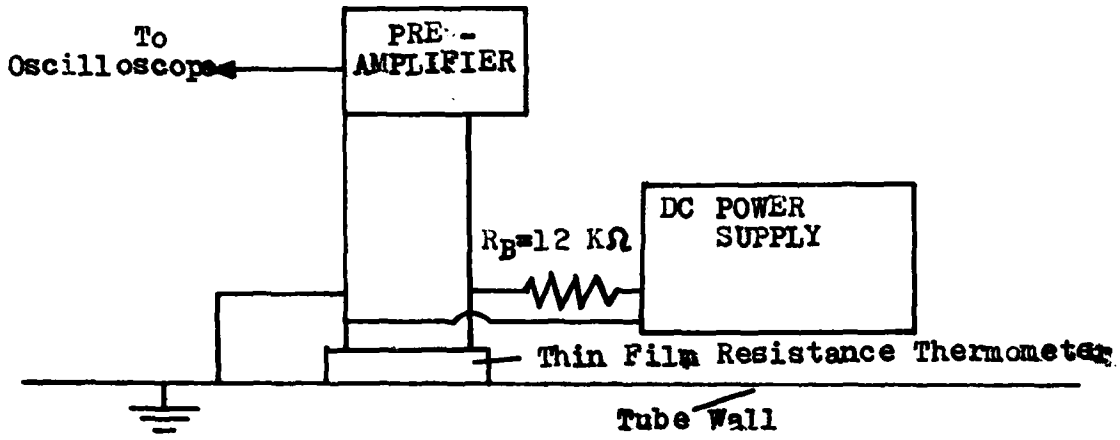

Figure 17: Schematic of experimental set up for thin-film thermometer.

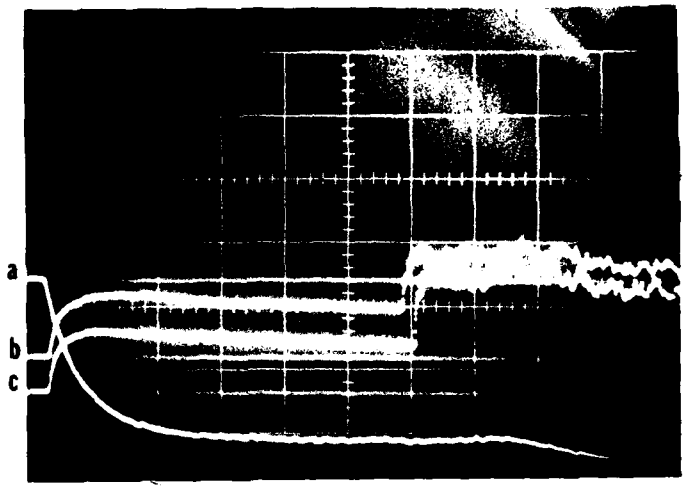

Figure 18: Oscilloscope record for expansion-wave boundary-layer measurements.

P_o = 45 psia, X_s = 2.17 ft. (a) 10 psi/cm, 2 msec/cm; (b) FHFA at corner .5 volt/cm, 2 msec/cm, R_o = 11.12Ω, a = .2; (c) FHFA at center .5 volt/cm, 2 msec/cm, R_o = 13.1Ω, a = .2.

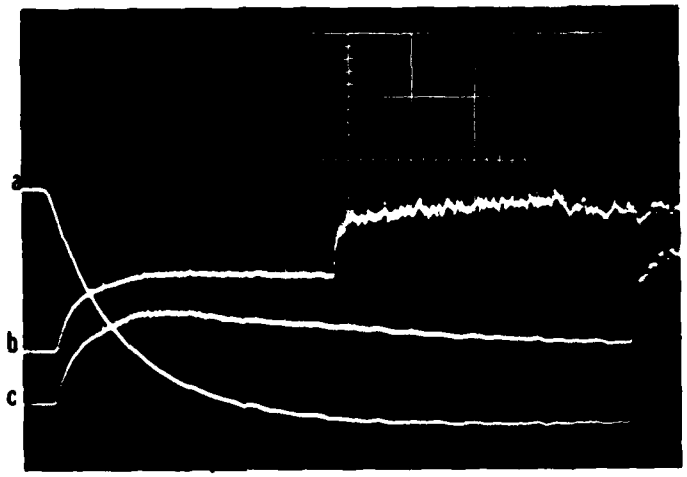

Figure 19: Oscilloscope record for expansion-wave boundary-layer measurements.

P_o = 65 psia, X_s = 2.17 ft. (a) 10 psi/cm, 1 msec/cm; (b) FHFA at corner .5 volt/cm, 1 msec/cm, R_o = 11.12Ω, a = .2; (c) FHFA at center .5 volt/cm, 1 msec/cm, R_o = 13.1Ω, a = .2.

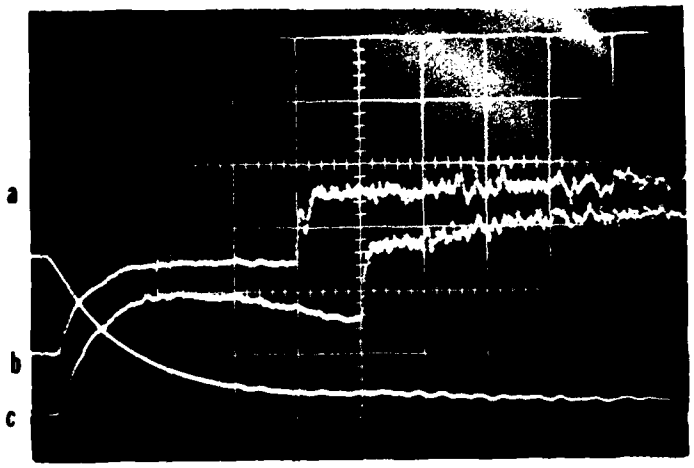

Figure 20: Oscilloscope record for expansion-wave boundary-layer measurements.

P_o = 85 psia, X_s = 2.17 ft. (a) 20 psi/cm, 1 msec/cm; (b) FHFA at corner .5 volt/cm, 1 msec/cm, R_o = 11.12Ω, a = .2; (c) FHFA at center .5 volt/cm, 1 msec/cm, R_o = 13.1Ω, a = .2.

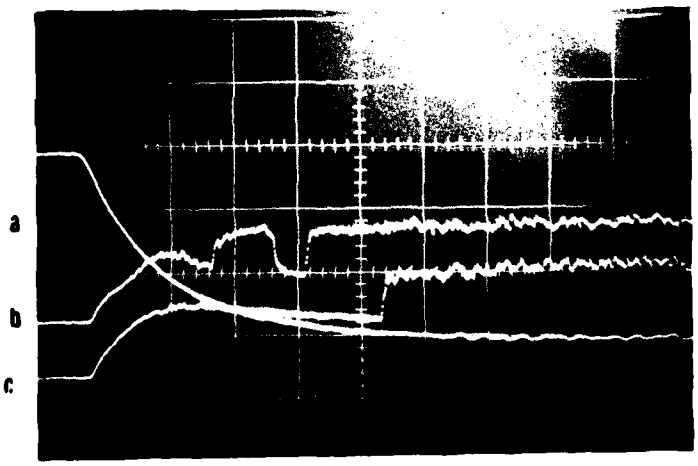

Figure 21: Oscilloscope record for expansion-wave boundary-layer measurements.

P_o = 105 psia, X_s = 2.17 ft. (a) 20 psi/cm, 1 msec/cm; (b) FHFA at corner 1.0 volt/cm, 1 msec/cm, R_o = 11.12Ω, a = .2; (c) FHFA at center 1.0 volt/cm, 1 msec/cm, R_o = 13.1Ω, a = .2.

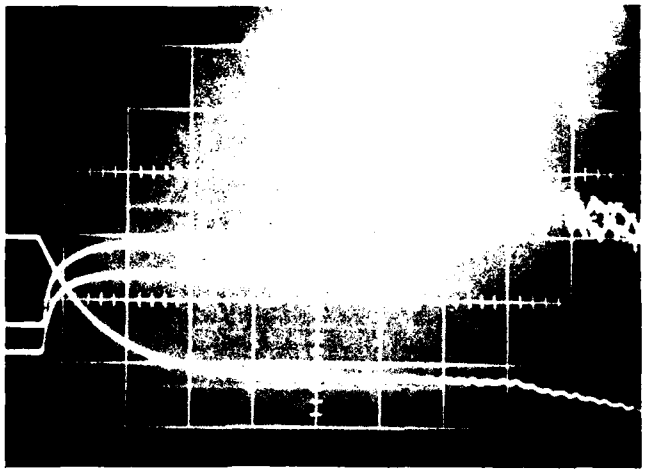

Figure 22: Oscilloscope record for expansion-wave boundary-layer measurements.

P_o = 45 psia, X_s = 4.6 ft. (a) 10 psi/cm, 2 msec/cm; (b) FHFA at corner .5 volt/cm, 2 msec/cm, R_o = 11.12Ω, a = .5; (b) FHFA at center .5 volt/cm, 2 msec/cm, R_o = 13.1Ω, a = .5.

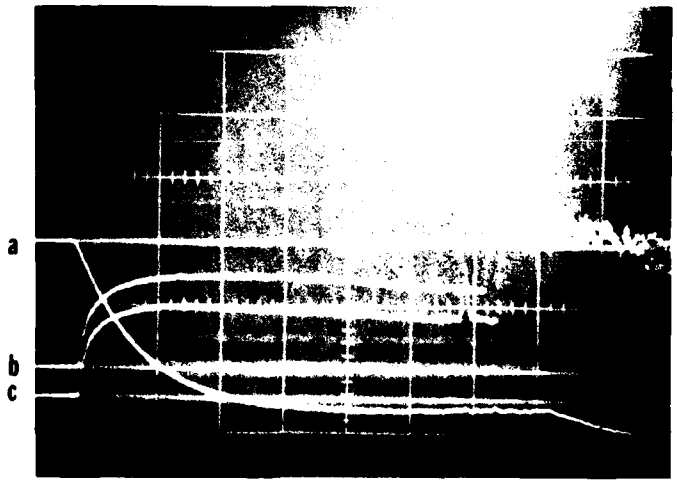

Figure 23: Oscilloscope record for expansion-wave boundary-layer measurements.

P_o = 55 psia, X_s = 4.6 ft. (a) 10 psi/cm, 2 msec/cm; (b) FHFA at corner .5 volt/cm, 2 msec/cm, R_o = 11.12Ω, a = .5; (c) FHFA at center .5 volt/cm, 2 msec/cm, R_o = 13.1Ω, a = .5.

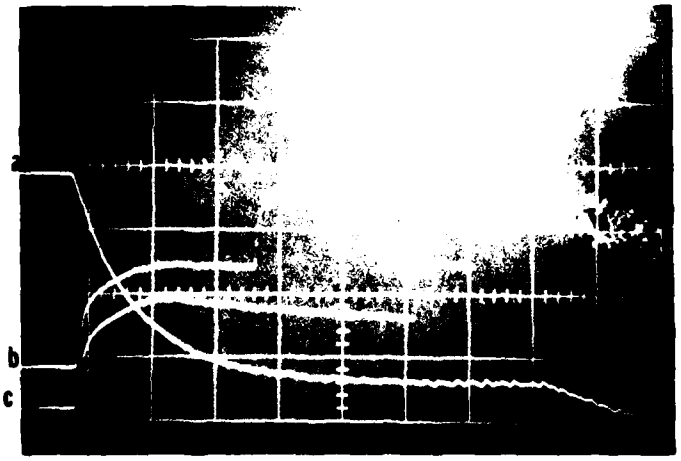

Figure 24: Oscilloscope record for expansion-wave boundary-layer measurements.

P_o = 65 psia, X_s = 4.6 ft. (a) 10 psi/cm, 2 msec/cm (b) FHFA at corner .5 volt/cm, 2 msec/cm, R_o = 11.12Ω, a = .5; (b) FHFA at center .5 volt/cm, 2 msec/cm, R_o = 11.12Ω, a = .5.

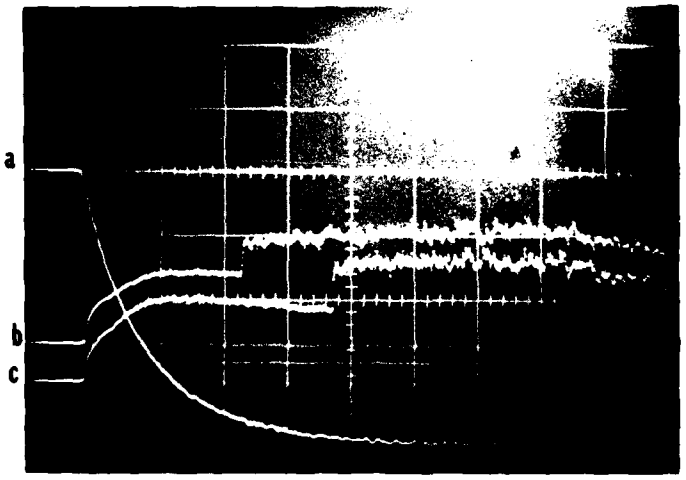

Figure 25: Oscilloscope record for expansion-wave boundary-layer measurements.

P_o = 85 psia, X_s = 4.6 ft. (a) 10 psi/cm, 2 msec/cm; (b) FHFA at corner 1.0 volt/cm, 20 msec/cm, R_o = 11.12Ω, a = .5; (c) FHFA at center 1.0 volt/cm, 2.0 msec/cm, R_o = 13.1Ω, a = .5.

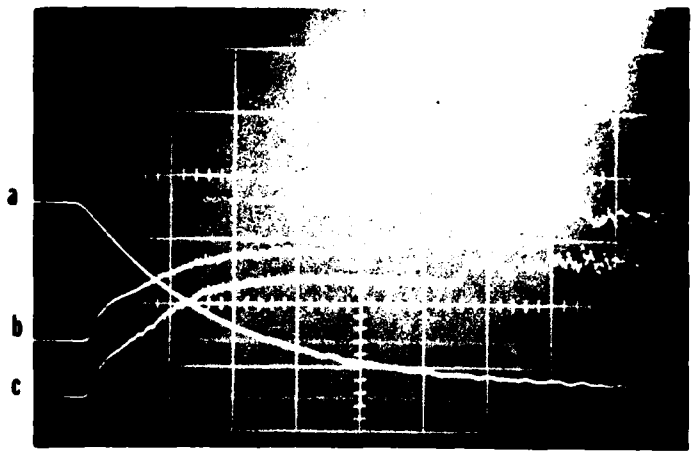

Figure 26: Oscilloscope record for expansion-wave boundary-layer measurements.

P_o = 115 psia, X_s = 4.6 ft. (a) 20 psi/cm, 1 msec/cm; (b) FHFA at corner 1.0 volt/cm, 1.0 msec/cm, R_o = 11.12Ω, a = .5; (c) FHFA at center 1.0 volt/cm, 1.0 msec/cm, R_o = 13.1Ω, a = .5.

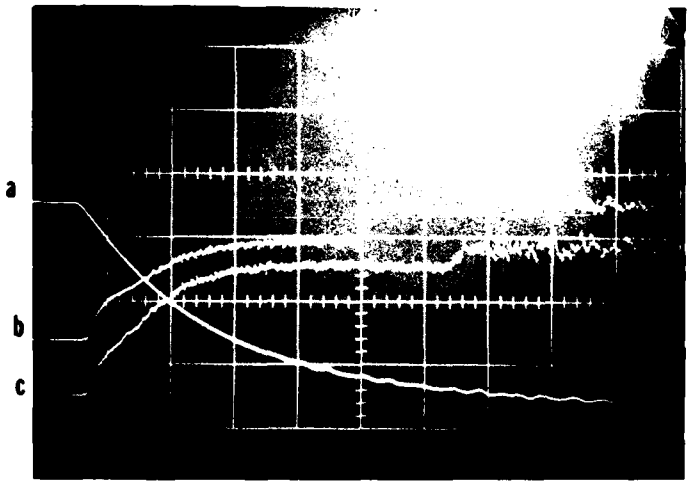

Figure 27: Oscilloscope record for expansion-wave boundary-layer measurements.

P_o = 125 psia, X_s = 4.6 ft. (a) 20 psi/cm, 1 msec/cm; (b) FHFA at corner 1.0 volt/cm, 1 msec/cm, R_o = 11.12Ω, a = .5; (c) FHFA at center 1.0 volt/cm, 1 msec/cm, R_o = 13.1Ω, a = .5.

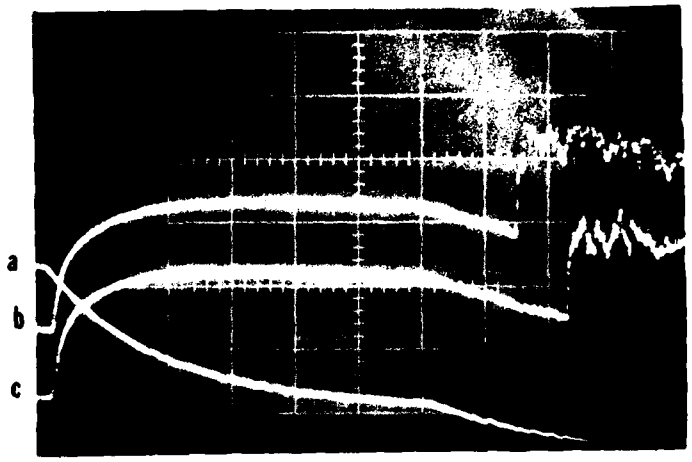

Figure 28: Oscilloscope record for expansion-wave boundary-layer measurements.

P_o = 45 psia, X_s = 8.17 ft. (a) 10 psi/cm, 2 msec/cm; (b) FHFA at corner .2 volt/cm, 2 msec/cm, R_o = 11.12Ω, a = .2; (c) FHFA at center .2 volt/cm, 2 msec/cm, R_o = 13.1Ω, a = .2.

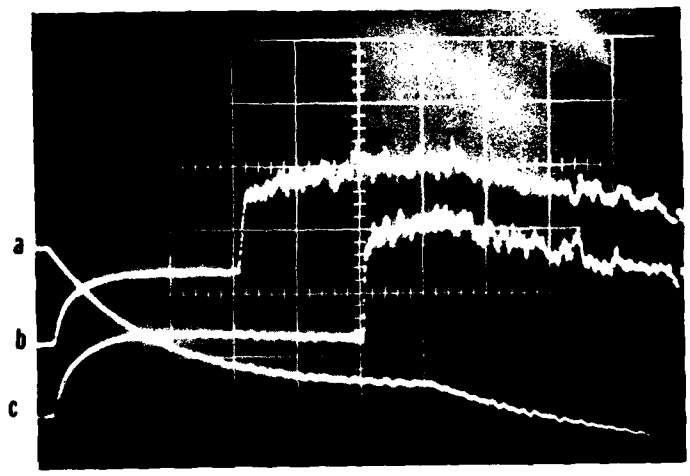

Figure 29: Oscilloscope record for expansion-wave boundary-layer measurements.

P_o = 95 psia, X_s = 8.17 ft. (a) psi/cm, 2 msec/cm; (b) FHFA at corner .5 volt/cm, 2 msec/cm, R_o = 11.12Ω, a = .2; (c) FHFA at center .5 volt/cm, 2 msec/cm, R_o = 13.1Ω, a = .2.

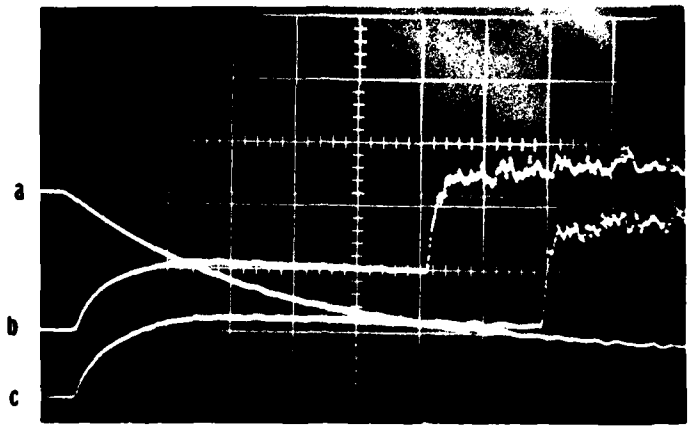

Figure 30: Oscilloscope record for expansion-wave boundary-layer measurements.

P_o = 105 psia, X_s = 8.17 ft. (a) 20 psi/cm, 1 msec/cm; (b) FHFA at corner .5 volt/cm, 1 msec/cm, R_o = 11.12Ω, a = .2; (c) FHFA at center .5 volt/cm, 1 msec/cm, R_o = 13.1Ω, a = .2.

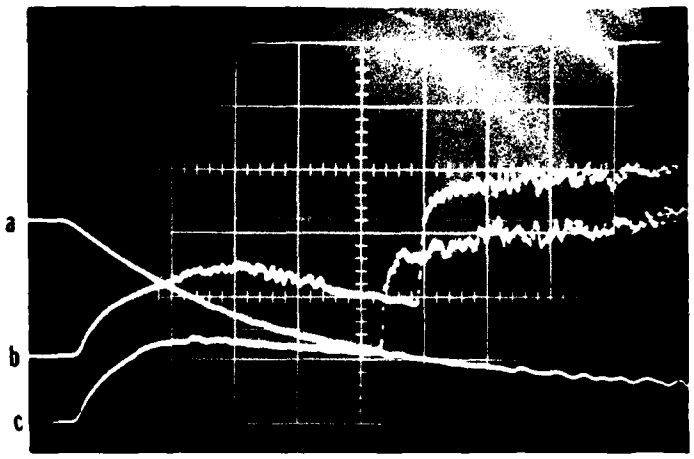

Figure 31: Oscilloscope record for expansion-wave boundary-layer measurements.

P_o = 115 psia, X_s = 8.17 ft. (a) 20 psi/cm, 1 msec/cm; (b) FHFA at corner .5 volt/cm, 1 msec/cm, R_o = 11.12Ω, a = .2; (c) FHFA at center .5 volt/cm, 1 msec/cm, R_o = 13.1Ω, a = .2.

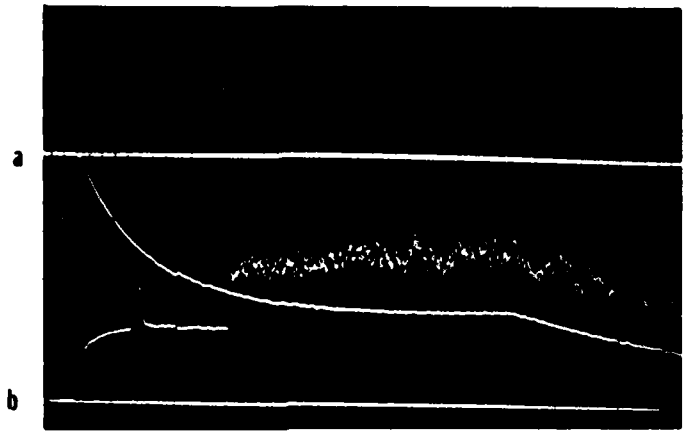

Figure 32 Oscilloscope record for expansion-wave boundary-layer measurements.

P_o = 55 psia, X_s = 5 ft. (a) 10 psi/cm, 2 msec/cm; (b) FHFA at center .5 volt/cm, 2 msec/cm, R_o = 15.4Ω, a = .5.

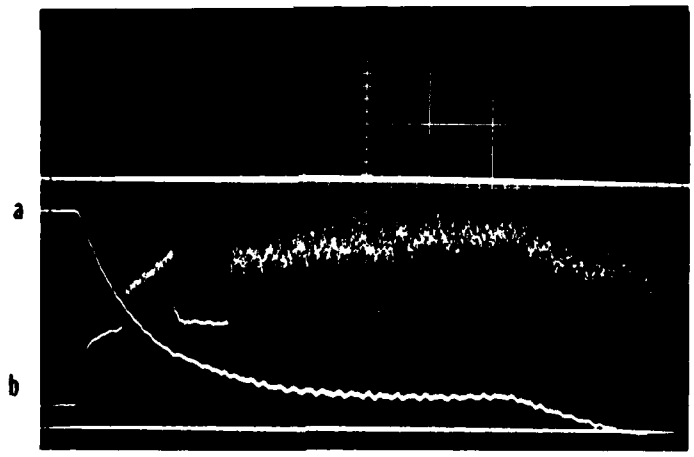

Figure 33 Oscilloscope record for expansion-wave boundary-layer measurements.

P_o = 65 psia, X_s = 5 ft. (a) 10 psi/cm, 2 msec/cm; (b) FHFA at corner .5 volt/cm, 2 msec/cm, R_o = 15.4Ω, a = .5.

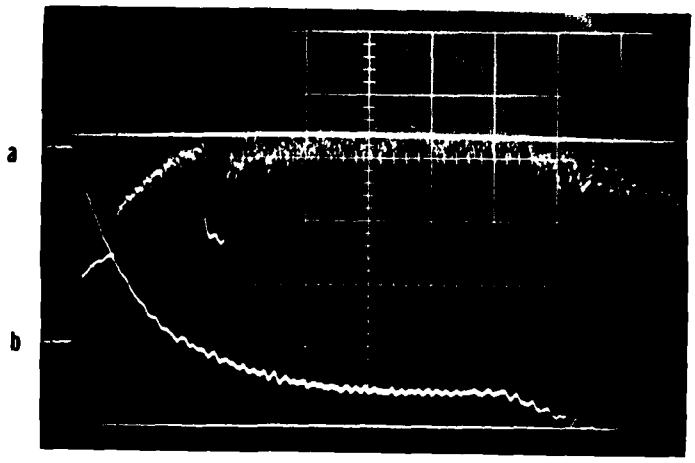

Figure 34 Oscilloscope record for expansion-wave boundary-layer measurements.

P_o = 85 psia, X_s = 5 ft. (a) 10 psi/cm, 2 msec/cm; (b) FHFA at corner .5 volt/cm, 2 msec/cm, R_o = 15.4Ω, a = .5.

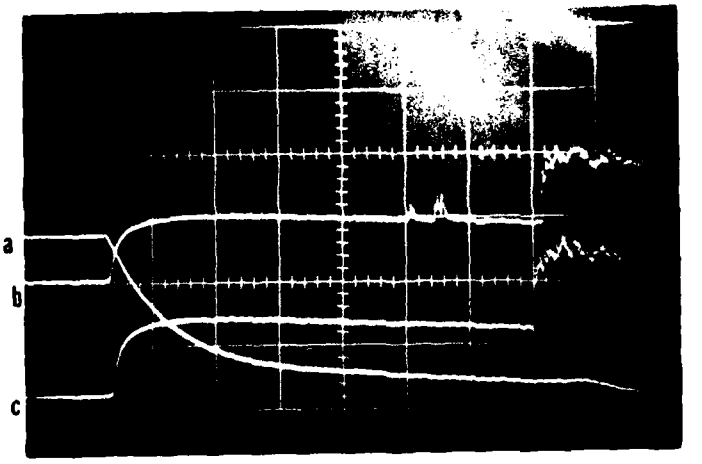

Figure 35 Oscilloscope record for expansion-wave boundary-layer measurements.

P_o = 45 psia, X_s = 4.6 ft. (a) 10 psi/cm, 2 msec/cm; (b) FHFA channel center .5 volt/cm, 2 msec/cm, R_o = 15.4Ω, a = .5; (c) FHFA plate center .5 volt/cm, 2 msec/cm, R_o = 13.1Ω, a = .5.

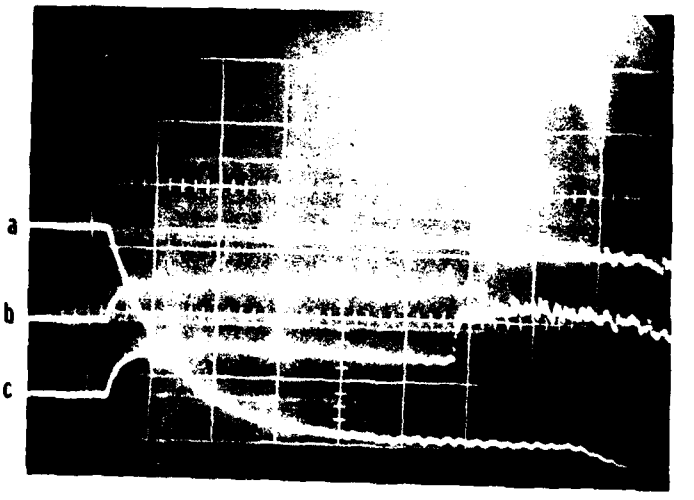

Figure 36 Oscilloscope record for expansion-wave boundary-layer measurements.

P_o = 65 psia, X_s = 4.6 ft. (a) psi/cm, 2 msec/cm; (b) FHFA channel center 1.0 volt/cm, 2 msec/cm, R_o = 15.4Ω, a = .5; (c) FHFA plate center 1.0 volt/cm, 2 msec/cm, R_o = 13.1Ω, a = .5.

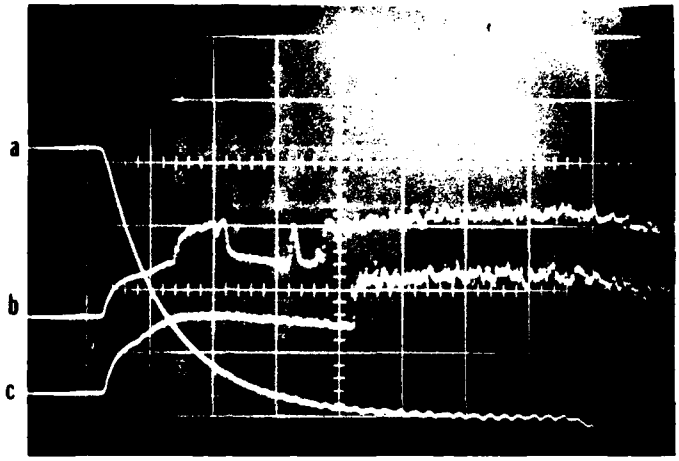

Figure 37 Oscilloscope record for expansion-wave boundary-layer measurements.

P_o = 85 psia, X_s = 4.6 ft. (a) 10 psi/cm, 2 msec/cm; (b) FHFA channel center 1.0 volt/cm, 2 msec/cm, R_o = 15.4Ω, a = .5; (c) FHFA at plate center 1.0 volt/cm, 2 msec/cm, R_o = 13.1Ω, a = .5.

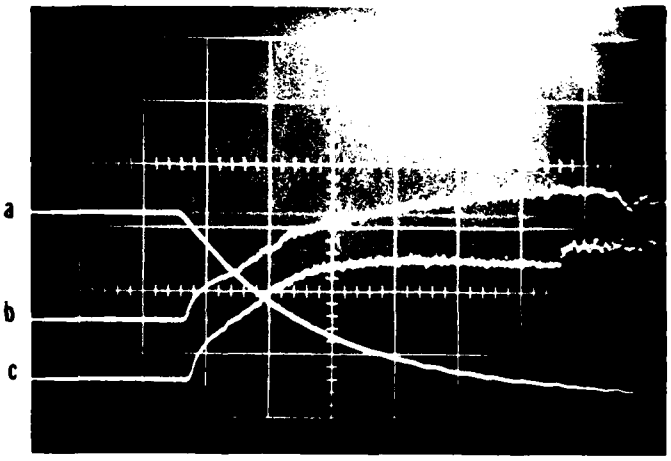

Figure 38: Oscilloscope record for expansion wave boundary-layer measurements.

p_o = 115 psia, X_s = 4.6 ft. (a) 20 psi/cm, 1 msec/cm; (b) FHFA channel center 1.0 volt/cm, 1 msec/cm, R_o = 15.4Ω, a = .5; (c) FHFA plate center 1.0 volt/cm, 1 msec/cm, R_o = 13.1Ω, a = .5.

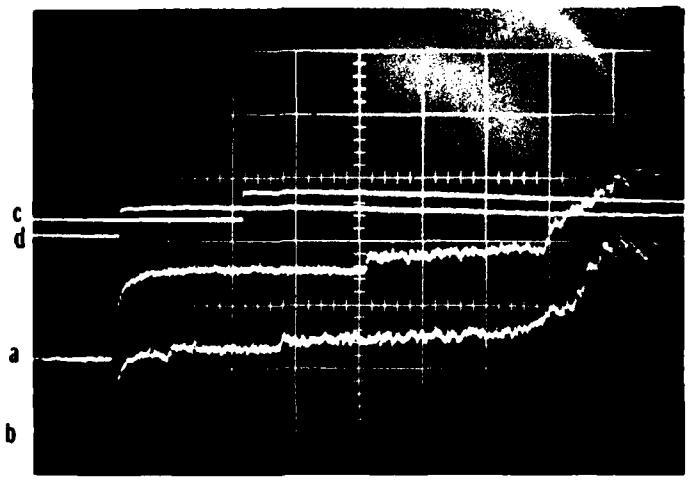

shock-wave boundary layer measurements.

Figure 39 P_o = 251 mm Hg, T_o = 26.4°C, X_s = 7.5 ft, M_s = 1.33.
(a) FHFA at corner .1 volt/cm, 1 msec/cm, R_o = 11.12Ω, a = .2.
(b) FHFA at center .1 volt/cm, 1 msec/cm, R_o = 13.1Ω, a = .2.
(c) 4 psi/cm, 1 msec/cm, X_s = 10.58 ft. (d) 4 psi/cm, 1 msec/cm, X_s = 7.63 ft.

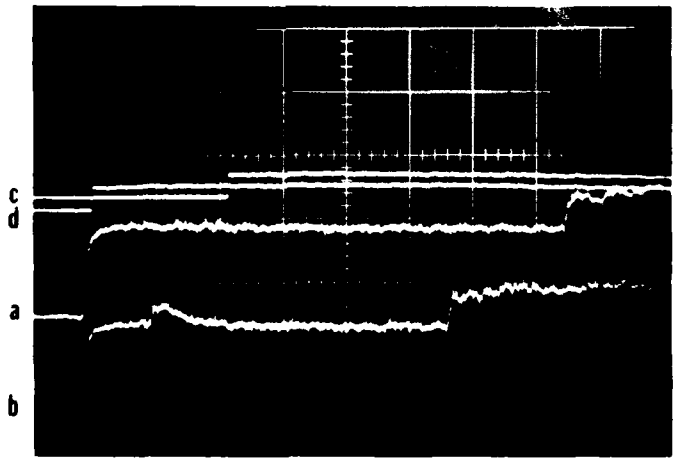

shock-wave boundary layer measurements.

Figure 40 P_o = 377 mm Hg, T_o = 26.2°C, X_s = 7.5 ft, M_s = 1.18.
(a) FHFA at corner .1 volt/cm, 1 msec/cm, R_o = 11.12Ω, a = .2.
(b) FHFA at center .1 volt/cm, 1 msec/cm, R_o = 13.1Ω, a = .2.
(c) 4 psi/cm, 1 msec/cm, X_s = 10.58 ft. (d) 4 psi/cm, 1 msec/cm, X_s = 7.63 ft.

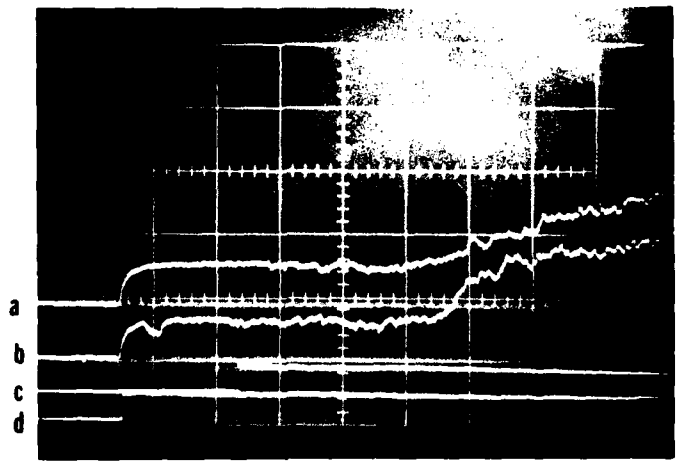

shock-wave boundary layer measurements.

Figure 41 P_o = 189 mm Hg, T_o = 26.3°C, X_s = 7.5 ft, M_s = 1.40.
(a) FHFA at corner .1 volt/cm, 1 msec/cm, R_o = 11.12Ω, a = .2.
(b) FHFA at center .1 volt/cm, 1 msec/cm, R_o = 13.1Ω, a = .2.
(c) 4 psi/cm, 1 msec/cm, X_s = 10.58 ft. (d) 4 psi/cm, 1 msec/cm, X_s = 7.63.

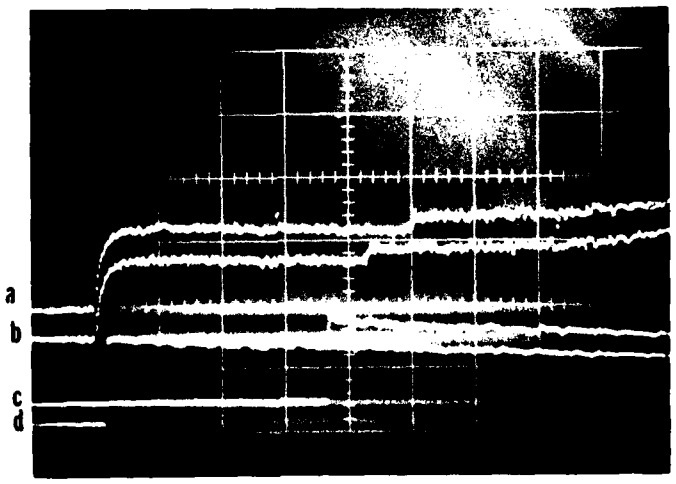

shock-wave boundary layer measurements.

Figure 42 P_o = 99 mm Hg, T_o = 23.4°C, X_s = 7.5 ft, M_s = 1.43.
(a) FHFA at corner .1 volt/cm, .5 msec/cm, R_o = 11.12Ω, a = .3.
(b) FHFA at center .1 volt/cm, .5 msec/cm, R_o = 13.1Ω, a = .3.
(c) 4 psi/cm, .5 msec/cm, X_s = 10.58 ft. (d) 4 psi/cm, .5 msec/cm, X_s = 7.63 ft.

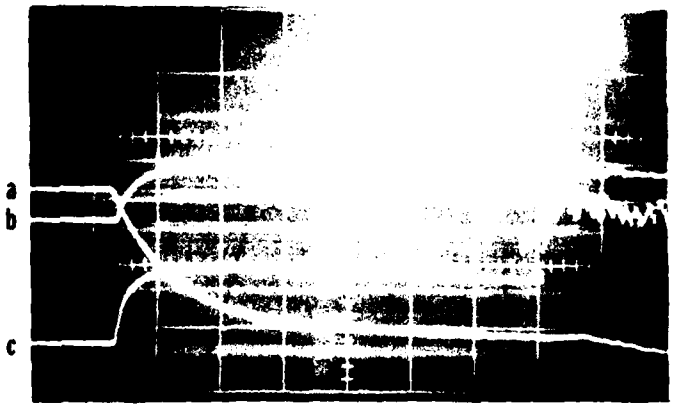

Figure 43 Oscilloscope record for expansion-wave boundary-layer measurements.

P_o = 45 psia, X_s = 4.6 ft. (a) 10 psi/cm, 2 msec/cm; (b) HWA at y = .035 in, 5.0 volt/cm, 2 msec/cm, R_o = 6.95Ω, a = .5; (c) FHFA at center .5 volt/cm, 2 msec/cm, R_o = 13.1Ω, a = .5.

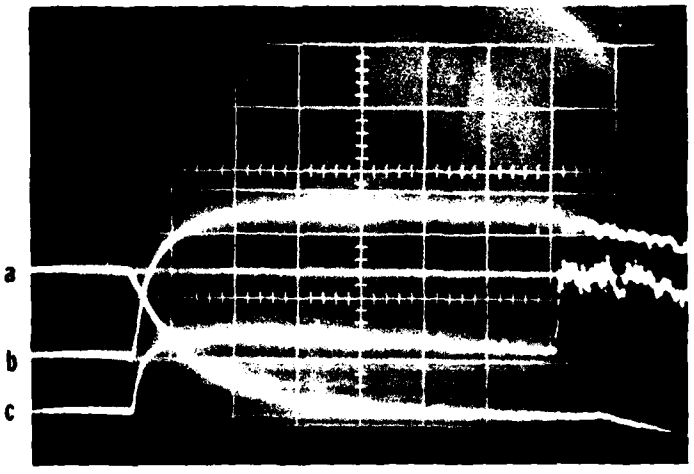

Figure 44 Oscilloscope record for expansion-wave boundary-layer measurements.

P_o = 45 psia, X_s = 4.6 ft. (a) 10 psi/cm, 2 msec/cm; (b) HWA at y = .022 in, 2.0 volt/cm, 2.0 msec/cm, R_o = 6.95Ω, a = .5; (c) FHFA at center .5 volt/cm, 2.0 msec/cm, R_o = 13.1Ω, a = .5.

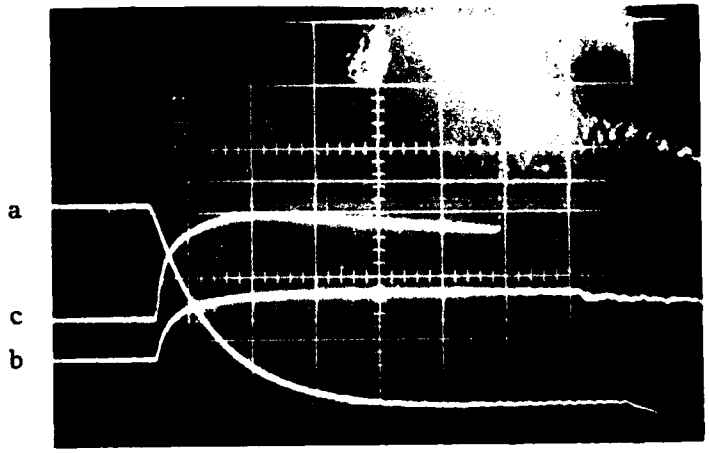

Figure 45 Oscilloscope record for expansion-wave boundary-layer measurements.

P_o = 65 psia, X_s = 4.6 ft. (a) 10 psi/cm, 2 msec/cm; (b) HWA at y = .035 in, 5.0 volt/cm, 2 msec/cm, R_o = 6.95Ω, a = .5; (c) FHFA at center .5 volt/cm, 2 msec/cm, R_o = 13.1Ω, a = .5.

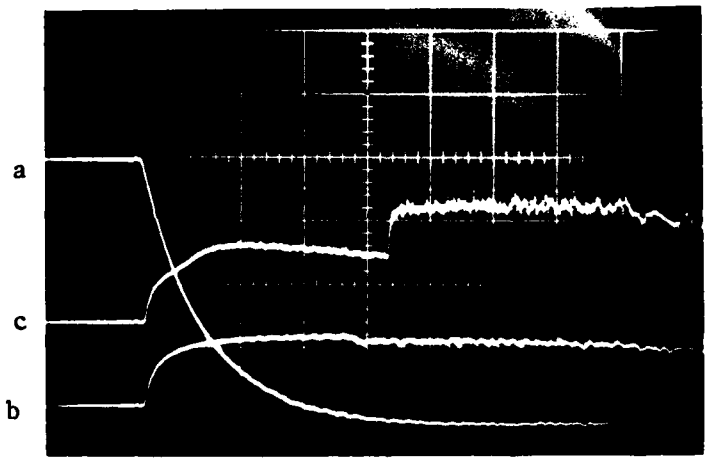

Figure 46 Oscilloscope record for expansion-wave boundary-layer measurements.

P_o = 85 psia, X_s = 4.6 ft. (a) 10 psi/cm, 2 msec/cm; (b) HWA at y = .035 in, 5 volt/cm, 2 msec/cm, R_o = 6.95Ω, a = .5; (c) FHFA at center 1.0 volt/cm, 1 msec/cm, R_o = 13.1Ω, a = .5.

Figure 47 Oscilloscope record for expansion-wave boundary-layer measurements.

P_o = 85 psia, X_s = 4.6 ft. (a) 10 psi/cm, 2 msec/cm; (b) HWA at y = .022 in, 2.0 volt/cm, 2 msec/cm, R_o = 6.95Ω, a = .5; (c) FHFA at center 1.0 volt/cm, 2 msec/cm, R_o = 13.1Ω, a = .5.

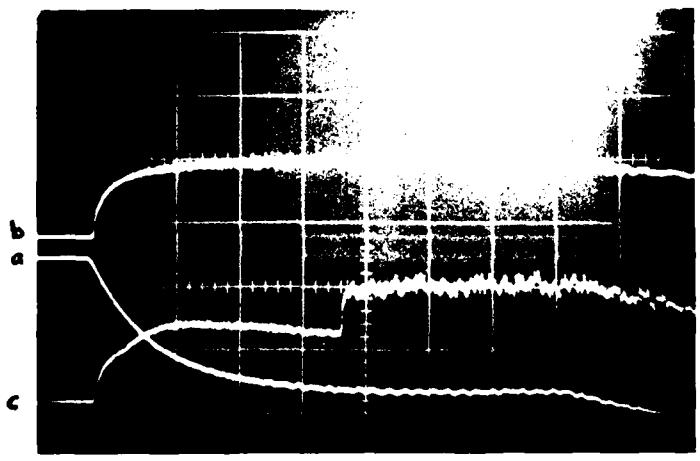

Figure 48: Oscilloscope record for expansion-wave boundary-layer measurements.

P_o = 85 psia, X_s = 4.5 ft. (a) 20 psi/cm, 2 msec/cm; (b) HWA at y = .25 in, 5 volt/cm, 2 msec/cm, R_o = 3.93Ω, a = .5; (c) FHFA at center .5 volt/cm, 2 msec/cm, R_o = 13.1Ω, a = .5.

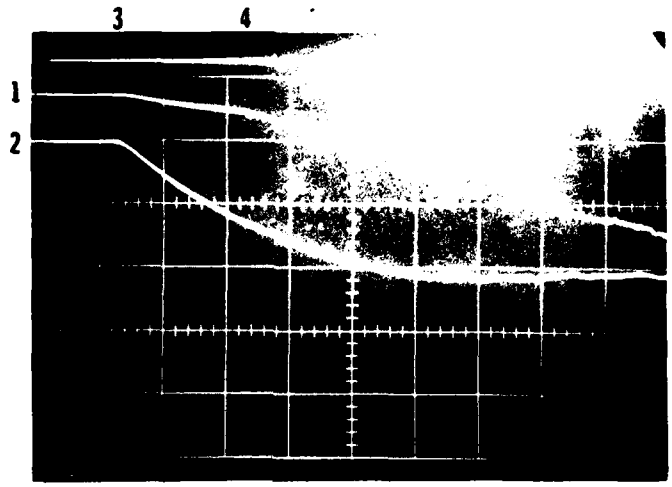

(1) Voltage output of surface thin film thermometer at 7 ft station. 2 mvolt/cm ↑, 1 msec/cm, → R_F = 1336.1 r. Initial film voltage (E_F) = 8.016 volts, α = 6.423 x 10^{-4} 1°C.

(2) Wall pressure transducer output at 7 ft station. 10 psi/cm ↑, 1 msec/cm →.

(3) Wavehead arrival at 7 ft station.

(4) Beginning of boundary layer transition at 7 ft station.

Figure 49: Typical oscilloscope record of thin film resistance thermometer output and pressure transducer output. Dry air with P_o = 55 psia, T_o = 73.4°F.

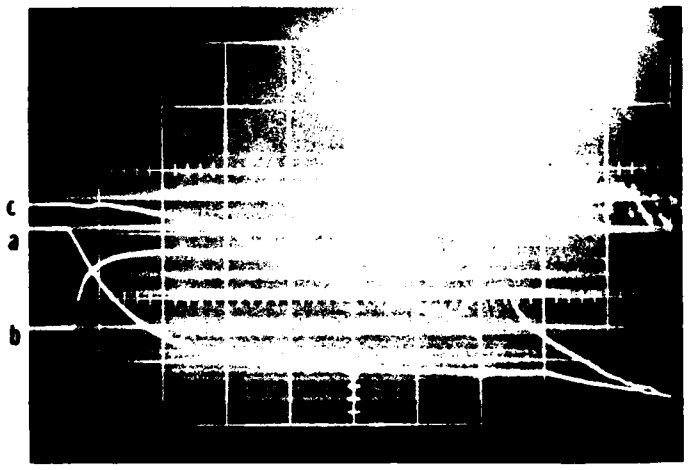

Figure 50 Oscilloscope record for expansion-wave boundary-layer measurements.

P_o = 45 psia, X_s = 4.6 ft. (a) 10 psi/cm, 2 msec/cm; (b) FHFA plate center .5 volt/cm, 2 msec/cm, R_o = 13.1Ω, a = .5; (c) thin film thermometer, channel wall, R_f = 624.4Ω, E_f = 4.995 volts, 2.0 MV/cm, 2.0 msec/cm, $\alpha = 8.72 \times 10^{-4}/°C$.

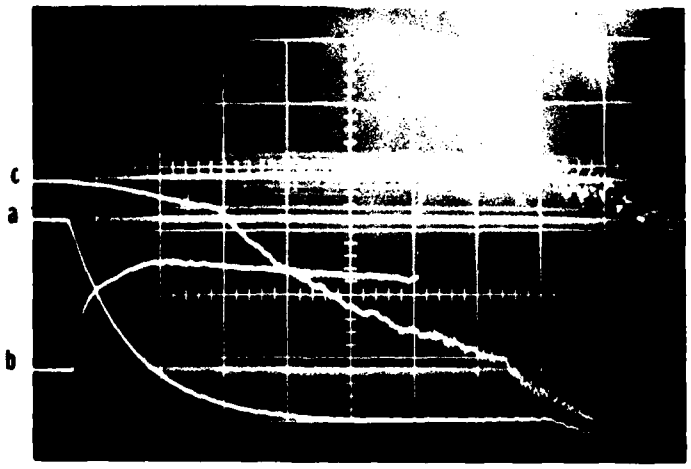

Figure 51 P_o = 65 psia, X_s = 4.6 ft. (a) 10 psi/cm, 2 msec/cm; (b) FHFA plate center .5 volt/cm, 2 msec/cm, R_o = 13.1Ω, a = .5; (c) thin film thermometer, channel wall, R_f = 622.4Ω, E_f = 4.99 volts, 2.0 MV/cm, 2.0 msec/cm, $\alpha = 8.72 \times 10^{-4}/°C$.

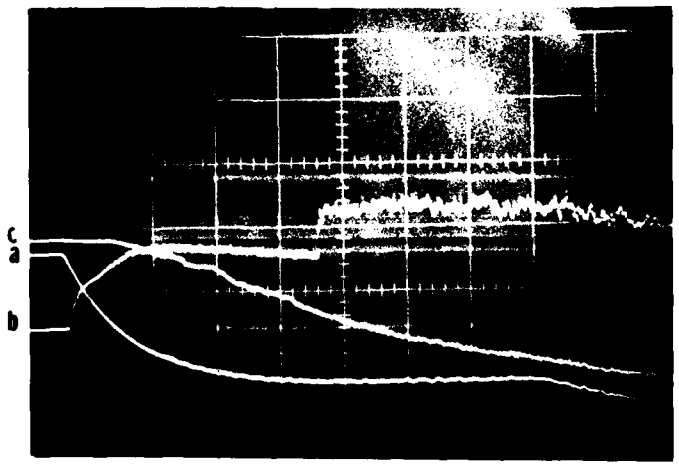

Figure 52 Oscilloscope record for expansion-wave boundary-layer measurements.

P_o = 85 psia, X_s = 4.6 ft. (a) 20 psi/cm, 2 msec/cm; (b) FHFA at plate center 1.0 volt/cm, 2 msec/cm, R_o = 13.1Ω, a = .5; (c) thin film thermometer, channel wall, R_f = 622.5Ω, E_f = 4.99 volts, 5.0 MV/cm, 2.0 msec/cm, $\alpha = 8.72 \times 10^{-4}/°C$.

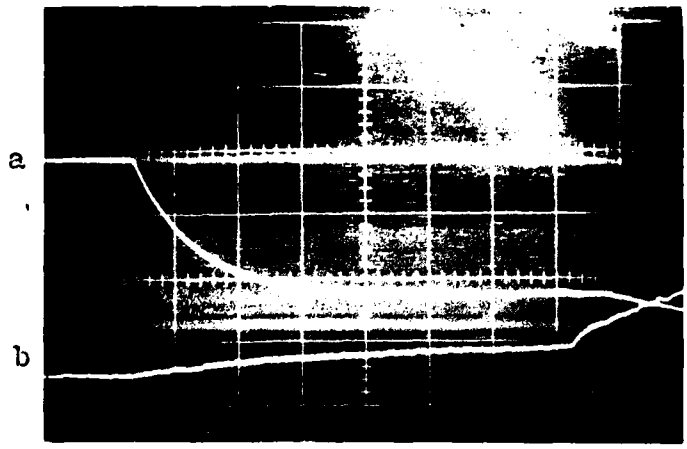

Figure 53. Expansion wave record. P_o = 45 psia, T_o = 23.5°C, x_s = 4.6 ft. (a) Pressure 10 psi/cm, 2 msec/cm. (b) Flush constant current anemometer, I = 3.35 milliamps, R_F = 15.34Ω, amplification A = 2300, .5 volts/cm, 2 msec/cm.

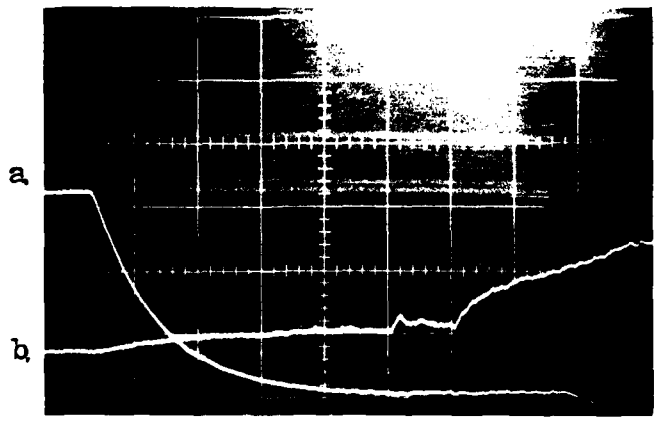

Figure 54 Expansion wave record. P_o = 65 psia, T_o = 23.5°C, x_s = 4.6 ft. (a) Pressure 10 psi/cm, 2 msec/cm. (b) Flush constant current anemometer, I = 3.35 milliamps, R_F = 15.34Ω, amplification A = 2300, .5 volts/cm, 2 msec/cm.

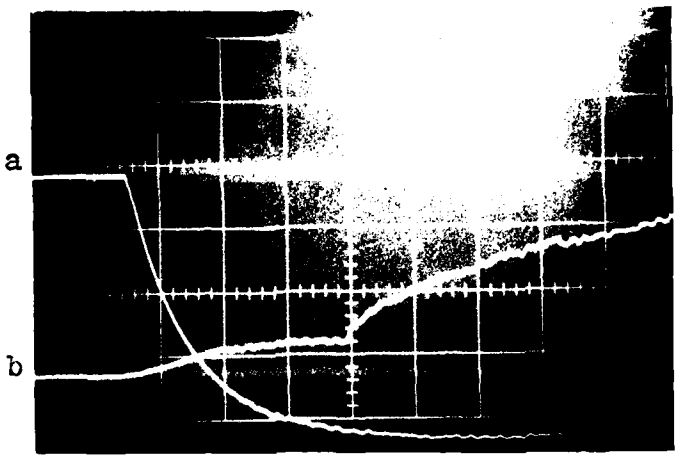

Figure 55 . Expansion wave record. P_o = 85 psia, T_o = 23.4°C, x_s = 4.6 ft. (a) Pressure 10 psi/cm, 2 msec/cm. (b) Flush constant current anemometer, I = 3.35 milliamps, R_F = 15.34Ω, amplification A = 2300, .5 volts/cm, 2 msec/cm.

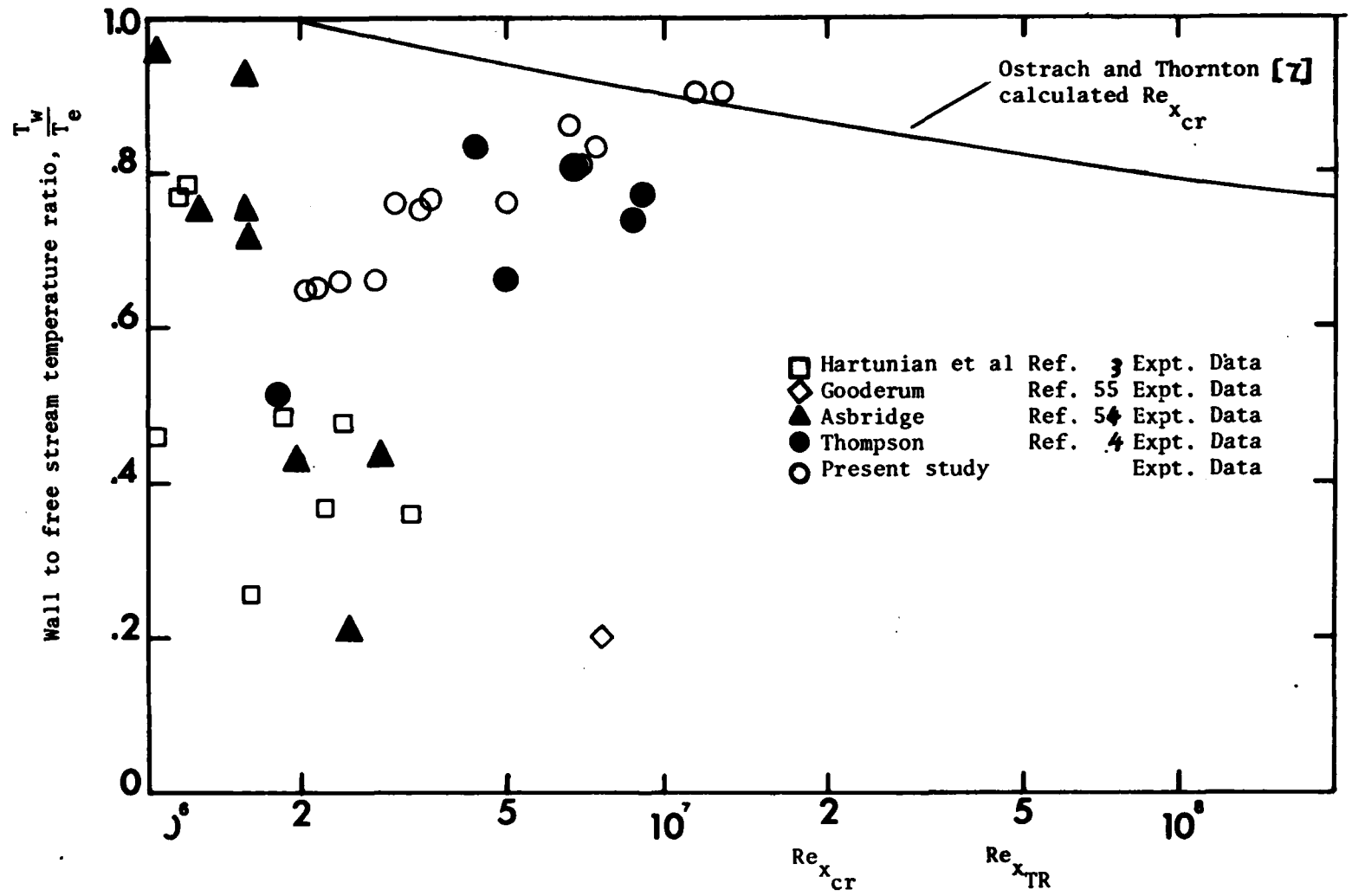

Figure 56 Comparison of local minimum critical and observed transition Reynolds numbers based on distance from the shock-wave.

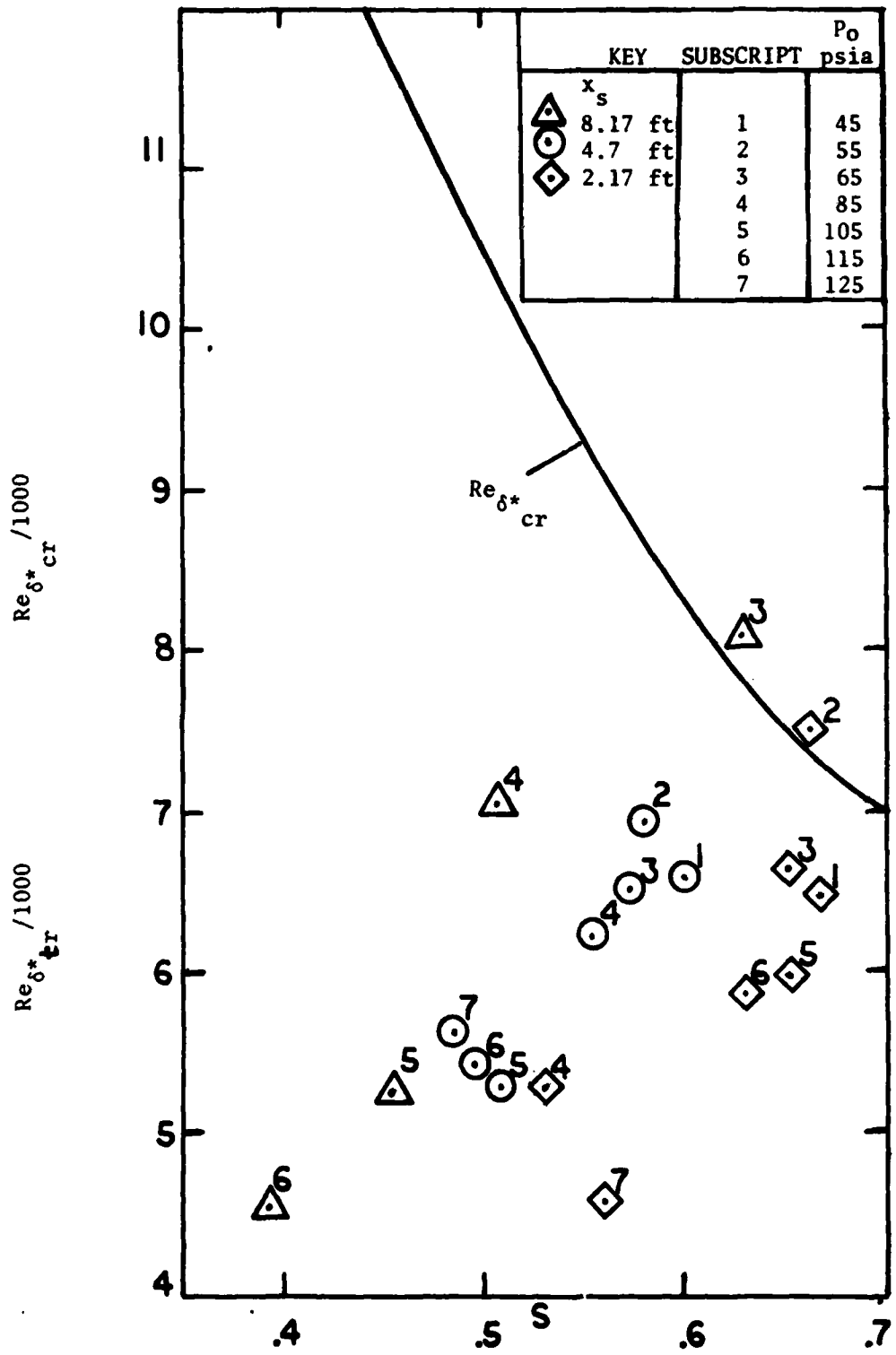

Figure 57: Comparison of observed transition Reynolds number from present experiment and calculated critical Reynolds number (Eq. 3.14) for the expansion-wave boundary-layer.

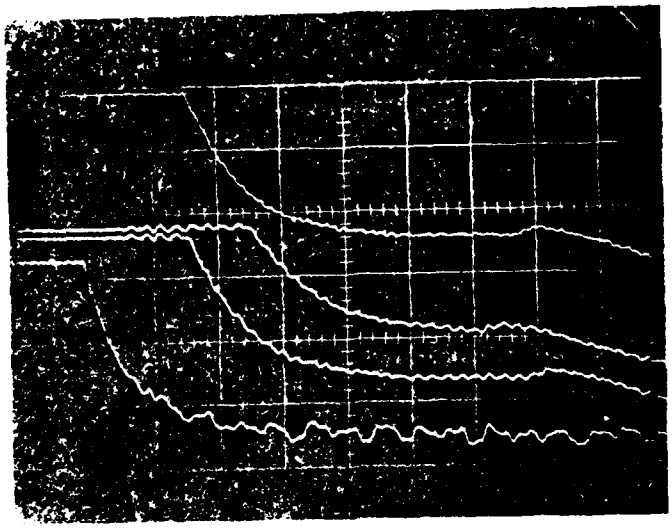

Figure 58 Oscilloscope record for expansion-wave boundary layer measurements. Fluctuations in static pressure. P_o = 125 psia. (a) P at X_s = 6.75 ft, 20 psi/cm, 2 msec/cm, 10 KHz upper frequency filter; (b) P at X_s = 9 ft; (c) P at X_s = 6.75 ft; (d) P at 3 ft. No filter on b, c and d.

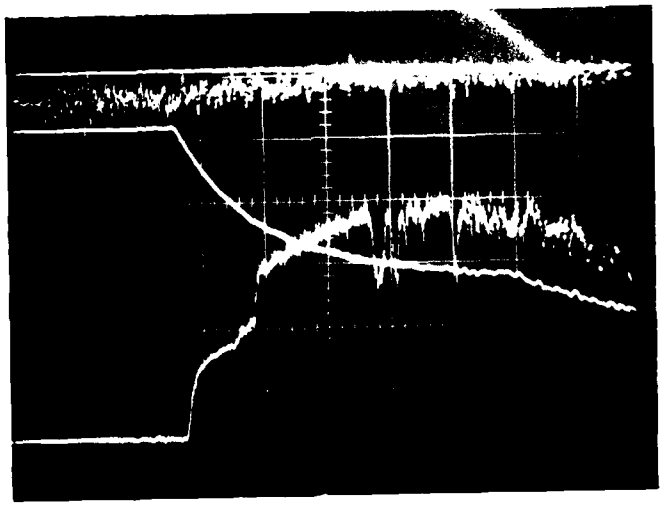

Figure 59 Oscilloscope record for expansion-wave boundary layer measurements. (a) Accelerometer output 2 g/cm, 2 msec/cm; (b) Pressure, 20 psi/cm, 2 msec/cm; (c) FHFA R_o = 16.2Ω, .5 volt/cm, 2.0 msec/cm, a = .5, Hf = 3, G = 6. X_s = 7 ft.

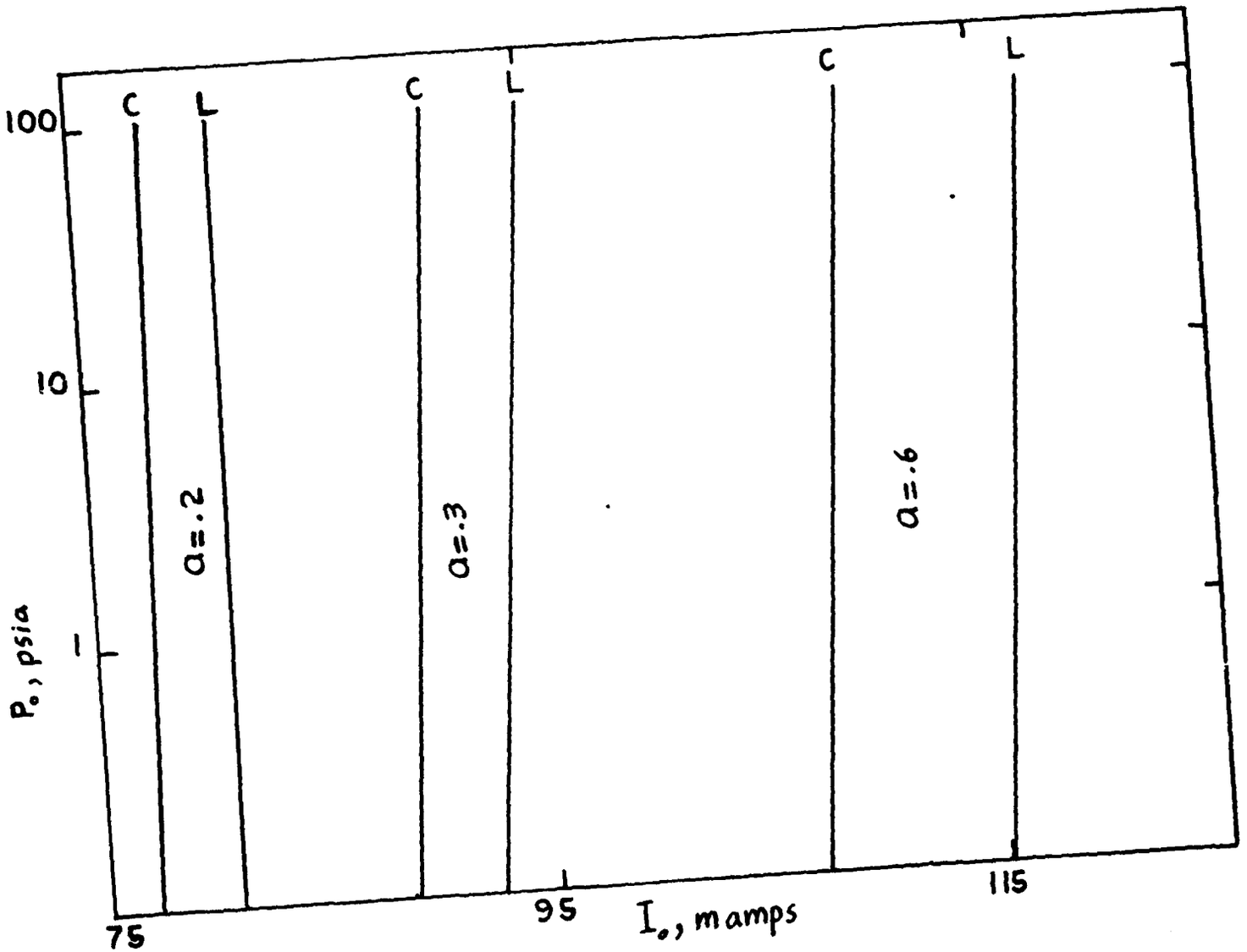

Figure 60: FHFA probe current levels for overheat ratios a = .2, .3 and .6 and varying pressure. L (R = 13.26Ω), C (R = 11.28Ω).

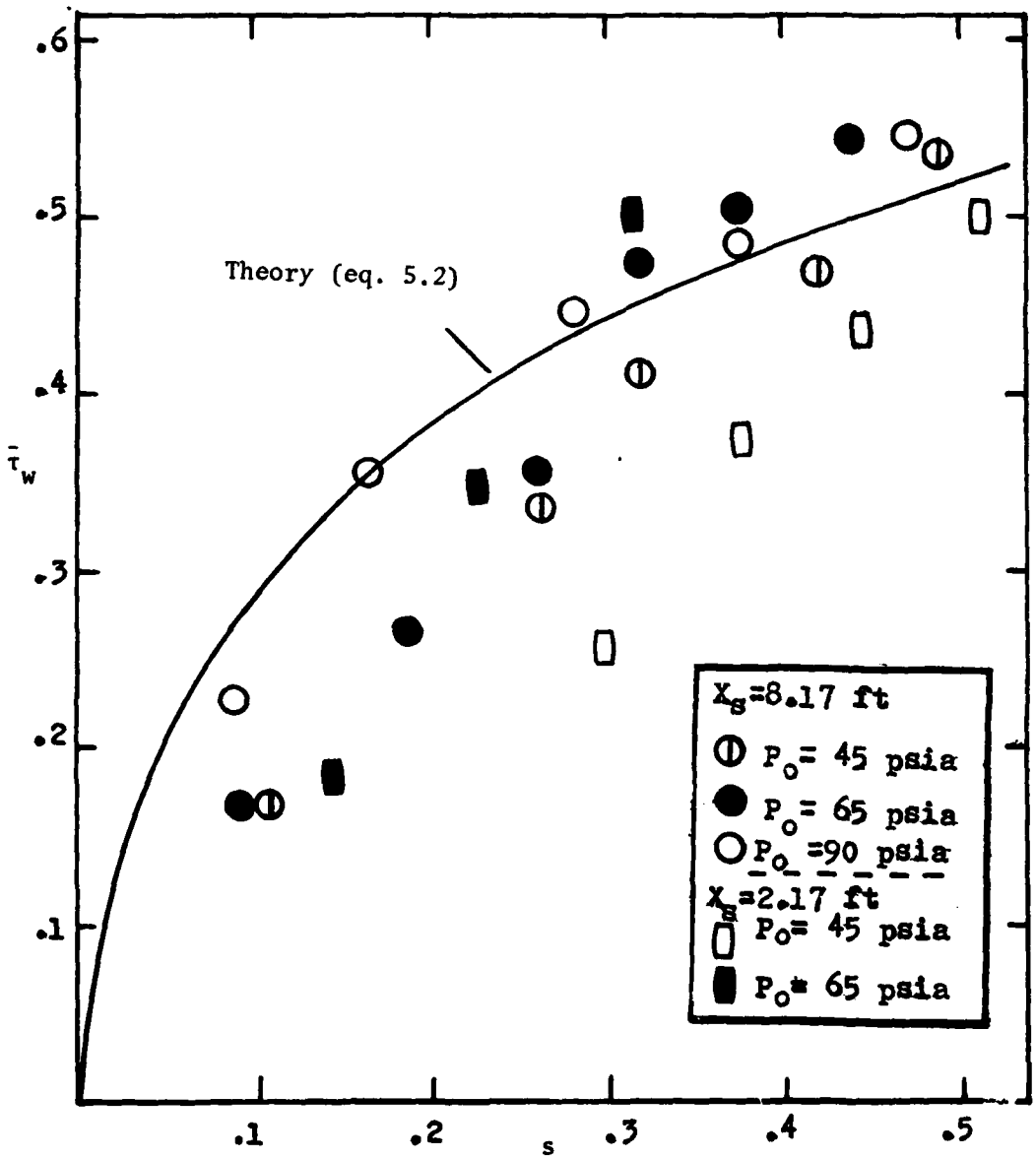

Figure 61 Comparison of experimental and theoretical skin friction for the expansion-wave boundary layer. L = .7L*.

APPENDIX A

THE COMPUTER PROGRAM FOR SOLUTION OF THE ORR-SOMMERFELD EQUATION

A.1 Program Description

A computer program was developed to solve for the eigenvalues of the Orr-Sommerfeld equation for boundary layer flows. The program consisted of a main program (STABIL) and eight subroutines written in Fortran IV. The iterations to find the eigenvalues were performed by an optimization routine developed by K. Afimiwala* [52].

Program STABIL

The main program STABIL initialized the inputs for the optimization subroutine CONGRA which searched for the desired eigenvalues X(1) and X(2). X(1) and X(2) were chosen as k_r and ω_r or k_r and k_i or any other desired eigenvalues. Also required for the use of subroutine CONGRA were the initial step size for the search (TT), the maximum step size for the search (TMAX), the accuracy criteria (ACC), and the maximum number of iterations (LIM) performed to satisfy the accuracy criteria.

The eigenvalues were found utilizing the orthonormalization** techniques described in Sec. A.2 by setting SKIPY $\leq$ 1 and YA = 0. Once the eigenvalues were found STABIL set SKIPY = 2 (orthonormalization skipped) and called function subroutine F(X) to evaluate the complex constant YA

---

*The optimization routines were provided by Dr. Roger W. Mayne and their use is greatly appreciated.

**The use of these methods was the result of a conversation with Dr. Stephen Davis whose help is much appreciated.

($\phi = \phi_1 + YA\ \phi_2$). Finally, STABIL called F(X) again (SKIPY = 2, YA $\neq$ 0) and subroutine OUTP evaluated and printed the eigenfunctions ($\phi, \phi', \phi'', \phi'''$) without orthonormalizing. An attempt was also made to evaluate the eigenfunctions using the orthogonalization technique but the required subroutine did not perform as desired. For the large Reynolds numbers ($Re_{\delta^*} > 2{,}000$) the eigenfunctions must also be evaluated using orthonormalization.

Function F(X)

Function subroutine F(X) was used by the optimization package to evaluate $F(X) = \phi(\eta=0)$ which was a test of whether or not the boundary conditions were satisfied at the wall. F(X) was also called by STABIL to evaluate the constant YA and the eigenfunctions.

For eigenvalue evaluations F(X) was computed by integration of the Orr-Sommerfeld equation using the method of orthonormalization as described in Sec. A.2. Orthonormalizations were performed NBLOCK+1 times, once at the start and at the end of each block. Each integration was performed over a block size $STP = \frac{\eta_{max}}{NBLOCK}$. The integration was performed in complex variables and using a single precision predictor-corrector subroutine CHPCG* in equal steps $\Delta\eta$ = PRMT(4).

Subroutine NORMAL

Normalized the eigenvalue solution vectors so that $X1 = \bar{\phi}_1 = (\phi_1, \phi_1', \phi_1'', \phi_1''') = (y(1), y(2), y(3), y(4))$ became

$$X1N = \frac{X1}{|X1|}$$

*Modified version of double precision subroutine DHPCG. DHPCG was obtained from Dr. Joseph C. Mollendorf and its use is greatly appreciated.

and: $X2 = \bar{\phi}_2 = (\phi_2, \phi_2', \phi_2'', \phi_2''') = (y(5), y(6), y(7), y(8))$ became

$$X2N = \frac{X2}{|X2|}$$

Subroutine INNER

This computes the inner product of the two complex vectors X1 and X2, ($|X1| = \sqrt{X1.X1}$).

Subroutine SCHMIDT

The Gram-Schmidt method was used to modify normalized solution vector X2N so that it was orthogonal to the normalized solution vector X1N. The modified vector X3 was derived as follows:

$$X3 = X2N - \left[\frac{X1N.X2N}{X1N.X1N}\right]X1N$$

so that

$$X1N.X3 = 0$$

At the end of each block X1 was set equal to X1N and X2 was set equal to X3.

Subroutine CHPCG

CHPCG performed the integration for each block from η = PRMT(1) to η = PRMT(2) = (PRMT(1) - STP) in equal steps $\Delta\eta$ = PRMT(3) = $\frac{1}{2^n}$. CHPCG had the capability of subdividing the initial step size PRMT(3) if the accuracy criteria was not satisfied. To insure that this does not happen the accuracy parameter PRMT(4) was set very large ($> 10^{20}$).

Subroutine FCT

FCT was called by CHPCG to evaluate the first order differential equations for the Orr-Sommerfeld equation and the mean flow if required. For the expansion-wave boundary layer, the mean flow solution was already known (Eq. 2.19).

Subroutine OUTP

OUTP is an output subroutine which printed and evaluated the eigenfunctions if SKIPY > 1.5 and YA $\neq$ 0.

A.2 Operation of Integration Function Subroutine (F(X))

F(X) integrated the Orr-Sommerfeld equation from η_{max} to the wall for a given Reynolds number and eigenvalues. For neutral stability calculations, eigenvalues k_i and ω_i were set to zero, and k_r' and ω_r' were set to $X(1)/\eta_{\delta_R}$ and $X(2)/\eta_{\delta_R}$ respectively. Re_{δ_R} is also modified to $Re' = \frac{Re_{\delta_R}}{\eta_{\delta_R}}$ where η_δ is the value of η at $y = \delta_R$. For the Blasius boundary layer, δ_R is taken as the displacement thickness so that $\eta_{\delta_R} = 1.7208$. For the expansion wave δ_R is taken as the momentum thickness and $\eta_{\delta_R} = .3479$. The length used to yield the non-dimensionalized quantities k_r', ω_r' and Re' became y at $\eta = 1$ which was used because the mean flow velocity profile U was derived in terms of the similarity parameter η ($U = U(\eta)$). The momentum thickness θ for the expansion wave boundary layer was obtained from a numerical integration of the velocity profiles Eq. (2.19) given by Srinivasan [5]. A trapezoidal rule method of integration was used for 600 even steps from $\eta = 0$ to $\eta = 6$.

Integration was started at a sufficiently large y_∞ (or η_∞) such that

the inviscid form of the Orr-Sommerfeld equation applies and there was no change in the resulting eigenvalues. Typically integration was started at y such that $\frac{U}{U_\infty} > .999$ for the expansion wave boundary layer flow. This corresponds to $\eta \geq 4.0$. Integration was started at $\eta_{max} = 6.0$ so that $\frac{U}{U_\infty} = 1.0000$ and $\frac{d^2}{d\eta^2}(\frac{U}{U_\infty}) = -.00005$. The asymptotic solution to the Orr-Sommerfeld equation was then given by

$$\phi_1 = e^{-k'\eta_{max}}$$

and

$$\phi_2 = e^{-\sqrt{k'^2+Re'(k'-\omega')}\ \eta_{max}}$$

For the expansion wave boundary layer, ϕ_2 was found to be so small ($< e^{-300}$) that truncation error would occur from any mathematical operation where ϕ_2 is multiplied by itself or one of its derivatives (e.g., $\phi_2^2 = 0$). To avoid this, ϕ_2 was multiplied by a constant greater than e^{200}.

Prior to integration the solution vectors $X1 = (\phi_1, \phi_1', \phi_1'', \phi_1''')$ and $X2 = (\phi_2, \phi_2', \phi_2'', \phi_2''')$ were normalized (each vector becomes of unit length) and a precautionary correction made to X2 to insure it was orthogonal to X1 as described in Sec. A.1. The integration was then performed by subroutine CHPCG in even steps Δh = PRMT(3). The truncation error in CHPCG was proportional to Δh^5. A choice of a too large Δh would result in a rapid deterioration of the linear independence of the two solution vectors beyond the restoration capability of the orthogonalization scheme. A choice of too small a Δh would increase the number of mathematical operations and enhance error propagation. Δh was chosen as $1/2^n$ as recommended by Betchov and Crimminale [26] because the computer

performs the computations in a binary mode and this choice of step size would cut down on the resulting truncation error. The choice of n is dependent on the product k'Re' (Ref. 53). For $Re_\theta \simeq 12{,}000$ a choice of n = 6 was found to yield fourth place accuracy of eigenvalues as compared to n = 7 (with NBLOCK+1 = 25 orthonormalizations as discussed below). For $Re_\theta > 14{,}000$ a step size of $1/2^7$ was used for eigenvalue computations.

Due to computer truncation error, the solution vectors do not remain linearly independent and their inner product deviated from zero. The integration was stopped at the end of equal distances $STP = \frac{\eta_{max}}{NBLOCK}$ and the solution vectors were orthonormalized. Some investigators (e.g., Ref. 53) stop the integration after each step or a number of steps and check on the orthogonality of the two solution vectors. If the angle between the two vectors is not within a desired range, then an orthonormalization is performed. A check on orthogonality at the end of each step would be more time consuming. If a sufficient number of orthonormalizations are chosen, then the same results can sometimes be obtained using less computer time. The use of too many unnecessary orthonormalizations could also produce some computational errors as suggested by Davey [39].

The choice of an appropriate step size depends on the number of orthonormalizations used. A larger step size might be used with a smaller number of orthogonalizations. There is a minimum number of orthonormalizations, however, that should be used with each choice of Δh and Re_θ. The choice of NBLOCK was somewhat arbitrarily chosen as 24 since at the largest Reynolds number for the Blasius boundary layer NBLOCK = 6 gave good accuracy. Using this choice of NBLOCK, Δh was varied to give the desired fourth place accuracy for the eigenvalues. Following the final choice of Δh, NBLOCK was increased to 30 but this did not result in a

change of the fourth place decimal accuracy.

The evaluation of eigenfunctions using orthonormalizations required a transfer matrix to keep track of the changes made each time an orthonormalization was used. An attempt was made to write a subroutine for this purpose but was not successful. An evaluation was made of the eigenfunctions without orthonormalizing for the Blasius boundary layer with $Re_{\delta^*} = 998$, $k = .3086 = i\ .0057$ and $\omega = .112$, and integrating from $\frac{\eta_{max}}{\delta^*} = 3.4$ rather than 6 (used by Jordinson [27]). For ϕ_r the agreement was good with Jordinson's results. However, $\phi_i << \phi_r$ so that the relative error for ϕ_i was much more significant, especially for large distances from the wall ($\eta/\delta^* > 1.2$). For larger Reynolds numbers, the orthogonalization scheme becomes increasingly important for accurate eigenvalue and eigenfunction evaluations [39].

The computation time for the eigenfunction evaluation and each iteration was typically about 2 seconds. The total number of iterations required to find the eigenvalues depends on the initial guess. To obtain good initial gueses, a matrix search was performed for the smallest F(X) in equal increments of k and ω and the best guess(es) were tried in the optimization routine. The correct eigenvalues were those giving the smallest value of $F(X) = \phi$ at the wall. The final search for the eigenvalue involved as many as fifty iterations and took approximately 100 to 150 seconds. This, however, did not include the time consumed for the numerous other starting gueses. The actual total time involved in finding one point on the neutral stability curve of the expansion wave boundary layer was about 500-1000 seconds. The large computation time needed was due to the lack of previously published eigenvalue results for this type of flow that could be used as a starting point of the search.

A.3 Program Listing

```
PROGRAM STABIL      73/173  OPT=0 TRACE MANTRAP              FTN 4.7+476          79/0

      PROGRAM STABIL(INPUT,OUTPUT,TAPE5=INPUT,TAPE6=OUTPUT)
      DIMENSION X(6),PRMT(5)
      COMPLEX CE,AE,AA,A4    ,PH,DPH,YA
      COMMON/ALWAYS/TMAX,METHOD,KFEAS,LIM,NC,NI,IOUT,NPERT
      COMMON/STAB1/NORDER,NBLOCK,L1,L2,R,CE,PRMT,NDIM,AE,AA,A4
      COMMON /GO/PH,DPH,YA ,SKIPY
C     INITIALIZATION
C
C     COMMON BLOCK ALWAYS CONTAINS PARAMETERS USED IN OPTIMIZATION PACKAGE
C     - OF KUSCHID AFIMAWALI  OBTAINED FROM DR MAYNE  COULD ALSO USE ROOT
C     - FINDING SCHEME ZANLYT ON IBM PACKAGE WITH SLIGHT MODIFICATION.
C
C      X  IS VECTOR CONTAINING EIGENVALUES TO BE COMPUTED OR TO BE USED IN
C     - EVALUATION OF EIGEN FUNCTIONS.. INITIAL GUESS MUST BE PRETTY CLOSE
C
C      SET YA=1.0  TO FIND CORRECT VALUE OF YA USED TO EVALUATE THE
C     EIGENFUNCTIONS IN SUBROUTINE OUTP AND AG IN FUNCT(X,F)
C
C     YA  IS FACTOR BY WHICH  Q2 MUST BE MULTIPLIED TO SATISFY OSE B.C AT
C     - AT THE WALL( DQ/DX=0.0).. F=DET=0 AT THE WALL  =0 IF THE SECON B.C
C      AT THE WALL IS ALSO SATISFIED
C
C     EIGENVALUES ITERATION VIA OPTIMIZATION.
C     SKIPY=1.0 OR LESS TO FIND EIGENVALUES ONLY NOT EIGENFUNCTIONS
C      SKIPY=1.55 OR MORE EVALUATES EIGENFUNCTION
```

THIS PAGE IS BEST QUALITY PRACTICABLE
FROM COPY FURNISHED TO DDC

```
      NN=2  $ NC=NI=0  $ MINIM=2  $ TT=.1E-4
      TT=.1E-3
      IGRAD=1 $ NORDER=4 $ METHOD=3 $ ACC=.1E-4 $ SKIPY=1.0 $ YA=0.0
      TMAX=.01  $ KFEAS=1  $ NPERT=1  $ LIM=15  $ IOUT=1
      R=12000. $ X(1)=.18875  $ X(2)=.0367
C
      YA=0.0  $ SKIPY=1.0
      ACC=.1E-5
      CALL FUNCT(X,F)
      WRITE(6,14) X(1),X(2),F,R
      CALL CONGRA(MINIM,X,TT,NN,ACC,F,FF,IGRAD)
      WRITE(6,15)  AE
      ACC=.1E-6
   15 FORMAT(/,/,* YA= *,2E15.8,/)
   14 FORMAT(5X,*REAL ALFA=*,E16.9,5X,*REAL EIGENBE=*,E16.9,5X,*DET=*,
     1E16.9,5X,*REYNOLDS NO.=*,E14.5)
      CALL EXIT  $  END
```

THIS PAGE IS BEST QUALITY PRACTICABLE
FROM COPY FURNISHED TO DDC

```
      SUBROUTINE FUNCT(X,F)
      DIMENSION X(4),Y(11),DERY(11),PRMT(5),AUX(16,16),X1(4),X2(4),X3(4)
      COMPLEX Y,DERY,AUX,X1,X2,X3,CE,DET,AE,AA,A4,G,AE2,BE,S1,S2
      COMMON/STAB1/NORDER,NBLOCK,L1,L2,R,CE,PRMT,NDIM,AE,AA,A4
      COMMON/STAB2/K3,MORDER
      COMMON/STAB3/I8
      COMPLEX PH,DPH,YA
      COMPLEX S12,S22
      COMMON /GO/PH,DPH,YA ,SKIPY
C
C      Y  COMPLEX VECTOR OF EIGENFUNCTIONS  G1=1 TO4,G2=5 TO8,VEL=9TO11
C      Y SOMETIMES.     FCOREC IS A SCALE FACTOR USED  WHICH DEPENDS ON
C     WHETHER DISPLACEMENT OR MOMENTUM THECKNESS IS USED TO DEFINE R,ALFA AND
C      BETTA OF MAIN PROGRAM STABIL FACTOR=1.7208 FOR BLASIUS    OR AS
C     COMPUTED IN SHAPE PARANETER CALCULATIONS AND SO HERE DEFINED..
C      NBLOCK IS THE NUMBER OF ORTHOGONALIZATIONS USED OR NUMBER OF LOCATIONS
C      AT WHICH ORTHOGONALITY IS CHECKED FOR.
C      PRMT(1)=STARTING POINT OF INTEGRATION , PRMT(2)=ENDING POINT
C     PRMT(3)= INITIAL STEP SIZE SUGGESTED, PRMT(4)=PARAMETER DETERMINING
C     WHETHER TO SUBDIVIDE STEP SIZE OR NOT IF VERY LARGE THEN NOT
C      X1 X2 COMPLEX UNIT VECTORS USED TO FIND THE ORTHONORMAL VECTOR X3
C     X1 AND X3  ARE USED IN INTEGRATION OF CSE  ....
C
C     BO MATRIX CONTAINING FACTORS BY WHICH THE EIGENVALUES ARE CHANGED EACH TIN
C      TIME AN ORTHOGNALIZATION IS USED TO START INTEGRATION OF NEXT BLOCK.
      EXTERNAL FCT,OUTP
       NORDER=MORDER=4
      ISWITCH=I8=0
      ISIGNAL=0
      FCOREC=.2479
```


THIS PAGE IS BEST QUALITY PRACTICABLE
FROM COPY FURNISHED TO DDC

```
      AR=X(1)/FCOREC  $ AI=0.0  $ BR=X(2)/FCOREC  $ BI=0.0
      AE=CMPLX(AR,AI) $ BE=CMPLX(BR,BI) $  CE=BE/AE
      R=R/FCOREC
                                AA=AE*AE  $ A4=AA*AA  $ K3=0
C  GATE  1 I N I T I A L I Z A T I O N
      NBLOCK=24.0  $ STP=-.25
      XS=-NBLOCK*STP
      AE2=CMPLX(0.0,R)
      AE2=AA+AE2*(AE-BE)
      AE2=CSQRT(AE2)
      S1=XS*AE  $ S2=XS*AE2   $ S1=-S1  $  S2=-S2
      S12=S1        $ S22=S2+150.
      Y(1)=CEXP(S1)  $ Y(5)=CEXP(S2)
      Y(1)=CEXP(S12)  $ Y(5)=CEXP(S22)
      DO1 I=2,4
      I1=I-1  $ J2=I+4  $ J1=I+3
      Y(I)=-AE*Y(I1)  $ Y(J2)=-AE2*Y(J1)
 1    CONTINUE
C    GATE 2  I N T E G R A T I O N
      K1=1
      PRMT(2)=XS
      DO 6 K1=1,NBLOCK
      IWHY=K1
       IF(IWHY.EQ.1) GOTO8
 7    CONTINUE
      PRMT(1)=XS+(K1-1)*STP
      PRMT(2)=PRMT(1)+STP
```

THIS PAGE IS BEST QUALITY PRACTICABLE
FROM COPY FURNISHED TO DDC

```
      PRMT(3)=-.015625
      PRMT(4)=.1E30
      IHLF=0
      NDIM=11
      NDIM=8
      DO2 I=1,11
    2  DERY(I)=1.0/NDIM
      CALL CHECG(PRMT,Y,DERY,NDIM,IHLF)
    8  CONTINUE
      IF(SKIPY.GT.1.0) GOTO51
      DO 3 I=1,4
      J=I+4
      X1(I)=Y(I)  $  X2(I)=Y(J)
    3 CONTINUE
C   GATE 3  GRHAM  S C H M I D T I N G
      CALL NORMAL(NORDER,X1,X3)
      DO4  I=1,4
    4 X1(I)=X3(I)
      CALL NORMAL(NORDER,X2,X3)
      DO 40 IY=1,4
   40 X2(IY)=X3(IY)
      CALL SCHMIDT(NORDER,X1,X2,X3)
      DO 5 I=1,4
      I5=4+I
      X2(I)=X3(I)
      Y(I)=X1(I)  $  Y(I5)=X2(I)
    5  CONTINUE
   51 IF(IWHY.GT.0) IWHY=IWHY+1
      IF(IWHY.EQ.2)  GOTO7
    6  CONTINUE
      DET=Y(1)-Y(2)*Y(5)/Y(6)
      DETR=REAL(DET)  $   DETI=AIMAG(DET)
      F=ABS(DETR) + ABS(DETI)
      R=F*FCORRC
      AE=-Y(2)/Y(6)
      RETURN
      END
```

THIS PAGE IS BEST QUALITY PRACTICABLE
FROM COPY FURNISHED TO DDC

```
      SUBROUTINE OUTP(X,Y,DERY,IHLF,NDIM,PRMT)
      COMPLEX Y,DERY
      DIMENSION Y(11),DERY(11),PRMT(5)
      COMMON/STAB2/K3,MORDER
      COMMON /GO/PH,DPH,YA,SKIPY
      COMPLEX UVEL,D2UVEL
      COMMON/YRIP/UVEL,D2UVEL
      COMPLEX PH,DPH ,YA
      IF(SKIPY.LT.1.5) GOTO 2
    3 YA=  YA                    $ PH=Y(1)+YA*Y(5) $ DPH=Y(2)+YA*Y(6)
      W=X/.3479
      WRITE(6,14)W,PH,DPH
   15 FORMAT(*  GOT TO THE WALL*, 5E14.6)
   14 FORMAT(*ZZ=*,E14.8,*PHREAL=*,E14.8, *PHCOMPLX=*,E14.7,
     1*  DPHREAL=*,E14.7,* DPHCMPLEX=*,E14.7)
    1 FORMAT(2X,F8.5,8E14.6)
    2 K3=K3+1  $  RETURN  $  END
      SUBROUTINE FCT(X,Y,DERY)
      COMMON/YRIP/UVEL,D2UVEL
      DIMENSION Y(11),DERY(11),PRMT(5)
      COMPLEX Y,DERY,STOR,CE,AE,AA,A4
      COMMON/STAB1/NORDER,NBLOCK,L1,L2,R,CE,PRMT,NDIM,AE,AA,A4
      N=8
      J=N-1  $  DO 1 I=1,J  $  K=I+1
    1 DERY(I)=Y(K)  $  STOR=CMPLX(0.000000000000,R)
      YER=Y/2.0  $ YER2=YER*YER
      CALL MERF(YER,FER)
      PI=3.1415926535
      UVEL=1.0-(1.0+YER2*2.0)*(1.0-FER)+X/PI**.5/EXP(YER2)
      D2UVEL=FER-1.0
      STOR=STOR*AE
C     UVEL=MEAN VELOCITY       D2UVEL= SECOND DERIVATIVE OF UVEL
      DERY(8)=(2.0*AA+STOR*(UVEL-CE))*Y(7)-(A4+STOR*((UVEL-CE)*AA+D2UVEL
     1))*Y(5)
      DERY(4)=(2.0*AA+STOR*(UVEL-CE))*Y(3)-(A4+STOR*((UVEL-CE)*AA+D2UVEL
     1 ))*Y(1) $ RETURN  $END
```

THIS PAGE IS BEST QUALITY PRACTICABLE
FROM COPY FURNISHED TO DDC

SUBROUTINE MULTI 73/173 OPT=0 TRACE MANTRAP FTN 4.7+476 79/01/06. 14.28.5

```
      SUBROUTINE MULTI(L,M,N,A,B,C)
      DIMENSION A(L,M),B(M,N),C(L,N)
      COMPLEX A,B,C,SUM
C     M A T R I X  M U L T I P L I C A T I O N AXB
C     L=NUMBER OF ROWS OF A.
C     M=NUMBER OF COLUMNS OF A AND NUMBER OF ROWS OF B
C     N=NUMBER OF COLUMNS OF B.
C     A,B=INPUT MATRICES TO BE MULTIPLIED
C     C=OUTPUT MATRIX
      DO3 I=1,N
      DO2 K=1,L
      SUM=CMPLX(0.0000000000,0.0000000000  )
      DO1 J=1,M
    1 SUM=SUM+A(K,J)*B(J,I)
    2 C(K,I)=SUM
    3 CONTINUE
      RETURN
      END
```

SUBROUTINE NORMAL 73/173 OPT=0 TRACE MANTRAP FTN 4.7+476 79/01/06. 14.28.58

```
      SUBROUTINE NORMAL(N,A,AN)
      COMPLEX A,AN
      DIMENSION A(N),AN(N)
C     TO NORMALIZE AN ORDERED SET OF COMPLEX NUMBERS.
C     N=NUMBER OF ELEMENTS IN A.
C     AN=NORMALIZED A VECTOR.
C     A=INPUT VECTOR TO BE NORMALIZED.
      CALL INNER(N,A,A,PROD,SNORM)
      ANORM=SQRT(SNORM)
      DO 1 I=1,N
    1 AN(I)=A(I)/ANORM
      RETURN
      END
```

THIS PAGE IS BEST QUALITY PRACTICABLE
FROM COPY FURNISHED TO DDC

```
SUBROUTINE SCHMIDT     73/173  OPT=0 TRACE MANTRAP              FTN 4.7+476          79/01/06. 14.28.58

                 SUBROUTINE SCHMIDT(N,A,B,C)
                 COMPLEX A,B,C,PROD,Z1
                 DIMENSION A(N),B(N),C(N)
           C     TO ORTHOGANLIZE  TWO  VECTORS  THROUGH GRAHAM SCHMIDT METHOD
           C     N=NUMBER OF ELEMENTS   IN A,B AND C
           C     A,B=INPUT VECTORS TO BE ORTHOGANALIZED   C=ORTHOGANALIZED B
                 CALL INNER(N,A,B,PROD,SNORM)
                 Z1=PROD
                 CALL INNER(N,A,A,PROD,SNORM)
                 Z1=Z1/SNORM
                 DO1 I=1,N
             1   C(I)=B(I)-Z1*A(I)
                 RETURN
                 END
```

```
SUBROUTINE INNER       73/173  OPT=0 TRACE MANTRAP              FTN 4.7+476          79/01/06. 14.28.5

                 SUBROUTINE INNER(N,A,B,PROD,SNORM)
                 COMPLEX A,B,Z1,Z2,PROD
                 DIMENSION A(N),B(N)
           C     TO CALCULATE  THE INNER PRODUCT OF TWO ORDERED SETS OF COMPLEX.NUMBERS
           C     N=NUMBER OF ELEMENTS IN THE VECTOR
           C     A,B=INPUT VECTORS TO FORM INNER PRODUCT.
           C     PROD=INNER PRODUCT
           C     SNORM=NORM SQUARE IN THE CASE A=B
                 PROD=CMPLX(0.0000000000,0.0000000000)
                 DO1 I=1,N
                 Z1=A(I)
                 Z2=CONJG(Z1)
             1   PROD=PROD+Z2*B(I)
                 SNORM=REAL(PROD)
                 RETURN
                 END
```

THIS PAGE IS BEST QUALITY PRACTICABLE
FROM COPY FURNISHED TO DDC

APPENDIX B

INTERPRETATION OF THE FLUSH HOT-FILM ANEMOMETER OUTPUT FOR THE EXPANSION WAVE BOUNDARY LAYER

The application of a small heated surface film to measure local skin friction has been successfully demonstrated by a number of workers (e.g., Refs. 41 and 49) for steady boundary layer flows. In the present application to the expansion-wave boundary layer the flow is unsteady. However, because of the small physical size of the film its response tends to be quasi-steady and therefore still indicative, at least qualitatively, of the local instantaneous skin friction. Before discussing the expansion wave application further, it is appropriate to first summarize briefly the theory of the hot surface film for steady flows.

Consider a small heated surface film of length L^* in the flow or x direction and width W perpendicular to the flow direction, where $L^* << W$. The film is assumed to be mounted on a substrate of low thermal conductivity so that the surface temperature decreases very steeply along x on either side of the film from the maximum film temperature to a constant wall temperature. For simplicity of analysis, the usual theory replaces this actual distribution of surface temperature by a "top-hat" or square-wave distribution along x over an effective film length L which may be determined by calibration. The Disa hot film used in the present studies is mounted on quartz and has dimensions $L^* = 0.2$ mm, $W = 1$ mm.

When the hot film is immersed in a laminar velocity boundary layer which is cooler, heat transfer to the fluid is assumed to occur through a thin thermal boundary layer which can be considered to begin at the leading edge of the top-hat surface temperature distribution. It is assumed that the thickness of this thermal boundary layer is much smaller

than the thickness of the velocity boundary layer, and also small compared to the effective film length (in order that boundary layer theory applies). Then the velocity distribution in the region of the thermal boundary layer may be approximated by

$$U = \frac{\tau_w}{\mu} y + \frac{1}{2\mu} \frac{dp}{dx} y^2 \qquad \text{(B-1)}$$

where τ_w is the local wall shear stress and μ the molecular viscosity. An integral formation may now be developed using Eq. (B-1) and the following integral energy equation for the thermal boundary layer

$$\frac{d}{dx} \int_0^\infty U(T-T_1)dy = \frac{1}{\rho C_p} q_w(x) \qquad \text{(B-2)}$$

where viscous dissipation is neglected. In Eq. (B-2) T_1 is the temperature outside the thermal boundary layer and $q_w = -k(dT/dy)_w$ is the local rate of surface heat transfer to the fluid. If some reasonable assumption is now made for the temperature distribution $T-T_1$ as a function of y/δ_T, where $\delta_T = \delta_T(x)$ is the thickness of the thermal boundary layer, then Eqs. (B-1) and (B-2) may be combined to obtain an expression for τ_w as a function of the heat transferred to the fluid. In Ref. 49 this is done assuming a universal shape for the temperature profile (independent of dp/dx) as given by Curle [43]. The resulting expression for τ_w is

$$\tau_w = \frac{\mu^2}{\rho\sigma L^2 a}\left(\frac{Q_w}{k\Delta T}\right)^3 - \frac{bL}{2a}\frac{dp}{dx}\frac{k\Delta T}{Q_w} \qquad \text{(B-3)}$$

with the notation:

a,b = constants of the temperature profile; Curle [43] gives a = .2226, b = .1046 based on similarity solutions of the differential equations

L = effective length of the film assuming a top-hat film temperature

distribution with x

$Q_w = q_w L$ = rate of heat transferred to the fluid per unit width of the film

σ = Prandtl number of the fluid

$\Delta T = T_w - T_1$ = overall temperature change across the film thermal boundary layer. $\Delta T = 0$ upsteam of the effective leading edge of the film and ΔT = constant over the effective length L of the film.

In numerous applications the term involving dp/dx in Eq. (B-3) is much smaller than the other two terms and can be neglected for a convenient first approximation. In that case Q_w is proportional to $\tau_w^{1/3}$.

If the film has electrical resistance R_F and is heated by an electric current i, then the steady state energy balance is expressed by

$$i^2 R_F = WQ_w + Q_B \tag{B-4}$$

where WQ_w is the total rate of convective heat loss from the film to the fluid and Q_B is the rate of heat loss to the substrate on which the film is mounted. Combining Eqs. (B-3) and (B-4) and neglecting the dp/dx term gives

$$\frac{i^2 R_F}{\Delta T} = A\,\tau_w^{1/3} + B \tag{B-5}$$

where

$$A = kW\left(\frac{\rho\sigma a L^2}{\mu^2}\right)^{1/3}$$

and

$$B = \frac{Q_B}{\Delta T}$$

In general, A and B depend on ΔT. By calibration in a steady flow of

known skin friction, a basic calibration curve of $i^2R_F/\Delta T$ versus $\tau_w^{1/3}$ can be constructed for constant ΔT. The constants A and B of Eq. (B-5) are thus effectively determined. An unknown skin friction can then be determined from measured values of i and R_F. Additional refinements of the technique, including application to turbulent boundary layers, are discussed in Refs. 41 and 49.

In the present application to the unsteady expansion-wave boundary layer the film was used with a Disa 55D01 anemometer unit which maintained the film resistance or temperature constant by appropriate current variation. If the variations of L and ΔT with time are neglected, with $T_1 \approx T_o$ assumed, then the foregoing steady state relations may be expected to apply qualitatively if the response of the film thermal boundary layer is near quasi-steady. The latter will be true if the diffusion time of the film thermal boundary layer, which is $\delta_T^2/\alpha \approx \delta_T^2/\nu_o$ (for air), is much smaller than the time characterizing change of the local velocity profile, which may be taken as $u/(\partial u/\partial\tau)$ for $y \to 0$ where τ is the time after wavehead arrival.

Neglecting $\partial p/\partial x$, the leading term for u as $y \to 0$ is given by (from Sec. 2 results)

$$u \approx 2\beta a_o\left(\frac{\tau}{\pi\nu_o}\right)^{1/2}\frac{y}{\tau+t_s} \tag{B-6}$$

where t_s is the time for the expansion wavehead to reach the film location. The characteristic time for change of the velocity profile is then

$$u/(\partial u/\partial\tau) \approx \frac{2\tau(\tau+t_s)}{t_s-\tau}$$

To obtain an estimate of δ_T at the trailing edge of the film (after

distance L along x) the convection and diffusion times may be equated on the assumption of near quasi-steady behavior, i.e., $L/u_{y=\delta_T} = \delta_T^2/\nu_o$. This gives $\delta_T \simeq \left(\frac{\nu_o L}{u/y}\right)^{1/3}$ as the thermal layer thickness developed over the length L, where u/y depends on τ as given by Eq. (B-6). From these relations, the condition $\delta^2/\nu_o << u/(\partial u/\partial\tau)$ characterizing near quasi-steady behavior then becomes

$$\frac{L}{a_o t_s} << 2^{3/2} \frac{(1+\tau/t_s)^{1/2}}{(1-\tau/t_s)^{3/2}} \left(\frac{\tau}{t_s}\right)^2$$

For the present values of $L \simeq L^*$, a_o, and t_s, this condition is satisfied quite rapidly, for $\tau/t_s > .05$ say, as τ increases from the initial value of zero. For $L^* = 0.2$ mm, $a_o = 1000$ ft/sec, and $t_s = 5 \times 10^{-3}$ sec, $L/(a_o t_s)$ is about 10^{-4}. Thus in the present expansion wave experiments the hot film response was near quasi-steady except at the very earliest times after the wavehead arrival.

On the basis of a quasi-steady response, Eq. (B-5) was applied to hot-film records over a range of conditions of the expansion-wave boundary layer. The heat loss term Q_B was measured under no flow conditions where the free convection loss was negligible by comparison. Assuming the same heat loss Q_B to apply under flow conditions (for a fixed film temperature), Eq. (B-5) was applied to determine τ_w from the measured film voltage (iR_F) versus time records. Comparison of τ_w so determined with the theoretical prediction from the boundary layer theory of Sec. 2 showed qualitative agreement for an effective film length L of 0.7L*. This comparison is summarized in Fig. 61. The value of L/L* observed in the present experiments is less than that typically observed in steady state experiments (e.g., L/L* = 1.4 in Ref. 41). This is probably due in part to the inherent unsteadiness of the present flow. Although the

film temperature itself is maintained constant, the distribution of surface temperature adjacent to the film will become narrower with increasing time.